Functional magnetic nanoparticles for bioactive protein delivery under physiological temperature

Sanjana Ganesh Mukunda

PhD

University of York

Biology

October 2025

Abstract

Current therapies for tissue damage, especially in bone repair, are limited by invasiveness and susceptibility to infection. The clinical problem of nonunions —fractures that fail to heal completely within the expected clinical timeframe 5–10% of annual fractures, underscores the need for less invasive and more targeted treatments. Successful bone regeneration relies on mesenchymal stem cells (MSCs) differentiating into osteoblasts, a critical process driven by bioactive signalling molecules. To overcome the limitations of current pharmaceutical interventions and surgical grafts, which include high-dosage side effects and a lack of controlled release, this research aims to develop a drug delivery system.

This study investigates temperature sensitive polymer poly(-isopropylmethacrylamide) (PNIPMAM)-coated superparamagnetic iron oxide nanoparticles (SPIONs) as a thermo-responsive platform for the delivery of the osteo-inducive growth factors. pPrimary objective was to optimize the synthesis of PNIPMAM-coated SPIONs to ensure a reproducible and stable formulation. This was achieved by refining the coating process, resulting in a consistent polymer coating with confirming lower critical solution temperature (LCST) above physiological temperature. Biocompatibility assessments using the Y201 MSC line confirmed the coated nanoparticles are non-toxic at concentrations up to 1 mg/ml and do not interfere with osteogenic differentiation on their own, establishing a crucial baseline for subsequent bioactivity assays.

The system achieved high BMP2 encapsulation efficiency ~95% with bioactivity quantified via ALP activity in C2C12 cells. However, there was no release of BMP2 under the tested conditions. Conversely, delivering the thermally unstable Wnt3a was successful by incorporating glycerol as a thermos-stabilizing additive, which also lowered the polymer's LCST at physiologically relevant temperature. This optimized system conclusively demonstrated a temperature-triggered, bioactive Wnt3a release, particularly with apotransferrin as a competitor protein.

In conclusion, this work establishes PNIPMAM-coated SPIONs as a potential viable platform for encapsulating and enabling on-demand, localized delivery of osteogenic factors. The findings highlight the critical influence of protein-specific characteristics and the formulation’s biochemical environment on release efficiency, providing a strong foundation for future advancements in regenerative medicine.

Declaration

I declare that this thesis is a presentation of original work and I am the sole author. This work has not previously been presented for an award at this, or any other, university. All sources are acknowledged as references. Moreover, I declare that in the event the work of others has been used, this has been fully acknowledged in the text and as references. Synthesis of nanoparticles (Section 2.2) was developed by Rajat Sharma previous, a previous PhD student from the lab of Prof. Victor Chechik in the Department of Chemistry and the development of the protein encapsulation methodology (Section 2.3.5) was developed by Mathew Walker another previous PhD student from the lab of Prof. Daniel Ungar, Prof. Paul Genever and Prof Victor Chechik.

Acknowledgments

I would like to express my sincere gratitude to Prof. Daniel Ungar for his invaluable guidance, encouragement, and support throughout my research and writing. My heartfelt thanks to Prof. Paul Genever for his continuous support and for providing new direction to this project. I am grateful to Prof. Victor Chechik for his expert advice and guidance on the chemistry aspects of my work. I thank all three of my supervisors for their active involvement, mentorship, and unwavering support during every stage of my PhD. I would also like to thank my TAP member, Dr. Amanda Barnes, for her insightful guidance and encouragement, and for creating such a supportive environment during my research journey.

My sincere appreciation goes to the academic and technical staff for their training and assistance with various instruments: Andrew Leech (Nano-DSF and Clariostar), Karen Hogg (Flow Cytometry), and Karen Hodgkinson (TEM). Thanks to Rajat Sharma for training me in the beginning for the chemistry part of the project. A heartfelt thanks to all the postdoctoral researchers - Dave Mentlak, Amy Milburn, Richard Ingram, and Naeem Iqbal for their constant help, kindness, and encouragement. Their enthusiasm and scientific insight made the most challenging times easier to overcome and further fuelled my passion for research. I am also thankful to all the members of J0 - Dimi, Savvas, Josie, Katherine, Kamilla and Nisreen for their friendship and support.

A special thanks to Will Jones and Joe Parr for making the lab such an enjoyable and lively place in the lab. For Jess Petts for teaching me how to crochet. I am also very grateful to my international group of friends that I was really closed to Ploy, Mahmoud, Rumesha, Saffron, Karen, Hatwan, and Maybet for making my time in the UK so memorable. Getting to know different cultures and sharing food and experiences with you all has been wonderful.

To Ploy, I am especially thankful for your constant support and companionship. I will always cherish the memories of our travels and adventures together. To Mahmoud, in particular, your positivity and friendship helped me through many difficult days and Thank you for always being there for me.

To my dearest friend Amy Wolstenholme-Hogg, I can’t thank you enough, especially during the early stages of my PhD, from practising presentations and helping me through TAP meetings to taking long walks and sharing delicious baked cakes that you make. You have been a constant source of support and joy throughout this journey, and I am forever grateful for your friendship.

Finally, I would like to thank my family - my parents, Saroja and Mukundan, for shaping who I am and for your unconditional love and support, especially during the final stages of my write-up period. Special thanks to my brother Sandeep for encouraging me to pursue a PhD and for always being there during the years I was away from home, and to my sister-in-law Aishwarya for her constant encouragement and for always being there for me when I needed the most. I am forever grateful for you.

This PhD was funded by the Government of Karnataka, and I am deeply grateful for the opportunity and support I received. The extension period was funded by the Radhika Fund, which provided crucial support during the final months of my research.

Abbreviation

ALP – Alkaline Phosphatase

AMF – Alternating Magnetic Field

APC – Adenomatous Polyposis Coli

ATRP – Atom Transfer Radical Polymerization

BMP – Bone Morphogenetic Protein

BSA – Bovine Serum Albumin

CKIα – Casein Kinase Iα

CTA – Chain Transfer Agent

DIPEA – N,N-diisopropylethylamine

DTT – Dithiothreitol

Dvl – Dishevelled

EPR – Enhanced Permeability and Retention

FBS – Fetal Bovine Serum

FDA – U.S. Food and Drug Administration

FGF – Fibroblast Growth Factor

Fzd – Frizzled

GFP – Green Fluorescent Protein

GSK-3β – Glycogen Synthase Kinase-3β

IGF – Insulin-like Growth Factor

IgG – Immunoglobulin G

IPA – Isopropanol

LCST – Lower Critical Solution Temperature

LPEMF – Low-Frequency Pulsed Electromagnetic Field

LRP5/6 – Low-density Lipoprotein Receptor-related Protein 5/6

MDT – Magnetic Drug Targeting

MH – Magnetic Hyperthermia

MSC – Mesenchymal Stem/Stromal Cell

NDA – Nitrodopamine

NIPAM – N-isopropylacrylamide

NIPMAM – N-isopropylmethacrylamide

OAm – Oleylamine

ODM – Osteogenic Differentiation Medium

Osx – Osterix

OVA – Ovalbumin

PCP – Planar Cell Polarity

PEG – Polyethylene Glycol

PEI – Polyethylenimine

PI – Propidium Iodide

PLC – Phospholipase C

PNIPAM – Poly(N-isopropylacrylamide)

PNIPMAM – Poly(N-isopropylmethacrylamide)

PTBMA – Poly(tert-butyl methacrylate)

RAFT – Reversible Addition–Fragmentation Chain-Transfer

RBF – Round Bottomed Flask

RES – Reticuloendothelial System

ROS – Reactive Oxygen Species

Runx2 – Runt-related Transcription Factor 2

SAR – Specific Absorption Rate

SPIONs – Superparamagnetic Iron-Oxide Nanoparticles

TCF/LEF – T-cell Factor/Lymphoid Enhancer-binding Factor

TEM – Transmission Electron Microscopy

TGA – Thermogravimetric Analysis

TGF-β – Transforming Growth Factor-beta

TRF – Apotransferrin

UCST – Upper Critical Solution Temperature

Table of Contents

List of Figures

List of Tables

Chapter 1

1. Introduction

1.1 Drug delivery

Over the past few decades, our understanding of human biology and the molecular basis of diseases has advanced dramatically. This progress has enabled the development of increasingly targeted and effective therapeutic strategies. However, a central challenge in modern medicine is the precise delivery of drugs to diseased tissues while minimising off-target effects and systemic toxicity [1, 2].

This challenge has driven the growth of the field of drug delivery, which focuses on optimising how, where, and when therapeutic agents are released in the body [3]. One of the most transformative advances in this field is nanomedicine, which uses nanoparticles to transport drugs directly to specific tissues or groups of cells. These nanocarriers can enhance drug solubility, protect sensitive molecules from degradation, and improve therapeutic outcomes by concentrating the drug at the site of action while reducing side effects in healthy tissues [4].

The concept of targeted drug delivery, particularly using nanoparticles, has gained prominence in cancer therapy. This is because cancerous tissues often exhibit abnormal and highly permeable blood vessels owing to rapid and disorganised angiogenesis [5]. In contrast, healthy tissues typically have intact vasculature, making them less permeable to nanoparticles. This difference allows nanoparticles to preferentially accumulate in tumour sites through a phenomenon known as the enhanced permeability and retention (EPR) effect, thereby minimising damage to healthy tissues [6] (**Figure 1.1**).

While the EPR effect initially drove interest in nanoparticle-based drug delivery for cancer, the versatility of nanomedicine has since expanded into other therapeutic areas, including tissue engineering and regenerative medicine. In particular, targeted delivery systems are being developed for bone regeneration, where the localised and sustained release of bioactive molecules, such as growth factors, is essential for promoting healing and guiding cellular responses.

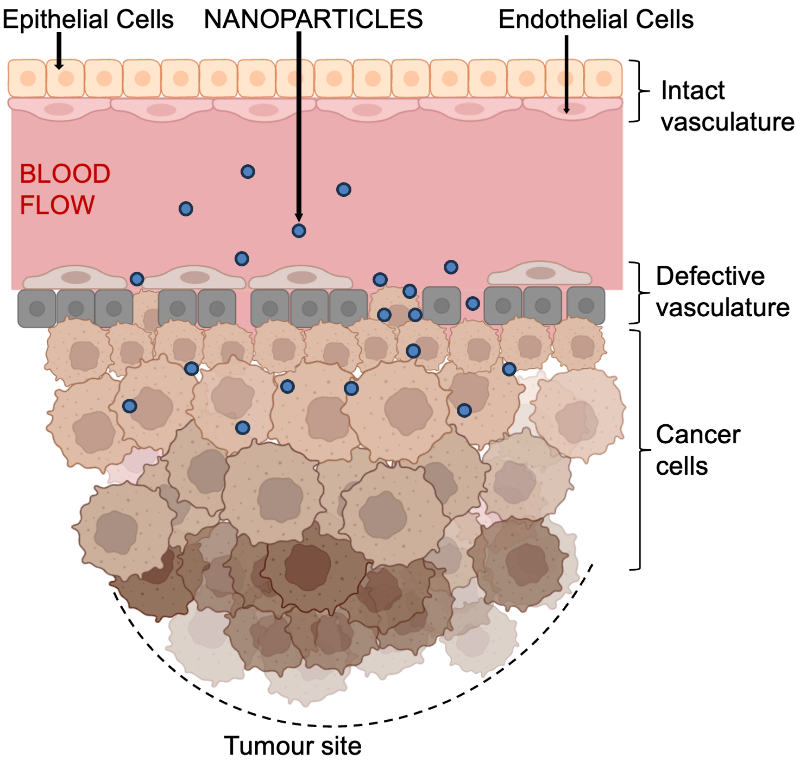

Figure 1.1: EPR effect enabling nanoparticle accumulation at the tumour site: A schematic illustrating how nanoparticles circulating in the bloodstream extravasate through the defective, porous vasculature surrounding a tumour and accumulate at the tumour site. This passive targeting mechanism allows for the selective delivery of drugs to cancerous tissues while minimising exposure to healthy areas with intact blood vessels. (Created with BioRender.com)

1.1.1 Protein therapeutic

Protein-based therapeutics have emerged as a major class of biologically derived treatments offering high specificity and potency. The field of biologics has revolutionised modern medicine, offering precision and efficacy often unmatched by traditional small-molecule drugs. These complex macromolecules encompassing monoclonal antibodies, therapeutic enzymes and other recombinant proteins that leverage sophisticated biological mechanisms to precisely target the intended site of action [7].

The intrinsic fragility and macromolecular dimensions of protein therapeutics, coupled with challenges such as enzymatic degradation, limited membrane permeability, and rapid systemic clearance, present a formidable obstacle to their effective delivery [8]. Unlike small-molecule drugs, proteins are highly susceptible to proteolytic cleavage, aggregation, and rapid systemic clearance mediated by renal filtration and reticuloendothelial uptake, which collectively constrain their half-life and bioavailability [9, 10]. The biological activity of a protein specifically like growth factors is intrinsically linked to its precise binding affinity to specific receptors and the subsequent activation of intracellular signalling pathways [11]. Any deviation from their native conformation due to aggregation, enzymatic cleavage, or denaturation during delivery can lead to a complete loss of bioactivity [8, 12]. Moreover, the efficacy of signalling molecules frequently depends on maintaining a specific local concentration and temporal release profile to orchestrate complex biological processes, such as tissue regeneration or cell differentiation. Uncontrolled or premature protein release can result in off-target effects, systemic toxicity, or insufficient concentrations at the desired site of action [13].

To overcome these multifaceted limitations and unlock the full clinical promise of protein therapeutics critically depends on the development of advanced delivery strategies capable of protecting their integrity, ensuring specific localisation, and controlling their release. In this context, nanomedicine has emerged as a powerful and versatile platform uniquely suited to meet these requirements for protein delivery.

1.2 Nanomedicine

Nanomedicine is a rapidly advancing field that applies the principles of nanotechnology to medical challenges such as diagnosis, treatment, and tissue repair. It involves engineering nanoscale materials, typically 1–100 nm, that can interact precisely with biological molecules and structures [14]. One of its most transformative applications is drug delivery, where nanocarriers can protect therapeutic agents from degradation, enhance solubility, and enable controlled, targeted release. These features help overcome limitations associated with traditional drugs, such as poor bioavailability, systemic toxicity, and frequent dosing requirements [15].

While nanoparticles have improved delivery precision and reduced off-target effects, challenges such as achieving sufficient accumulation at the target site and ensuring timely release remains a challenge [2]. Overcoming these limitations requires the development of smart, stimuli-responsive systems such as thermoresponsive polymers that can respond to local physiological cues like temperature or pH, thereby enabling controlled, site-specific drug release [16-18].

1.2.1 Superparamagnetic iron-oxide nanoparticles (SPIONs)

The rapidly advancing field of nanotechnology has significantly impacted various scientific disciplines, particularly medicine and materials science. Among the many nanomaterials explored, SPIONs have emerged as some of the most promising and versatile agents because of their unique magnetic properties, which enable both precise targeting and real-time imaging [19, 20]. SPIONs are typically composed of iron oxides such as magnetite (Fe_3O_4) or maghemite (γ-Fe_2O_3) [21], making them nontoxic, biodegradable, biocompatible, and efficiently cleared from the human body via the iron metabolism pathways. Above all this these particles exhibit a distinctive magnetic behaviour known as superparamagnetism [22].

1.2.1.1 Superparamagnetism

Superparamagnetism is a distinct magnetic phenomenon observed in small, single-domain nanoparticles, typically within the size range of 2–20 nm [23]. At this nanoscale, these particles exhibit unique magnetic properties due to containing a single magnetic domain (**Figure 1.2**A). As a result, they exhibit high magnetic susceptibility but have zero coercivity and no remanent magnetisation [24]. This means that they respond quickly to an external magnetic field but lose their magnetisation almost instantly once the field is removed, unlike bulk ferromagnetic materials that retain magnetism after the removal of the external magnetic field (**Figure 1.2** B)[22]. This absence of residual magnetism is critical for biomedical applications, as it prevents particle aggregation in biological fluids, ensuring stable dispersion and minimising the risk of embolism [22, 25]. Their rapid and reversible response to external magnetic fields allows for precise and transient magnetic control, enabling a wide array of applications. When exposed to an alternating magnetic field (AMF), the magnetic moments within these single-domain SPIONs continuously reorient in response to the rapidly changing field. This process of magnetic relaxation results in the generation of heat in the particle's core [23, 26]. Consequently, the inherent magnetic responsiveness of SPIONs facilitates not only non-invasive imaging modalities like MRI, but also enables targeted therapeutic strategies with reduced systemic toxicity, leveraging both magnetic guidance and localised heat generation called magnetic hyperthermia [20, 27]. Owing to their unique multifunctionality, SPIONs have garnered considerable interest across biomedical fields such as drug delivery and tissue engineering. In regenerative medicine, their ability to enable the localised delivery of bioactive molecules positions them as promising tools for promoting targeted tissue repair while minimising systemic side effects.

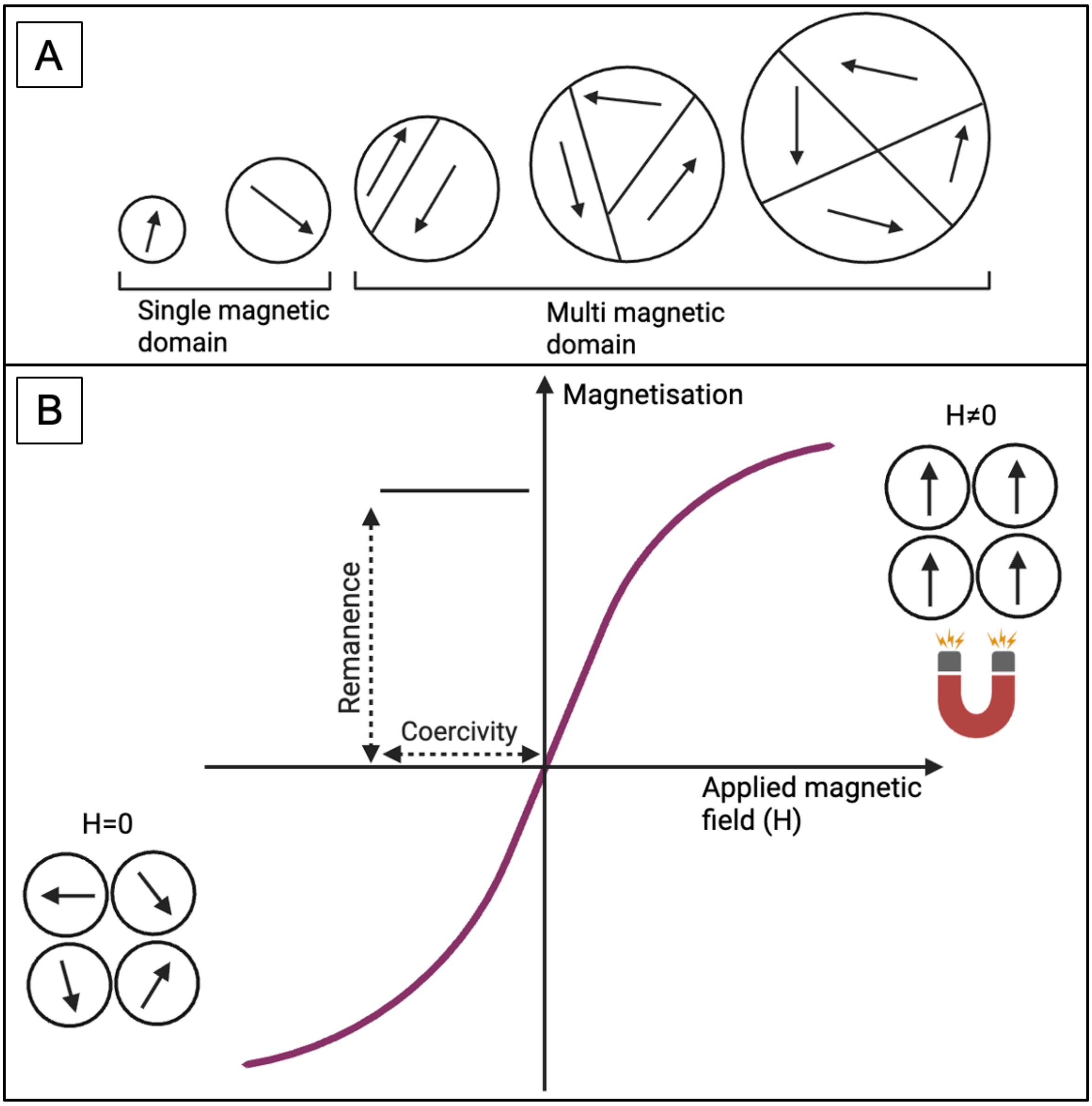

Figure 1.2: Magnetic domain structures and magnetisation behaviour of magnetic materials: (A) Transition from single magnetic domain to multi-domain structure as particle size increases. Small particles exhibit uniform magnetisation, while larger particles contain multiple domains to minimise magnetic energy. (B) Magnetisation curve characteristic of superparamagnetic materials, parameters include remanence (residual magnetisation) and coercivity (field strength required to demagnetise). Insets illustrate random domain orientation in the absence of a magnetic field (H = 0) and aligned domains under an applied field (H ≠ 0). (Created with BioRender.com)

1.2.1.2 SPIONs in drug delivery

SPIONs have garnered considerable interest in targeted drug delivery due to their ability to be guided by external magnetic fields [28]. Unlike conventional systemic delivery methods that often suffer from non-specific distribution and off-target effects, SPIONs offer a compelling alternative. Their inherent magnetic properties, coupled with their nanoscale size and high biocompatibility, make them ideal for precise control over therapeutic agent distribution. The concept of magnetic drug targeting (MDT) directly leverages these properties, involving the functionalization of SPIONs with therapeutic molecules and the use of an externally applied magnetic field to steer and retain these particles at the target site [29-31]. This approach has been compellingly demonstrated in early preclinical and clinical studies.

A Phase I clinical trial explored the use of magnetic drug targeting in patients with advanced solid tumours. This study used a ferrofluid, a colloidal dispersion of iron oxides and hydroxides, chemically bound to the anticancer drug doxorubicin. Under the influence of an external magnetic field, these magnetic particles are directed towards the tumour site, effectively serving as a vehicle to concentrate the drug specifically within the targeted tissue [29]. Another study demonstrated successful locoregional cancer treatment using magnetic drug targeting with iron oxide bound to mitoxantrone, achieving complete remission of experimental squamous cell carcinoma in rabbits without toxicity through intra-arterial application with an external magnetic field [32]. This strategy was further supported by later studies, which demonstrated that applying an external magnetic field significantly enhanced the accumulation of iron oxide nanoparticles in gliomas, achieving a 5-fold increase in tumour exposure and a 3.6-fold improvement in target selectivity over normal brain tissue. These results highlight their potential for MRI-guided, targeted drug delivery [33]. Various drug payloads have been successfully delivered using SPION-based systems, including chemotherapeutics like paclitaxel [19], doxorubicin [29] and anti-inflammatory agents [34]. This capability for spatially controlled accumulation represents a significant advantage, as it enables the reduction of the overall drug quantity required for local therapeutic concentrations and minimises severe side effects at non-target sites.

Beyond their utility in magnetic targeting, SPIONs offer an additional therapeutic modality through their ability to generate heat when exposed to an alternating magnetic field (AMF), a principle that forms the basis of magnetic hyperthermia. This dual functionality enables

SPIONs to act as drug carriers and agents for localised thermal therapy, enhancing their potential in cancer treatment strategies.

1.2.1.3 Magnetic hyperthermia

Magnetic hyperthermia (MH) is a promising therapeutic approach that utilises SPIONs to generate localised heat under an AMF. This method aims to deliver therapeutic heat directly to cancer cells to induce tumour ablation [35]. This phenomenon relies on the conversion of magnetic energy into thermal energy when SPIONs are exposed to a rapidly oscillating magnetic field, typically ranging from 100 kHz to several MHz [31, 36]. Under such a field, the single-domain magnetic moments within the SPIONs continuously attempt to realign with the changing magnetic orientation. This repeated reorientation results in energy dissipation as heat through two main mechanisms (**Figure 1.3**).

1. **Néel relaxation**, where the magnetic moment flips within the particle's crystal structure (dominant in smaller SPIONs) [36].
2. **Brownian relaxation**, where the entire nanoparticle physically rotates within its surrounding medium due to viscous drag (more significant in larger particles) [35].

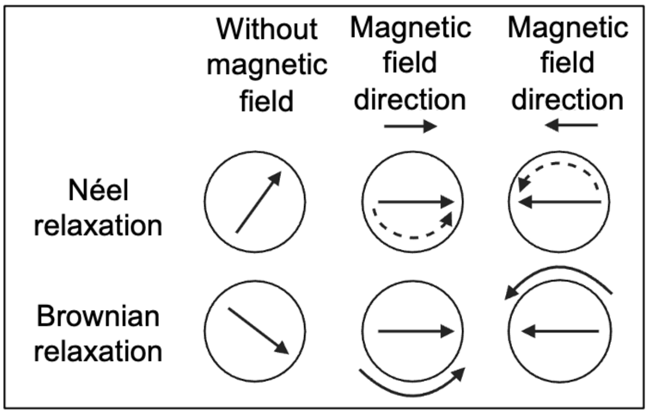

Figure 1.3: Mechanisms of magnetic relaxation in SPIONs: Illustration of the two main types of relaxation: Néel relaxation, where the magnetic moment rotates within a fixed particle, and Brownian relaxation, where the entire nanoparticle physically rotates in response to an applied magnetic field. In the absence of a magnetic field, the magnetic moments are randomly oriented. Under an external magnetic field, moments align with the field direction, either through internal flipping (Néel) or particle rotation (Brownian), enabling magnetic heating applications.

In physiological environments, both mechanisms can contribute simultaneously, depending on particle characteristics such as size, shape, surface coating, and the viscosity of the medium. The efficiency of this thermal conversion is commonly measured using the Specific Absorption Rate (SAR), expressed in watts per gram of iron (W/g Fe), which reflects the amount of heat generated per unit mass. A higher SAR indicates a more effective magnetic-to-thermal energy conversion. Precise control over heat generation, facilitated by the magnetic properties of SPIONs, not only enhances therapeutic targeting but also helps minimise collateral damage to healthy tissues [24].

Magnetic hyperthermia was first introduced by Gilchrist in 1957, who demonstrated that iron oxide nanoparticles could be heated using an alternating magnetic field to damage cancerous tissues in the lymph nodes [37]. Decades later, this concept was significantly advanced, with studies showing that the direct injection of magnetic nanoparticles into tumours, such as gliomas in animal models, enabled more precise and localised heating of cancerous tissue [38, 39]. Subsequent research has demonstrated the feasibility of this approach for treating recurrent prostate cancer in humans [27]. In 2010, MagForce AG's technology, branded as NanoTherm®, became the first nanoparticle-based hyperthermia therapy to receive CE certification for the treatment of glioblastoma in Europe [40].

This principle can also be exploited for drug release by coating SPIONs with a thermosensitive polymer [17, 18], then using localised heat generation to trigger release of encapsulated therapeutic molecules. The versatility of SPIONs lies in their modifiable surface chemistry, which allows for the conjugation of a broad range of drugs and targeting ligands. Conventional magnetic hyperthermia studies often employ SPIONs, utilising frequencies above 100 kHz for durations typically around 30 min [31, 37], with the primary aim of elevating the entire local environment to temperatures between 40 and 48 °C to induce cell death. In contrast, for triggered drug release, the objective is not to heat the entire tissue volume for prolonged periods of time. Instead, by carefully controlling the heating parameters (e.g. shorter duration of AMF exposure), heat generation can be predominantly confined to the nanoparticle core. This transient, localised heat can then efficiently radiate a minimal distance to the surface-bound thermosensitive polymer, inducing its phase transition and initiating the controlled release of the therapeutic encapsulated cargo without causing widespread environmental heating or significant collateral damage to any tissue.

1.3 Thermo-responsive polymers

Polymers are commonly employed to coat SPIONs, and among the various polymers used for coating, thermoresponsive polymers are particularly valuable. These polymers undergo significant reversible changes in their physical and chemical properties in response to temperature fluctuations, making them ideal for controlled and stimuli-responsive drug release systems. A key characteristic is a sharp phase transition at a specific temperature, often a Lower Critical Solution Temperature (LCST) or Upper Critical Solution Temperature (UCST). LCST is the temperature above which a polymer becomes insoluble in a solvent UCST its inverse

For drug delivery applications, polymers with an LCST are especially relevant. Below their LCST, these polymers are typically hydrophilic and swollen (dissolved in aqueous buffer), adopting an extended coil conformation. This ensures the stability of the nanoparticle system and efficient encapsulation of therapeutic agents within the SPION core, allowing stable circulation and drug retention at physiological temperatures. As the temperature rises above the LCST, they become more hydrophobic and undergo a sharp phase transition, leading to chain collapse and precipitation, this phenomenon is known as coil-to-globule transformation. This conformational change manifests as alterations in solubility, volume, permeability, and mechanical strength, thereby acting as a precise trigger for the rapid release of encapsulated proteins (**Figure 1.4**) [41].

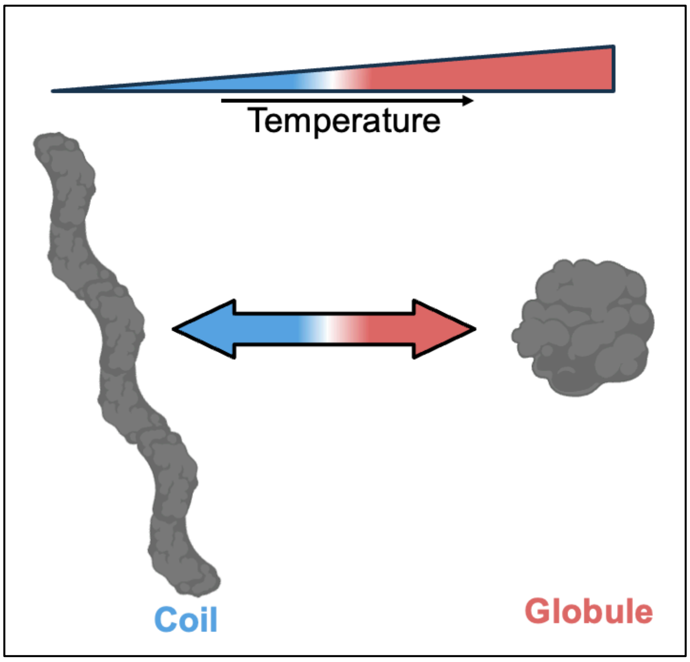

Figure 1.4: Temperature-responsive Coil-to-Globule conformational change of thermosensitive polymers: Schematic illustration showing the reversible conformational transition of thermosensitive polymers at the lower critical solution temperature (LCST). Below the LCST, polymer chains adopt an extended coil-like structure. As the temperature increases above the LCST, the polymers collapse into a compact globular form. This transition is fully reversible and is governed by changes in the surrounding temperature. (Created with BioRender.com)

1.3.1 Coil-to-globule transition

The coil-to-globule transition observed in thermoresponsive polymers, such as poly(N-isopropylacrylamide) (PNIPAM) and poly(N-isopropylmethacrylamide) (PNIPMAM), is a temperature-induced conformational change that occurs in aqueous environments and is crucial for stimuli-responsive drug delivery systems. These amphiphilic polymers contain hydrophilic amide groups and hydrophobic isopropyl side chains [42].

At temperatures below the LCST, the polymer adopts an expanded coil conformation, which is stabilised by extensive hydrogen bonding between the amide groups and surrounding water molecules (Doberenz et al., 2020). Water molecules also form a structured, entropically unfavourable shell around hydrophobic regions (Quoika et al., 2020), maintaining polymer solubility.

When the temperature exceeds the LCST, the hydrogen bonding between water and the amide groups weakens, and the structured water surrounding the hydrophobic isopropyl groups is released. This release provides an entropic gain that drives the polymer to collapse into a compact globular form. In this state, the hydrophilic amide groups become buried within the core, while the hydrophobic isopropyl groups are exposed, resulting in decreased solubility and significant water loss. This transition is primarily driven by hydrophobic interactions rather than chemical bond breakage or formation [41].

This conformational rearrangement leads to a marked reduction in hydrodynamic radius and can promote aggregation or phase separation, ultimately causing precipitation. Crucially, this transformation is fully reversible by cooling the system below the LCST, allowing rehydration and return to the coil state [41, 43]. This reversible behaviour makes thermoresponsive polymers ideal for controlled drug release, where heat (e.g. from magnetic hyperthermia) triggers the diffusion of encapsulated proteins by altering polymer-shell permeability or inducing carrier collapse.

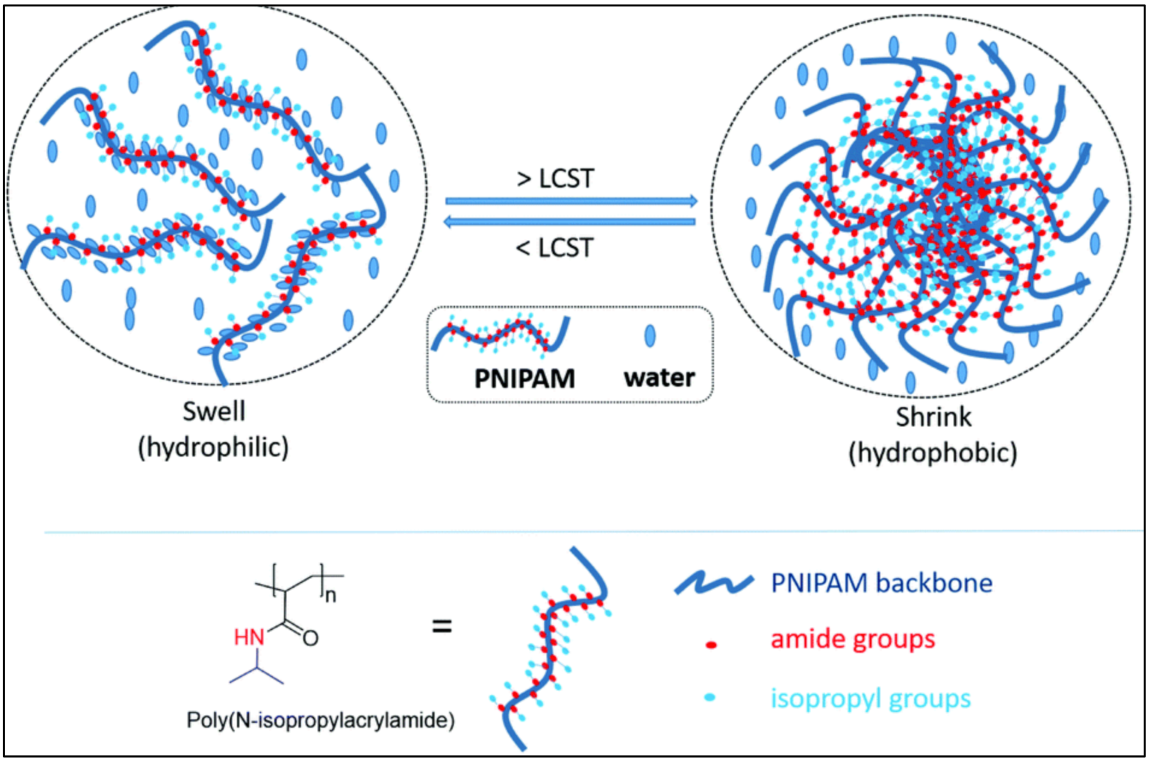

Figure 1.5: Thermo-responsive behaviour of PNIPAM in aqueous solution: Schematic representation of the temperature-induced phase transition of PNIPAM. Below its LCST, PNIPAM is hydrophilic and swells with water, forming an extended coil structure. Above its LCST, it becomes hydrophobic, expelling water and collapsing into a compact, shrunken globule. The diagram highlights the PNIPAM backbone, amide groups, and isopropyl groups responsible for this behaviour [44].

1.3.2 PNIPAM and PNIPMAM

PNIPMAM and PNIPAM are thermoresponsive polymers composed of repeating units of N-isopropylmethacrylamide (NIPMAM) and N-isopropylacrylamide (NIPAM), respectively [45]. Both PNIPAM and PNIPMAM are cornerstone polymers in the development of thermoresponsive systems for nanomedicine. PNIPAM, with its well-characterised LCST of approximately 32 °C, has historically served as the benchmark thermoresponsive polymer, leading to foundational research and demonstrating versatile applications in drug delivery and tissue engineering [46].

However, for applications specifically targeting precise in vivo drug release, nuanced differences in LCSTs have become critical. Although PNIPAM has been extensively studied, its LCST of approximately 32 °C renders it less suitable for stable *in vivo* drug delivery. It will undergo premature collapse/phase transition at physiological temperatures, and release of cargo immediately upon entry into the body rather than at the desired target site. In contrast, PNIPMAM exhibits an LCST typically above 44 °C [47, 48]. This attribute makes PNIPMAM particularly advantageous because it ensures that the polymer remains soluble and effectively retains the encapsulated cargo until a temperature trigger above the physiological temperature is applied. Even within mild hyperthermic ranges, PNIPMAM can undergo a rapid and complete coil-to-globule collapse triggered by localised thermal stimuli that precisely reach the phase transition temperature at the target site, enabling effective release of the encapsulated cargo.

Given that the objective of this study is to focus on SPION-based systems for highly localised and minimally invasive drug release, the thermos-responsive characteristics of PNIPMAM present a compelling advantage. Its LCST of > 37 °C aligns perfectly with the goal of triggering drug release specifically at the core body temperature or with subtle increases induced by SPION-mediated magnetic hyperthermia. The precise thermal window offered by PNIPMAM minimises the need for extensive heating of the surrounding healthy tissues, thereby enhancing the therapeutic index of the proposed drug delivery system.

1.3.2.1 PNIPMAM in the field of medicine

Building on this foundation, PNIPMAM-based hydrogels and nanogels have been used for controlled release of therapeutic agents. A study reported the synthesis and characterisation of PNIPMAM core/ poly(tert-butyl methacrylate) (PTBMA) shell nanogels for controlled release of chemotherapeutics, specifically doxorubicin. The study found that nanogels demonstrated superior effectiveness as delivery vehicles for chemotherapeutics, showing improved drug partitioning, loading, and controlled release properties [47]. Similarly, an *in vitro* study developed gold core-polymeric shell nanoparticles with varying compositions of PNIPAM and PNIPAM-co-PNIPMAM that exhibited temperature-sensitive behaviour, enabling the sustained and triggered release of doxorubicin [49].

Another study demonstrated the potential of combining PNIPMAM with PNIPAM to fine-tune the phase transition temperature closer to physiological conditions. This hybrid approach takes advantage of the sharp and well-defined coil-to-globule transition of PNIPMAM while leveraging the lower LCST of PNIPAM. As a result, the system becomes responsive at temperatures that are clinically relevant, particularly for controlled drug delivery. This strategy highlights the feasibility of slightly lowering PNIPMAM's LCST without requiring excessive thermal input, thereby maintaining cell viability and minimizing thermal damage to surrounding tissues [50]

Despite these highly advantageous features of PNIPMAM, relatively few *in vitro* studies have been conducted using PNIPMAM-based systems, largely due to its higher LCST typically above normal human body temperature. Achieving the necessary temperature increase of approximately 8 °C to induce the polymer's phase transition can pose risks, potentially affecting healthy cells or compromising the cellular environment. However, this limitation can be effectively addressed by integrating PNIPMAM with SPIONs, which offers a mechanism for highly localised magnetic heating. This development could be potentially useful for the activation of stem cells in situ through the delivery and release of growth factors to promote for example stem cell-driven bone regeneration.

1.4 Bone

Bone is a dynamic tissue that continuously undergoes remodelling to maintain its structural integrity and functionality [51]. Although bone possesses remarkable regenerative capabilities and efficiently restores its normal structure and function, there are situations in which the healing process is compromised. Conditions such as nonunion fractures [52], malunion fractures, or improper tissue restoration during bone grafting can present significant challenges [53], especially in cases of severe trauma, older patients, or those with underlying metabolic conditions [54]. In these scenarios, enhancing the bone regeneration process becomes essential.

Bone regeneration is primarily driven by osteoblasts, which originate from stem cells, often referred to as mesenchymal stem cells (MSCs) found in the bone marrow. These MSCs have the capacity to differentiate into osteoblasts under the influence of bioactive molecules such as growth factors. In addition to their differentiation potential, MSCs play a vital coordinating role in bone remodelling by responding to signals released during bone resorption, such as TGF-β, which directs their migration to sites in need of repair [55]. This dynamic process of bone remodelling involves a continuous cycle in which old bone is broken down by osteoclasts and replaced by new bone formed by osteoblasts. Maintaining this balance is essential for bone health [55] (**Figure 1.6**).

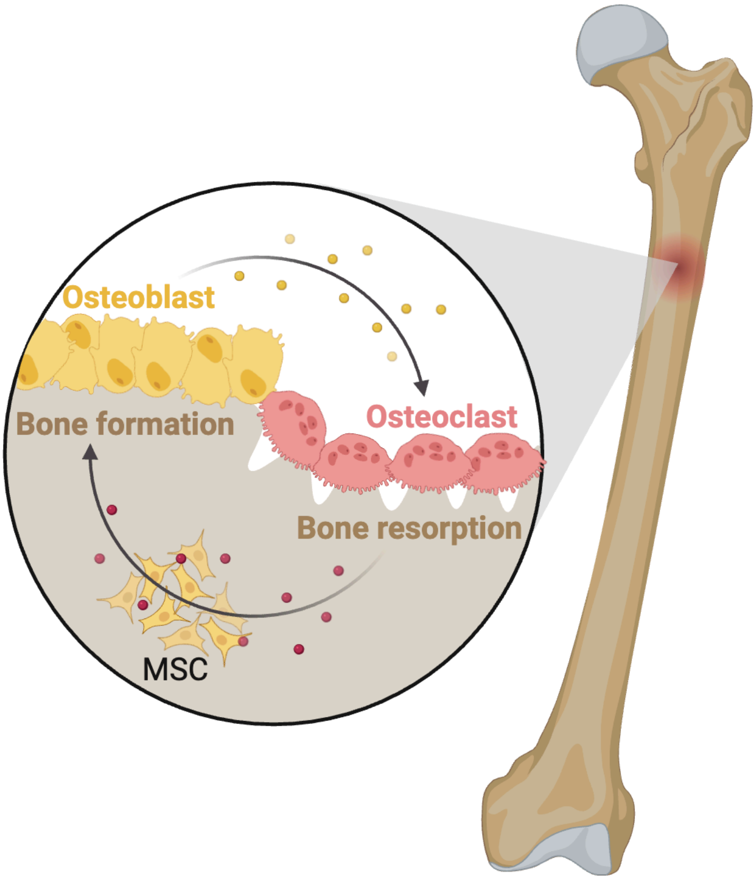

Figure 1.6: Cellular dynamics of bone remodelling: Schematic representation of the dynamic process of bone remodelling within a long bone. The magnified inset illustrates the coordinated activities of osteoclasts, responsible for bone resorption, and osteoblasts, which are derived from MSCs and are responsible for new bone formation. This continuous

cycle of resorption and formation maintains bone health and integrity. (Created with BioRender.com)

1.5 Mesenchymal stem/stromal cells (MSC)

Human mesenchymal stromal cells (MSCs) are heterogenous populations containing rare multipotent stem cells, hence the term “MSCs” is often used to describe both stem and stromal cell types. True stem cells are characterised by their self-renewal capacity and ability to differentiate into three distinct lineages: osteoblasts, chondrocytes, and adipocytes, which give rise to bone, cartilage, and fat tissues in adults, respectively [56, 57]. While bone marrow remains the classical source of MSCs, similar cells have also been successfully isolated from various other adult connective tissues, including the adipose tissue, umbilical cord, and periosteum, suggesting a widespread distribution of MSC-like cells throughout the body [57, 58]. However, harnessing their full osteogenic potential for localised bone repair requires precise guidance and control. Given their pervasive presence, it is crucial to deliver growth factors that precisely direct MSCs towards osteoblastic differentiation (osteogenesis) at specific sites requiring enhanced bone regeneration.

1.5.1 Osteogenesis

Osteogenesis, is the process of new bone tissue formation [59]. This highly regulated and complex process is crucial not only during embryonic development and bone growth but also throughout adulthood for bone remodelling, fracture repair, and maintenance of skeletal integrity. Essentially, it is the mechanism through which osteoblasts derived from MSCs synthesise and mineralise the bone extracellular matrix. At the molecular level, osteogenesis is regulated by a multitude of signalling pathways and bioactive molecules. Growth factors, such as Bone morphogenetic proteins (BMPs) like BMP2, BMP6, BMP7 and BMP9, Insulin-like Growth Factors (IGFs), Fibroblast Growth Factors (FGFs), Wnt proteins like Wnt3a, and members of the Transforming Growth Factor-beta (TGF-β) superfamily among others play critical roles in inducing MSC differentiation into osteoblasts and promoting osteoblast activity [60-63]. Transcription factors, notably Runt-related transcription factor 2 (Runx2) and Osterix (Osx), act as master regulators, orchestrating the expression of genes essential for osteoblast differentiation and bone matrix formation [64, 65]. Among these molecules, BMP2 and Wnt3a play crucial roles in osteogenesis [66, 67].

BMP2 is a potent growth factor that directly induces MSCs differentiation into bone-forming osteoblasts, whereas Wnt3a is a key signalling protein that regulates osteoblast proliferation and differentiation.

1.5.2 Bone morphogenic protein-2

The principle of bone induction was first discovered by Marshall Urist in 1965 (Urist, 1965), who demonstrated that demineralised bone matrix could stimulate new bone formation. [68]. The specific protein BMP2 was later isolated and characterised by Wozney and colleagues in 1988 [69]. During biosynthesis proteolytic cleavage generates a 114 amino acid monomer that is glycosylated [70-72]. The biologically active form of this protein is a homodimer linked by disulphide bonds which form a cystine knot. This feature is conserved among members of the TGF-β family [73, 74]. As a member of this family, in order to transform MSCs into osteoblasts, BMP2 attaches to specific type I and type II serine/threonine kinase receptors, triggering both canonical and non-canonical signalling pathways. These pathways activate RUNX2 and osterix (Osx) (Figure 1.7). These transcription factors ultimately trigger osteogenic genes, such as alkaline phosphatase(ALP), type I collagen, and osteocalcin, which are essential for bone formation and mineralisation [65, 75]

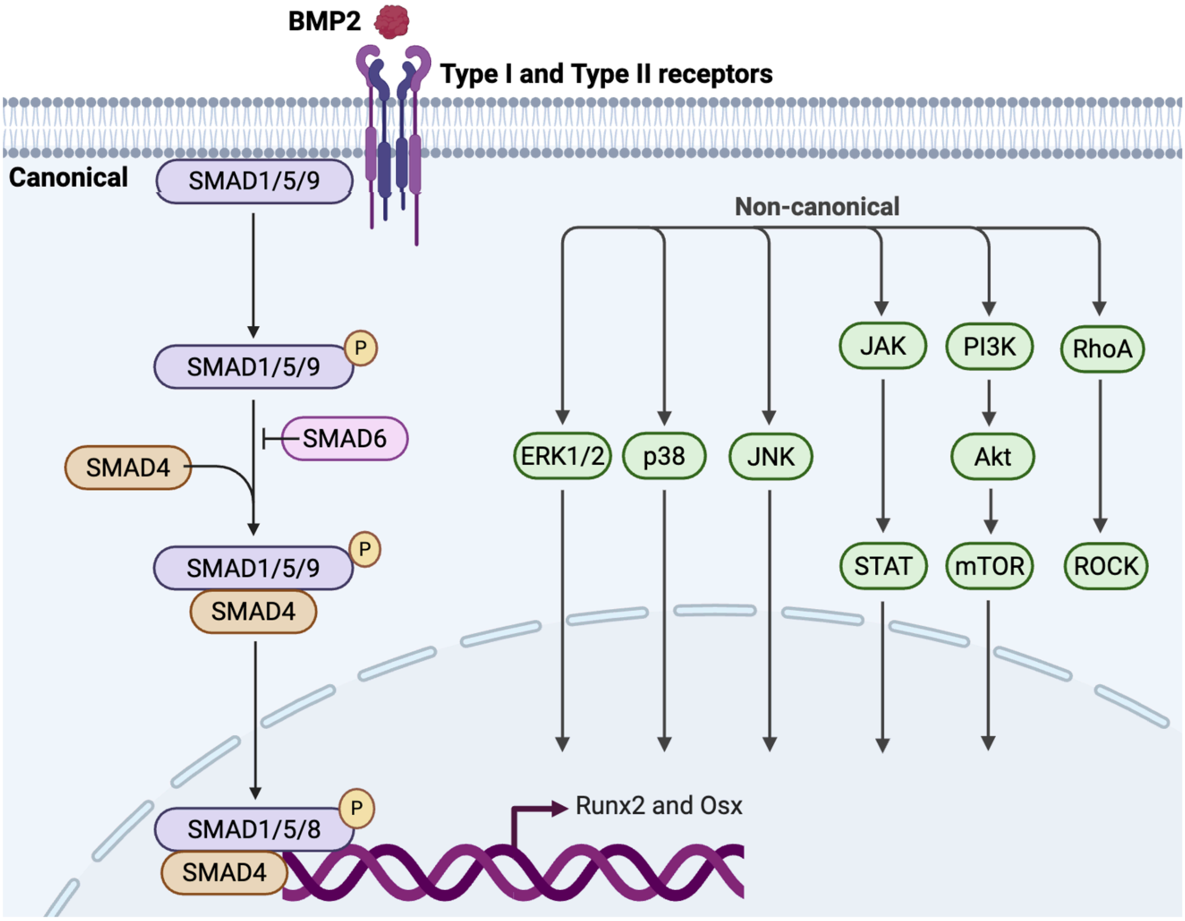

Figure 1.7: Schematic illustration of the BMP2 signalling pathways: Upon binding to Type I and Type II receptors, BMP2 activates both the Canonical Smad pathway (leading to phosphorylation of Smad1/5/9, complexing with Smad4, and nuclear translocation to regulate osteogenic genes such as Runx2 and Osx) and various non-canonical pathways (including ERK1/2, p38, JNK, JAK/STAT, and PI3K/Akt/mTOR pathways), all of which contribute to the activation of Runx2 and Osx, except for the RhoA/ROCK pathway which regulates the cytoskeleton of all these cellular responses. (Created with BioRender.com)

In 2002, the FDA (U.S. Food and Drug Administration) approved the therapeutic use of BMP2 in spinal fusion procedures through a product known as InFUSE [76]. InFUSE employs a concentration of BMP2 that is 20 times higher than the normal physiological concentration, in order to achieve therapeutic effects [77-79]. Although the use of InFUSE for spinal fusion has shown high success rates, it has also been associated with adverse side effects, including cases of dysphagia and respiratory problems [80]. Furthermore, in some cases patients experienced inflammation mediated osteoclast formation [81], swelling, and pain at the site of administration [82]. Other reported side effects include haematoma [83], ectopic bone formation [84], and nerve injury [85]. The direct use of BMP2 for therapeutic purposes has been associated with several complications [81], highlighting the need for a controlled and localised delivery system allowing dosing regimes with lower concentration [86].

The controlled delivery system used in this study aims to reduce the risk of side effects associated with high BMP2 concentrations while simultaneously promoting bone regeneration and healing, thereby offering a safer and more efficient method for BMP2 delivery. To effectively evaluate the amount of BMP2 released from the delivery system, it is essential to establish a reliable model capable of detecting bioactive BMP2.

1.5.3 *In vitro* models used for assessing bioactive BMP2

To effectively evaluate novel strategies for enhancing bone regeneration, particularly those involving the localised delivery of osteo-inducive molecules such as BMP2, appropriate experimental *in vitro* models are essential. While human MSCs are highly relevant for translational research, their osteogenic differentiation and subsequent bone formation *in vitro* can be a protracted and a complex process, often requiring weeks for proper evaluation. To enable a more immediate and efficient assessment of the preliminary delivery system's ability to evaluate bioactive BMP2, established immortalised cell lines, such as C2C12 mouse myoblasts, are frequently employed as *in vitro* cellular models [87].

1.5.3.1 *in vitro* human MSC model

MSCs are widely used in regenerative medicine research, while the use of primary cells *in vitro* presents notable challenges. Primary MSCs have a finite lifespan and undergo senescence as they replicate. A process which could alter their gene expression profiles and functional properties [88, 89]. In addition primary MSCs when isolated from a donor exhibit significant heterogeneity in terms of their surface markers, differentiation potential, and functional properties. This heterogeneity can make it challenging to isolate a pure population of MSCs, as there may be contamination from other cell types present in the tissue [90]. To overcome these limitations, the lab at the University of York immortalised human MSC clonal lines from a single donor (FH181), using human telomerase reverse transcriptase [91]. Multiple stable cell lines were generated from single cell derived colony. Four specific clones have undergone detailed characterisation, of which two (Y101 and Y201) are capable of differentiation, while the other two (Y102 and Y202) represent MSCs with enhanced immunomodulatory features but lack differentiation potential [91]. The two differentiating cell lines, Y101 and Y201, share similar gene expression profiles and possess the capacity for trilineage differentiation. However, Y101 cells display a predominant tendency towards osteogenic differentiation, while their efficiency in adipocyte differentiation is limited. In contrast, Y201 cell lines demonstrate tri-potency, enabling differentiation into multiple cell lineages [91]. Y201 cell lines were chosen as the osteogenic model for this study. While native MSCs are known to be a heterogeneous population, the tri-potency of Y201 cells provides a more representative model for evaluating multi-lineage potential compared to cell lines with more restricted differentiation capabilities, such as Y101. This approach, which uses a well-characterised and reproducible cell line, allows for consistent and reliable tests. By incorporating a cell line that maintains key multilineage properties, we can effectively assess the efficacy of our delivery system and ensure that our results are relevant to the fundamental characteristics and behaviour of MSC. Alongside this novel use of the Y201 cell line, it was important to include a well-established model to validate BMP2 responsiveness. Literature reports highlight the variability in the BMP2 response of human MSCs [92], making it essential to employ a system with proven sensitivity. Therefore, the C2C12 mouse myoblast cell line was used as a widely recognised and reliable *in vitro* model for the initial evaluation of BMP2 delivery systems.

1.5.3.2 *In vitro* mouse model

A widely recognised and valuable in vitro mouse model is the pluripotent mesenchymal precursor cell line C2C12, also known as a myoblast cell line. Derived from mouse skeletal muscle [93], C2C12 cells are an immortalised cell line known for their robust proliferative capacity and, critically for bone research, their unique ability to undergo a lineage switch from myoblasts (muscle precursors) to osteoblasts (bone-forming cells) in response to specific osteoinductive cues, particularly BMPs [94].

This characteristic makes C2C12 cells an ideal and highly responsive system for evaluating the osteo-inducive potential of biomaterials that deliver growth factors like BMP2 [87]. C2C12 cells offer high consistency and reproducibility in experiments. Their rapid cellular kinetics, including a faster proliferation rate and a relatively quick differentiation response compared to human MSCs, allows for a more accelerated and efficient initial screening of the delivery system's ability to provide biologically active BMP2. This facilitates a timely assessment of whether the delivered BMP2 is effectively engaging cellular machinery to initiate osteogenic differentiation.

Furthermore, C2C12 cells inherently possess and express the necessary cellular machinery, including specific receptors for key osteogenic signals. They express BMP type I and type II receptors, which are essential for binding BMP2 and initiating the downstream Smad signalling cascade critical for osteoblast differentiation [95]. The presence of these conserved signalling pathways ensures that the responses observed in C2C12 cells are mechanistically relevant to the broader context of osteogenesis, making them a reliable preliminary model for assessing the bioactivity of delivered BMP2 and its influence on osteogenic commitment before proceeding to more complex in vivo studies.

1.5.4 Limitations in current BMP2 delivery systems

Historically, the clinical application of recombinant human BMP2 has been hindered by significant delivery challenges. Direct injection into a defect site, while simple, is severely limited by the protein’s rapid diffusion and enzymatic degradation, resulting in a very short local half-life [76, 96]. To address the rapid clearance associated with this approach, various biomaterial carriers were developed to localise and prolong BMP2 delivery [97, 98].

Collagen-based sponges, for example, became widely adopted due to their inherent biocompatibility, biodegradability, and ability to mimic aspects of the natural extracellular matrix [76]. These sponges can physically entrap BMP2, creating a temporary reservoir for the protein. This principle formed the basis of early clinical products, such as InFUSE, which delivers BMP2 using an absorbable collagen sponge. However, even with this targeted system, achieving a therapeutic effect often requires supraphysiological doses [79]. Such high concentrations lead to inefficient protein utilisation and are associated with off-target effects, including inflammation and ectopic bone formation [81, 84].

A further limitation of these systems is the so-called “burst release” phenomenon, where a large proportion of the loaded BMP2 is released rapidly within the first few days, followed by a much slower and often sub-therapeutic release . This release profile results in an initial surge of high local concentrations that can trigger inflammation or undesired bone growth, whereas the subsequent low levels may fail to support sustained osteogenesis [99].

Hydrogels, composed of natural or synthetic polymers, offered another avenue for BMP2 delivery due to their tunable mechanical properties, injectability, and ability to encapsulate growth factors [98, 99]. While hydrogels can provide a more controlled release profile than simple sponges, challenges persist in achieving truly sustained and controlled release that precisely match the physiological requirements of bone healing. However, issues such as the rapid degradation of some hydrogels, potential protein denaturation during encapsulation, and difficulty in tailoring release rates over extended periods remain [97, 98].

Across these previous delivery methods, several limitations consistently hinder optimal therapeutic outcomes, including short half-life and rapid degradation, loss of bioactivity, unpredictable release, due to variability in material degradation rates and environmental conditions, that result in inconsistent BMP2 release. All combined, these limitations cause severe clinical challenges [100, 101].These persistent challenges underscore the critical necessity of developing advanced, sophisticated delivery systems capable of providing localised, sustained, and bioactive delivery of BMP2 at therapeutically relevant concentrations, thereby mimicking the natural healing cascade more effectively and improving clinical outcomes while minimising side effects.

While BMP2 has been extensively studied for its osteo-inducive potential, it is not the only signalling molecule of interest in bone regeneration. Other pathways, such as the Wnt signalling cascade, also play pivotal roles in regulating mesenchymal stem cell differentiation and bone formation. In this context, Wnt3a has emerged as a key growth factor with significant potential for enhancing osteogenesis. However, similar to BMP2, the effective delivery of Wnt3a poses unique challenges, necessitating innovative strategies to preserve its bioactivity and achieve a targeted release.

1.6 Wnt3a

Wnt3a is a member of the Wnt family of 19 known secreted glycoproteins. These highly conserved, cystine-rich proteins regulate a wide range of biological processes [102]. Notably, Wnt proteins play a foundational role in embryonic development, influencing crucial events such as axis formation and tissue patterning. In adults, this protein continues to be a key regulator of processes like cell proliferation, differentiation, and tissue homeostasis, including its vital function in bone [102, 103] and differentiation during embryonic development and tissue homeostasis [104]. There are two major branches of Wnt signalling: canonical (β-catenin-dependent) and non-canonical (β-catenin-independent) pathways (**Figure 1.8**).

In the canonical pathway, one of the most extensively studied Wnt signalling routes, Wnt ligands bind to the Frizzled (Fzd) receptor and low-density lipoprotein receptor-related protein 5/6 (LRP5/6) co-receptors. This binding leads to the activation of Dishevelled (Dvl), a cytoplasmic phosphoprotein that mediates downstream signalling and subsequently inhibits the β-catenin destruction complex. This complex comprises glycogen synthase kinase-3β (GSK-3β), Axin scaffold protein, adenomatous polyposis coli (APC) tumour suppressor, and casein kinase Iα (CKIα). Inhibition of this complex prevents the phosphorylation and degradation of β-catenin, allowing it to stabilise and accumulate in the cytoplasm. The accumulated β-catenin then translocates into the nucleus, where it interacts with T-cell factor/lymphoid enhancer-binding factor (TCF/LEF) transcription factors to regulate the expression of genes involved in cell proliferation and osteogenesis [62, 105].

Wnt signalling is not limited to the canonical pathway though; non-canonical pathways include the Wnt/Planar Cell Polarity (PCP) and Wnt/Ca^{2+} signalling cascades. These pathways do not involve β-catenin stabilisation. Instead, they activate small GTPases such as Rac1 and RhoA, as well as downstream effectors like JNK and ROCK, leading to cytoskeletal remodelling and activation of transcription factors such as AP-1. The Wnt/Ca^{2+} pathway additionally activates phospholipase C (PLC), resulting in PIP2 hydrolysis, IP3-mediated Ca^{2+} release, and activation of protein kinase C (PKC) and NFAT, which influence gene transcription [62, 105].

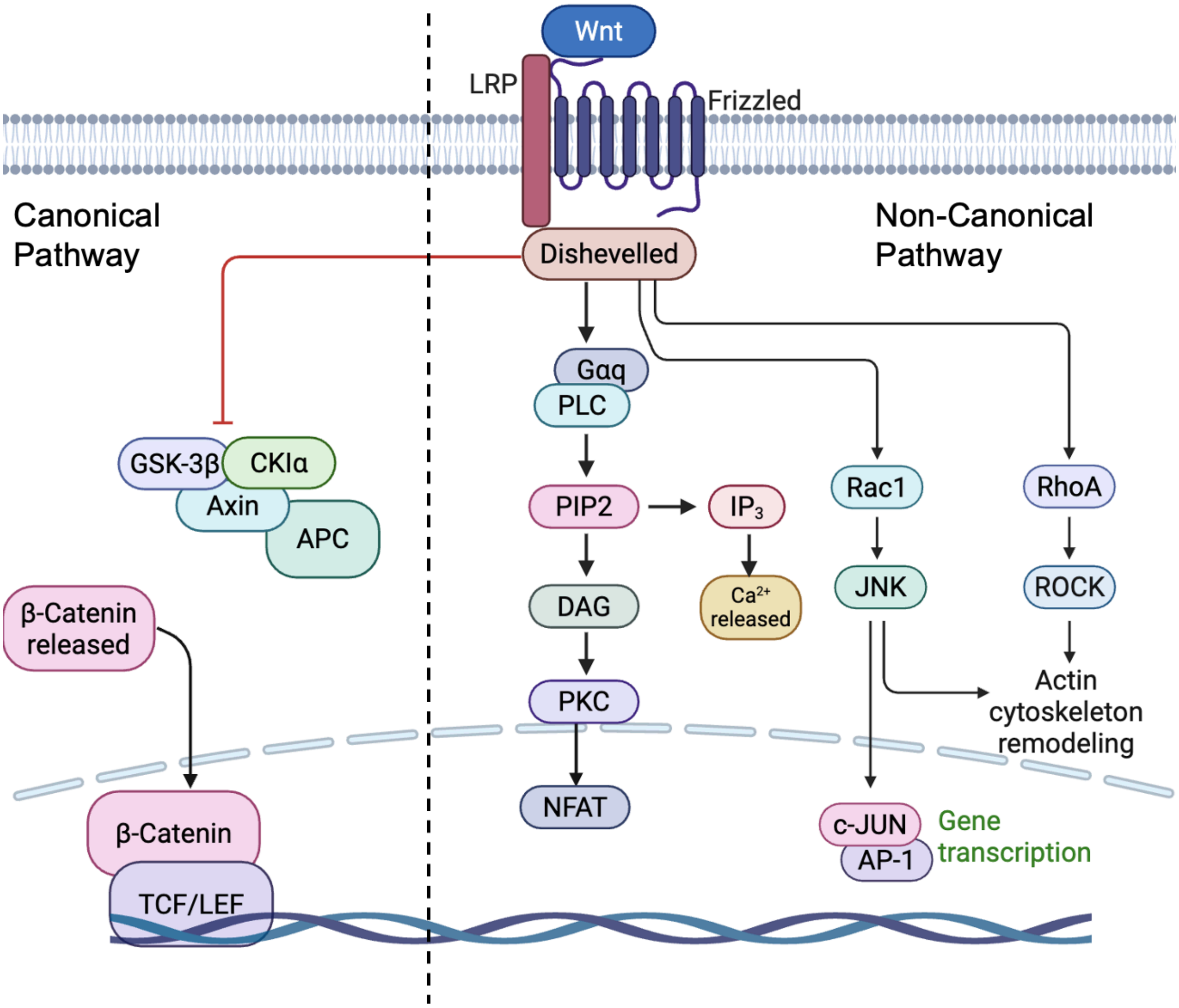

Figure 1.8: Detailed overview of the Wnt signalling pathways: This schematic illustrates the two primary branches: the Canonical Wnt Pathway (left) and the Non-Canonical Wnt Pathways (right). In the Canonical Pathway, Wnt ligands bind to Frizzled receptors and LRP co-receptors, leading to the activation of Dishevelled. Activated Dishevelled inhibits the destruction complex (comprising GSK-3β, Axin, and APC), preventing the phosphorylation and degradation of β-catenin. This allows β-catenin to accumulate in the cytoplasm, translocate to the nucleus, and bind to TCF/LEF transcription factors, ultimately promoting gene transcription**.** One branch involves dishevelled activation of Gαq, which then activates PLC, leading to the hydrolysis of PIP2 into DAG and IP3. IP3 triggers the release of Ca2+ from intracellular stores, activating PKC and subsequently NFAT, which influences gene expression. Another non-canonical branch involves dishevelled activating Rac1 and JNK, which can then lead to the activation of c-JUN and AP-1, resulting in gene transcription. The

third non-canonical pathway involves Dishevelled activating RhoA, which subsequently activates ROCK, leading to actin cytoskeleton remodelling. (Created with BioRender.com)

1.6.1 Role of Wnt3a in osteogenesis

Several Wnt proteins are key regulators of bone formation and osteogenic differentiation. Among these, Wnt3a, a potent ligand of the canonical Wnt/β-catenin signalling pathway, is a well-documented driver of osteogenesis and bone regeneration [106]. Its critical role has been demonstrated in numerous studies, revealing its ability to regulate the fate and function of human MSCs and osteoblasts. For instance, a study showed that Wnt3a stimulation enhances the expression of critical osteogenic markers, including ALP and osteocalcin. Additionally, Wnt3a signalling has been demonstrated to increase the mineralisation capacity of MSCs, facilitating the development of a mineralised extracellular matrix, a hallmark of mature bone tissue [106, 107].

Interestingly, Wnt3a not only promotes osteoblast differentiation but also plays a role in inhibiting adipogenesis, the differentiation of MSCs into fat cells [108]. This dual function ensures that progenitor cells are directed towards an osteogenic lineage rather than an adipogenic fate, a critical switch in maintaining bone mass and density. Dysregulation of Wnt signalling, including Wnt3a activity, has been implicated in various bone disorders, such as osteoporosis, where reduced Wnt activity leads to decreased bone formation [109]. Exogenous application of Wnt3a protein has been shown to stimulate osteogenic differentiation of MSC in culture [110]. Similarly, an *in vivo* study has shown that local application of Wnt3a enhances bone regeneration in a mouse model of post-traumatic osteomyelitis by increasing osteogenesis, promoting osteoblast genesis, reducing osteoclast activity, effectively restoring bone healing [111].

Gene expression analysis was conducted to establish Wnt3a’s effects on C3H10T1/2 mouse MSC differentiation. This study identified 477 genes regulated by Wnt3a and specifically focused on its impact on osteoblast and adipocyte differentiation. Consistent with Wnt3a's role in inhibiting adipogenesis, the treatment suppressed the expression of 12 adipocyte-related genes. For osteoblast differentiation, Wnt3a upregulated 13 genes associated with promoting osteoblast differentiation and function like BMP4 [112].

Another study demonstrated that increased Wnt3a expression induced by spinal loading was associated with improved bone remodelling and angiogenesis *in vivo*. In complementary *in vitro* experiments, silencing Wnt3a using siRNA led to decreased osteoblast differentiation and mineralisation and increased osteoclast formation, migration, and adhesion in cultured cells [113]. In experimental settings, Wnt3a has been used to enhance bone formation, both *in vitro* and *in vivo*. For instance, exogenous application of Wnt3a protein has been shown to stimulate osteogenic differentiation of stem cells in culture [107]. Moreover, animal studies have indicated that activation of Wnt3a signalling can lead to increased bone formation and improved healing of bone defects [111]. These findings underscore the potential of Wnt3a as a therapeutic target for bone regeneration.

1.6.2 Development of Wnt3a delivery systems

The intrinsic instability and short half-life of Wnt3a protein pose significant challenges for its therapeutic application in bone regeneration [114]. To overcome this, researchers have developed various advanced delivery systems to protect the protein and ensure its sustained and localised release. A prominent approach involves the use of liposomal nanoparticles. For example, one study successfully encapsulated Wnt3a into liposomal vesicles and delivered them to skeletal defects in aged mice and rabbits. This method effectively shields Wnt3a from degradation and allows for its controlled delivery, resulting in enhanced bone formation in aged bone grafts [67].

Another study reported that local delivery of Wnt3a via a polycaprolactone-based "Wnt3a bandage" enhanced bone regeneration in critical-size calvarial defects across different age groups of mice. The Wnt3a-bandage increased the proportion of CD90+ osteoprogenitor cells in the defect site and significantly improved bone repair in adult mice to levels comparable to young mice [115]. In another study, an absorbable collagen sponge was used as a carrier to deliver 2.0 µg of recombinant mouse Wnt3a protein. When combined with guided bone regeneration, this approach showed promising results in promoting bone formation in a rat critical-size calvarial defect model after 7 days of healing [116].

This study demonstrates that PEGylated liposomes can effectively associate with and deliver active Wnt3a protein to human bone marrow cells *in vitro*, particularly to skeletal stem cells. The researchers showed that Wnt3a-loaded PEGylated liposomes activated Wnt signalling and promoted the expansion of osteoprogenitors, highlighting their potential for systemic administration to enhance bone repair [117]. Together, these studies highlight the critical importance of a robust delivery system in harnessing Wnt3a's full therapeutic potential for bone repair.

1.7 Previous studies underpinning the current work

Despite the above mentioned delivery strategies, all the systems lacked a controlled, on-demand release mechanism. Therefore, a major focus in our laboratory has been to develop a novel delivery system with a remotely triggered release capability. One of the previous studies in our laboratory focused on developing SPIONs. The SPIONs used in this study were synthesised via a modified polyol process to achieve water solubility. These SPIONs were then coated with the temperature-sensitive polymer poly(N-isopropylacrylamide) (PNIPAM) which was synthesised using the atom transfer radical polymerisation (ATRP) method. To enable the attachment of PNIPAM to the SPIONs, a terminal nitrocatechol group, nitrodopamine (NDA), was incorporated into PNIPAM via a peptide link. NDA-PNIPAM actively binds to SPIONs, yielding water-soluble PNIPAM-coated SPIONs designed for the controlled delivery of proteins, such as Wnt3a. the study used a novel approach where 1 µg of Wnt3a was used to encapsulate in 1 mg of PNIPMAM-coated SPIONs. A key finding was that the encapsulated Wnt3a remained inactive until its release was magnetically triggered. Upon release, the protein enhanced MSC proliferation. Furthermore, the release of Wnt3a required the presence of a competitor protein. Foetal bovine serum (FBS) served as a competing protein source, confirming that Wnt3a could be released even in the presence of other proteins, as would be the case in a biological system. The cumulative release observed was approximately 40 ng [17].

This study is the first to report the magnetically triggered release of proteins entrapped in PNIPAM-coated nanoparticles. It highlighted a promising strategy for protecting bioactive proteins during transit and releasing them in a controlled manner [17]. However, a significant limitation was the phase transition temperature of the PNIPAM-coated SPIONs (32 °C), which is below physiological temperature, thereby limiting their in vivo application. To address this issue, a subsequent study focused on developing SPIONs coated with poly(N-isopropylmethacrylamide) (PNIPMAM), a polymer with a higher transition temperature. PNIPMAM was synthesised using reversible addition–fragmentation chain-transfer (RAFT) polymerisation, and SPIONs were prepared via thermal decomposition of iron(III) acetylacetonate. The SPIONs were then coated with PNIPMAM, similar to the previous study by using NDA yielding water soluble PNIPMAM-coated SPIONs with a precipitation temperature above 44 °C, a significant improvement over the previous system allowing for *in vivo* use [18].

This study demonstrated the potential of PNIPMAM-coated SPIONs by successfully encapsulating several proteins, including apotransferrin (TRF), green fluorescent protein (GFP), and bovine immunoglobulin G (IgG). To investigate protein release, various competitor proteins were tested, such as RNaseA, ovalbumin (OVA), bovine serum albumin (BSA), and bovine IgG. The findings highlighted the critical role of glycosylation of the competitor proteins in the release process. For example, TRF release varied from approximately 5% (21 ng of 400 ng loaded) with RNase B to approximately 44% (175 ng) with OVA as the competitor. Similarly, for IgG, approximately 19% (150 ng of 800 ng loaded) was released when OVL was used as a competitor [18].

A key observation was that magnetic heating resulted in more efficient protein release than conventional heating, without significantly increasing the bulk solution temperature. This demonstrates the potential of PNIPMAM-coated SPIONs for targeted protein delivery, as they can efficiently encapsulate and release proteins in response to magnetic stimuli.

The current study builds upon these foundational studies by employing PNIPMAM-coated SPIONs to further investigate and enhance their applicability in targeted bioactive protein delivery in the field of biology.

1.8 Aims and objectives

To build on the previous studies described above, the present work aimed to investigate the potential of PNIPMAM-coated SPIONs as a delivery system for bioactive molecules. This approach involves encapsulating model osteogenic growth factors within the polymer PNIPMAM coated onto the surface of SPIONs. This thermally responsive polymer coating is designed to facilitate controlled protein release slightly above human body temperature, ensuring the proteins remain intact until their release triggered. Since this was the first time PNIPMAM-coated SPIONs were used for bioactive protein release, bulk temperature increase was employed for these preliminary experiments to mimic the heat generated by magnetic induction. This approach provided a controlled environment to study the polymer's phase transition and to assess the bioactivity of the released proteins. (Figure 1.9).

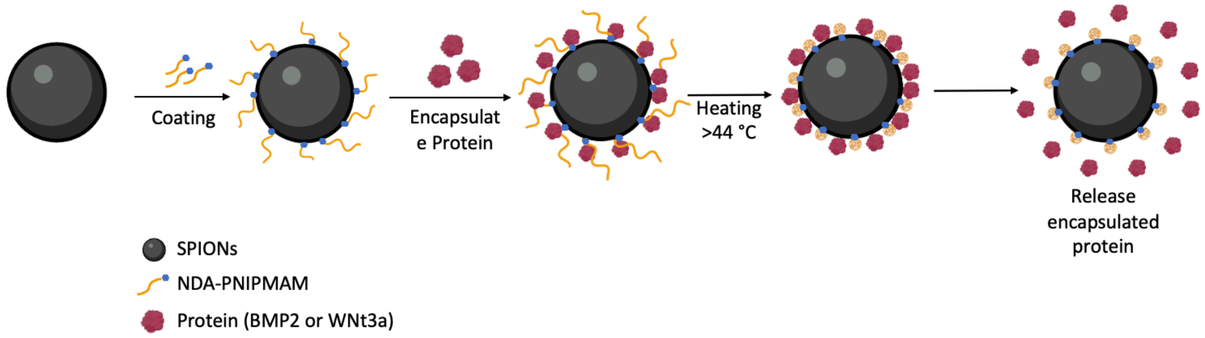

Figure 1.9: **Protein encapsulation and release from PNIPMAM-coated SPIONs:** Step-by-step schematic depicting the coating of SPIONs with NDA-PNIPMAM, subsequent encapsulation of proteins (BMP2 or Wnt3a) within the NDA-PNIPMAM coated SPIONs, and their temperature-triggered release upon heating above 44 °C. (Created with BioRender.com). This research builds on previous work from our laboratory that established the synthesis of PNIPMAM-coated SPIONs. My first aim was replicate this previous synthesis to ensure reproducibility. I then made fine adjustments to the process to reduce variability and ensure consistent polymer-coated SPIONs. With the PNIPMAM-coated SPION preparations successfully synthesized. A key objective was to evaluate the potential toxicity and physiological impact of PNIPMAM-coated SPIONs using an *in vitro* model relevant to bone regeneration. The Y201 cell line was chosen for this purpose. I assessed the nanoparticles' impact on both Y201 cell proliferation and differentiation.

Finally the central objective was to investigate the encapsulation and release efficiency of two bioactive proteins. Firstly, BMP2, which had not previously been tested with the PNIPMAM-coated SPIONs. This required development of a reliable *in vitro* model and a method for quantifying both encapsulated and released BMP2 from the PNIPMAM-coated SPIONs. To find a suitable model, two cell lines, Y201 and C2C12, were screened using various assays.

Secondly, also examined the delivery of Wnt3a, which had not previously been tested with PNIPMAM-coated SPIONs. Since Wnt3a had already been used with PNIPAM-coated SPIONs, I employed the same in vitro model to assess its encapsulation and release from PNIPMAM-coated SPIONs. Previous work had shown that Wnt3a has a short half-life, particularly at temperatures above 37 °C, suggesting it might not survive the temperature regime involved in the encapsulation and release process using this new PNIPMAM-coated SPIONs. I therefore tested its stability, and as expected, my experiments confirmed that

Wnt3a denatured under these conditions. To address this, I focused on improving its thermal stability by testing various additives. I evaluated its impact on the phase transition of PNIPMAM-coated SPIONs. Following this careful optimisation, I proceeded with encapsulation and release experiments in the presence of the additive and competitor proteins to assess the preliminary *in vitro* performance of the delivery system.

Chapter 2

2. Materials and Methods

2.1 Antibodies and proteins used

The following antibodies were used in this study: polyclonal rabbit psmad/1/5/9 (Cell Signalling Technology, 7074S, 1:500), smad antibody (Proteintech, 66559-1, 1:4000) ,anti-rabbit HRP (CST, 7074S, 1:2000), anti-mouse HRP (Jackson, 115-035-146, 1:2000).
BMP2 (Antibodies.com, A61457), Wnt3a (Proteintech, HZ-1296), Norrin (R&D Systems, 3497-NR) competitor protein : bovine IgG (Sigma-Aldrich, I5506), human apotransferrin (Sigma-Aldrich, T1147), RNase B (Fisher Scientific, AAJ62334MC). ovalbumin

2.2 Nanoparticles synthesis

The synthesis and assembly of the nanoparticles in this study were adapted from previously reported protocols, which served as the foundation for the coating and functionalisation strategies developed for this study [18]. Minor modifications were introduced to improve reproducibility and to optimise the quality of the final coating.

2.2.1 Synthesis of SPIONs

Synthesis of 16 nm IONPs was adapted from a previous study. In a typical synthesis, Fe(acac)$_3$ (3.5 g,10 mmol), oleyalamine(OAm) (5.34 g, 20 mmol) and oleic acid (OA) (2.8 g,10 mmol) were weighed in a three-neck round bottomed flask (RBF). It was fitted with a condenser and the reaction mixture was heated to 150 °C under a positive gas flow and kept at this temperature for 15 min. The temperature was then raised to 240 °C at a heating rate of 3 °C /min and kept at this temperature for 3 h. The temperature was later increased to 300 °C with the same heating rate and kept for 1 h. The mixture was constantly stirred under argon atmosphere. After this the mixture was allowed to cool at room temperature then dissolved in toluene and washed with excess amount of ethanol this process was repeated 3 times, then the nanoparticles were suspended in toluene and stored at 4 °C. The synthesised nanoparticles were subsequently imaged using transmission electron microscopy (TEM) to determine morphology and size distribution (**Figure 2.1**).

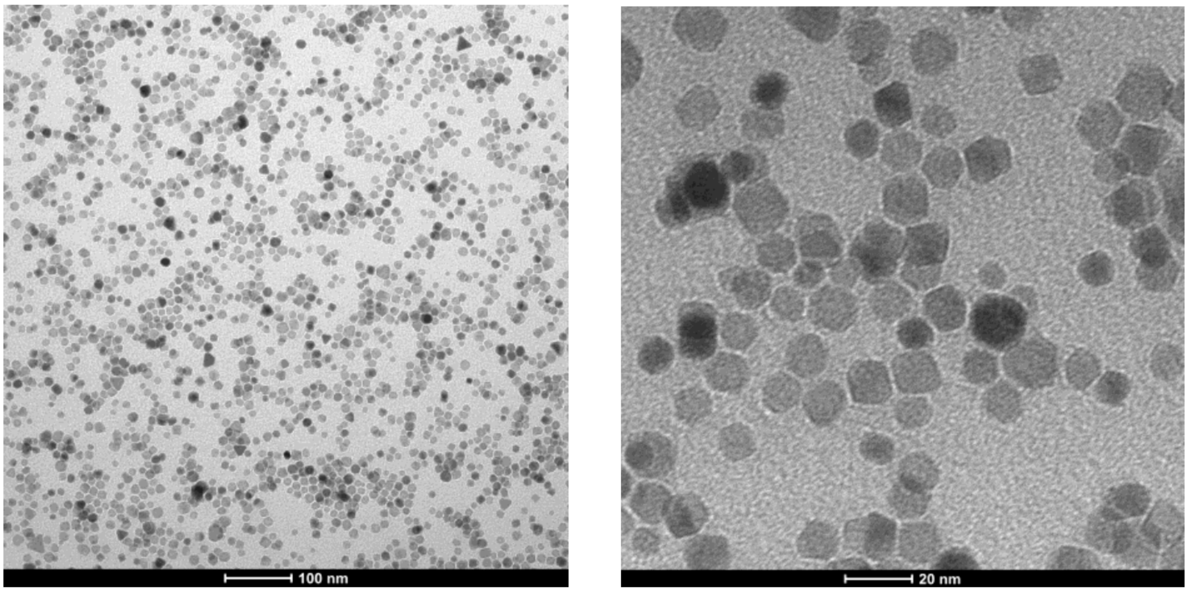

Figure 2.1: TEM images of synthesised SPIONs: TEM analysis revealed an average nanoparticle diameter of 14 ± 0.3 nm (mean ± standard deviation, n = 100).

2.2.2 Synthesis of poly(NIPMAM)

A round bottom flask containing a reaction mixture of 5 g *N*-isopropylmethacrylamide NIPMAM and 36 g of 2-[[(dodecylthio)thioxomethyl]thio]-2-methylpropanoic acid which is chain transfer agent (CTA), dissolved in 10 ml isopropanol (IPA) was degassed using Argon for 20 mins and sonicated for 40 mins. To this 1 ml of Azobisisobutyronitrile of 50 mg dissolved in 5 ml IPA and degassed in Argon. After addition the solution was stirred at 70°C in oil bath under Argon atmosphere for 24 hours. The reaction was quenched stopped after 24 hours by exposing the mixture to oxygen. IPA was removed using a rotary evaporator, the remaining product was dissolved in 50 ml of THF and precipitated using n-Pentane in the ratio (1:9) and centrifuged at 3800 g for 5 minutes. The pellet was dissolved in THF, dried using rotary evaporator and stored at room temperature.

The dried product was later redissolved in dH_2O and analysed using nano-differential scanning fluorometry (nanoDSF), which revealed a thermal transition with an LCST above ~45 °C (**Figure 2.2**).

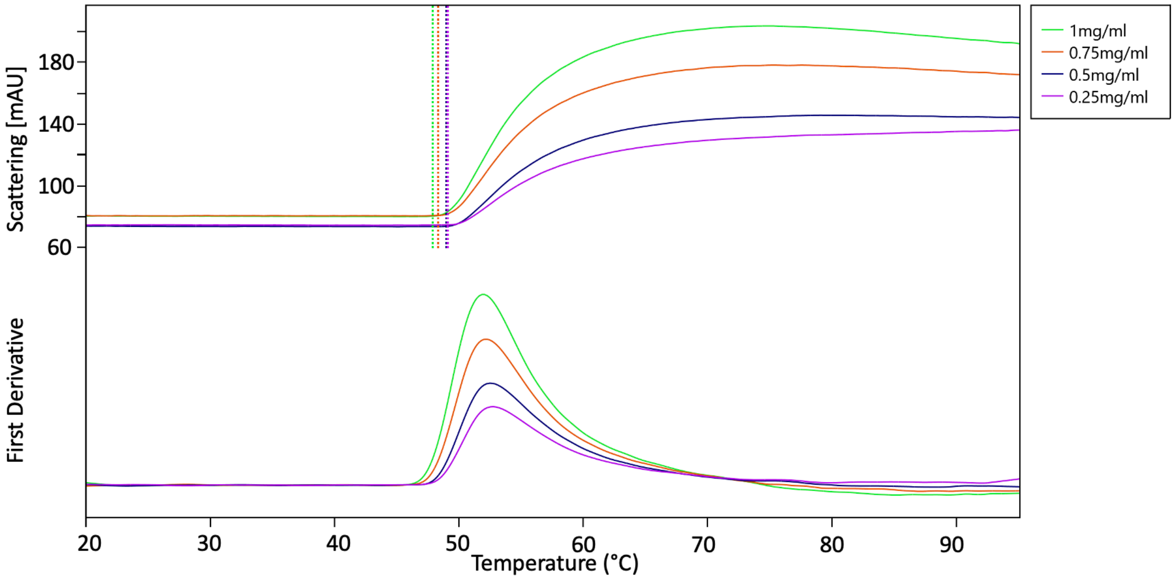

Figure 2.2: nanoDSF analysis of PNIPMAM: nanoDSF thermograms showing scattering intensity (top) and corresponding first derivative (bottom) as a function of temperature for nanoparticle dispersions at the indicated concentrations. The thermal transition associated with the LCST is evident from the increase in scattering intensity, with derivative plots used to identify the transition midpoint. The LCST was consistently observed above ~45 °C.

2.2.3 Nitrodopamine (NDA) synthesis

For a 2 g scale reaction, concentrated sulphuric acid (960 µL, 17 mmol) in dH_2O (10 mL) was cautiously added dropwise to a cooled solution of dopamine hydrochloride (2 g, 10 mmol) and sodium nitrite (1.52 g, 22 mmol) in dH_2O (25 mL) maintained in an ice bath. A yellow precipitate formed, and the mixture was stirred overnight at room temperature. The precipitate was collected by Büchner filtration, washed with water and methanol, and afforded 2-nitrodopamine hydrogen sulphate. Purification was achieved by recrystallisation: the crude product was dissolved in dH_2O (50 mL) and heated to 70 °C, yielding small brown crystals, which were dried in the heating oven at 70 °C.

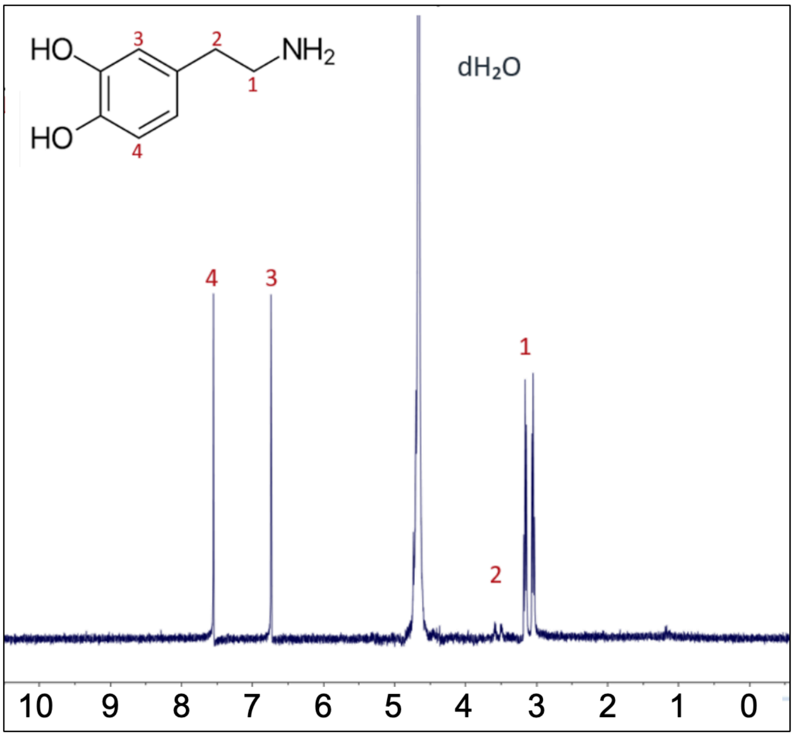

Figure 2.3: ^{1}H NMR spectrum of NDA recorded in D_2O: Characteristic NDA peaks were observed at δ =t, 2.9–3.1 ppm (1), t,3.45–3.74 ppm (2), 6.87 ppm (3), and 7.65 ppm (4).

2.2.4 NDA functionalized PNIPMAM (NDA-PNIPMAM) synthesis

PNIPMAM (1 g), HBTU (152 mg, 2-(1H-benzotriazol-1-yl)-1,1,3,3-tetramethyluronium hexafluorophosphate), and N,N-diisopropylethylamine (DIPEA, 60 µL) were added to a 50 ml RBF equipped with a magnetic stir bar. The mixture was dissolved in 8 mL of dry DMF. Separately, NDA (198 mg) was dissolved in 2 mL of dry DMF in a sample vial, followed by the addition of DIPEA (117 µL). This solution was then transferred under inert conditions to the RBF containing the polymer, and the reaction mixture was stirred at room temperature for 3 days. After that the solution was acidified with a few drops of 2 M HCl, and NDA-PNIPMAM was precipitated by adding excess diethyl ether (1:9 ratio). The suspension was centrifuged at 3800 g for 10 minutes, and the supernatant was discarded. The resulting pellet was redissolved in 20 ml water overnight and centrifuged again at 3800 g for 10 minutes. The supernatant was transferred to a pre-soaked 12,000 kDa MWCO dialysis membrane and dialysed against dH_2O until the yellow colour from excess free NDA was completely removed. The dialysed NDA-PNIPMAM solution was then transferred into 2 mL microtubes and centrifuged at 21,000 g for 10 minutes. The final supernatant was collected, transferred to an RBF, dried under reduced pressure using a rotary evaporator, and stored at room temperature until further use for coating.

2.2.5 PNIPMAM-coated nanoparticle synthesis

OA/OAm-capped SPIONs (30 mg) and NDA-PNIPMAM (450 mg) were suspended in 5 mL of dry DMF. The mixture was sonicated for 5 hours at room temperature and subsequently left rotating overnight on a rotary evaporator at room temperature. Nanoparticles were precipitated by the addition of diethyl ether (1:9 ratio) and collected by centrifugation at 3800 g for 10 minutes. The supernatant was discarded, and the pellet containing the particles was redispersed in dH_2O by sonication. This suspension was then ultracentrifuged at 100,000 g for 1 hour. The supernatant was removed, and the resulting PNIPMAM-coated SPION pellet was dissolved in water and stored at 4 °C.

2.3 In vitro analysis

2.3.1 Cell Culture

2.3.2 Cell culture components were purchased from Invitrogen, Y201 cells and C2C12 was cultured in Dulbecco's modified Eagle's medium (DMEM), 4.5 mg/L glucose, pyruvate, no glutamine, supplemented with 10% fetal bovine serum (FBS), 1% penicillin/streptomycin and 1% Gluta-Max. For routine subculture, all cell lines were incubated at 37°C, 5% CO_2. Experiments in this study were performed using Y201 cells between passages P77–P97 and C2C12 cells between P10–P50.Proliferation assay

Y201 cells were seeded overnight at low density 3000 cells per well in a 96-well plate. 0.5 mg of polymer-coated SPIONs (100 µL, 5 mg/mL in dH2O) were washed twice with 1 mL of diethyl ether, with each washing step involving centrifugation at 21,000 g for 20 minutes to separate the nanoparticles. The supernatant was carefully removed after each centrifugation, and the nanoparticles were resuspended in 1 ml of DMEM. The nanoparticles were washed twice more by resuspending them in 1 mL of DMEM, followed by centrifugation at 21,000 g for 20 minutes. Finally, the polymer-coated SPIONs were resuspended in 100 µL of DMEM. Desired concentrations of the polymer-coated SPIONs were prepared by diluting the stock suspension in DMEM and were then added to the cells.

2.3.2.1 Deep blue cell metabolic activity assay of the viable cells

After treatment, the cells were assessed for at 24, 48, and 72 hours using the Deep Blue Cell Viability kit (cat. no. 424701, BioLegend). The treatment media were removed, and fresh media were added (135 µl per well). To each well, 15 µl of the viability dye was added individually, and the plate was then incubated for 4 hours at 37 °C. After the incubation period, 100 µl of the mixture from each well was transferred to a black 96-well plate. Fluorescence intensity was measured using a CLARIOstar® plate reader (BMG) at an excitation wavelength of 530 nm and an emission wavelength of 590 nm.

2.3.3 Western blot

Y201 cells were seeded overnight in 24-well plate at a density of 57,000 cells per well. and treated with various concentrations of BMP2 after the treatment at the cell were immediately put on ice and washed with 1X PBS twice and then was lysed with 100 µL of Laemmli SDS-PAGE sample buffer (150 mM Tris pH 6.8, 8% w/v SDS, 166 mM DTT) and boiled for 5 min at 95°C. For further analysis the lysed protein samples were then stored at -20 °C .

2.3.4 The samples were then protein separation using SDS-PAGE gel electrophoresis. Resolved proteins were transferred to nitrocellulose membrane. using semi-dry transfer (Bio-Rad). Membranes were then blocked at room-temperature for 1 h in 5% (w/v) milk powder for Smad blots and tubulin for p-smad 5% (w/v) BSA dissolved in TBS-T was used. After being washed six times with TBS-T or PBS-T, the membranes were incubated for 1 h at room temperature with the HRP-conjugated secondary antibody, diluted in blocking buffer. The membranes were washed a further six times and were then imaged using an iBright Imaging System (Thermo Fisher Scientific) after incubation with the chemiluminescent substrate. For normalization, p-Smad blots were stripped using stripping buffer for 15 min, washed, re-blocked, and re-probed with an anti-tubulin antibody. Protein levels were subsequently quantified using .ImageJ software was used to quantify protein levels, with tubulin serving as the loading control.*in vitro* osteogenic differentiation assay

Cells were seeded at an equal density of $1x10^4$ cells per well in four 96-well plates, with each plate representing a separate time point. The cells were cultured overnight to achieve attachment post-seeding and then cultured in osteogenic medium containing 50 µg/ml

L- ascorbic acid-2-phosphate, 5 mM β-glycerophosphate, and 10 nM dexamethasone. The osteogenic and non-osteogenic basal condition was supplemented with medium containing 10% FBS for cells and FBS with penicillin-streptomycin, the latter was used as a control group. The medium was changed every 3 days.

2.3.4.1 ALP activity assay

At three-day intervals, including a day zero time point, cells were washed with 0.2 M carbonate buffer (pH 10.2). 150 µL of lysis buffer (0.1% Triton X-100 in 0.2 M carbonate buffer) was added to the cells and stored at −80 °C until all the timepoints were collected . To ensure complete lysis, cells were subjected to 1 freeze–thaw cycle (−80 °C/37 °C), after which plates containing cells treated with nanoparticles were centrifuged for 15 minutes. After the freeze thaw cycle the cells were pipetted up and down to ensure they are completely lysed and then 50 µL of the 150 µL supernatant was transferred to a clear 96-well plate, and pNPP substrate was added. Plates were incubated at 37 °C for 1 hour, after which the absorbance of the resulting pNP was measured using a microplate reader at 405 nm. pNP concentration (µmol/mL), reflecting ALP activity.

2.3.4.2 Propidium Iodide (PI) Assay

The remaining 50 µL of fully lysed cells was transferred to black-bottom 96-well plates. PI (P3566, ThermoFisher) was diluted to 50 µg/mL in 1× PBS to prepare a working stock, and 50 µL of this solution was added to each well. Plates were gently shaken, wrapped in foil, and incubated for several minutes. Fluorescence was measured using a CLARIOstar® plate reader at 485 nm excitation and 538 nm emission. DNA concentration (µg/ml) was determined from a standard curve. Finally, ALP activity (µmol/ml of pNP) was normalised to DNA content (µg/ml of DNA) for each well, expressed as µmol pNP/µg DNA.

The PI assay was utilized to quantify DNA content for the normalization of ALP activity. While PI is traditionally used as a viability dye in flow cytometry or fluorescent imaging, its application for normalizing DNA content in this specific context and 96-well format offers a cost-effective and reliable alternative to more expensive commercial kits, such as PicoGreen. This method overcomes the limitations of normalizing to total protein content, which can fluctuate significantly due to varying treatment conditions. The PI assay accurately measured an increase in fluorescence intensity that directly correlates with a corresponding increase in both cell number and DNA concentration, confirming its reliability for quantifying DNA content in this experimental setup (**Figure 2.4**). Although the assay is less sensitive at very low DNA concentrations, it is highly effective for quantifying DNA amounts above 1 µg/mL. This makes it a suitable and accurate method for normalizing results in the 96-well format, ensuring that any differences in ALP activity are a true reflection of the experimental treatment .

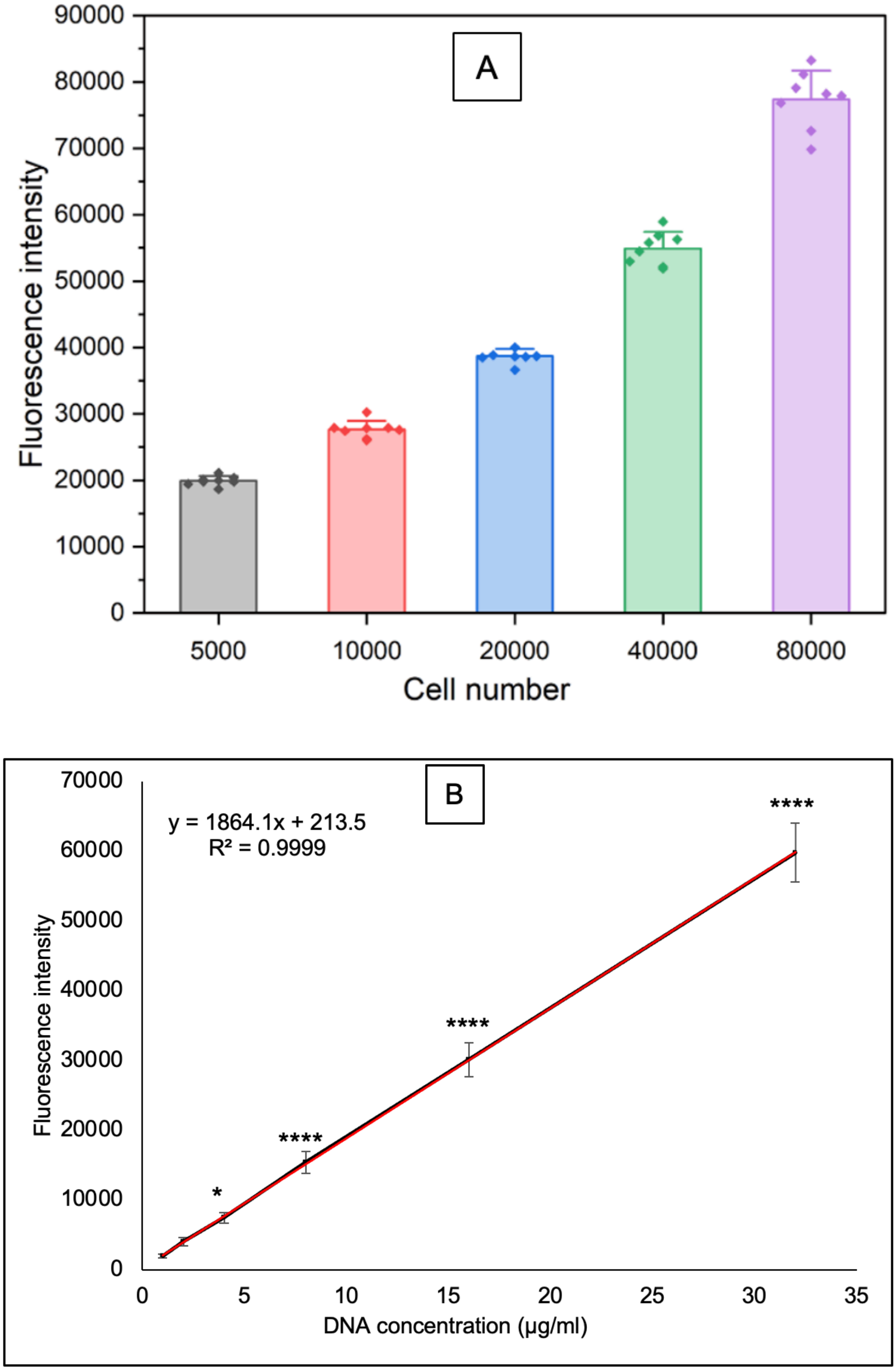

Figure 2.4: Validation of the PI assay for DNA quantification: (A) demonstrates that the

fluorescence intensity of the PI signal correlates directly with an increase in cell number (average of 10 technical replicates(n).). (B) presents a standard curve, plotting fluorescence intensity against known DNA concentrations (experimental repeats(N) N=3).

2.3.5 Preparation of protein encapsulation

Prior to encapsulation, 0.5 mg of polymer-coated nanoparticles (100 µL, 5 mg/mL PNIPMAM-coated SPIONs in dH_2O) were washed with diethyl ether (1 mL). Nanoparticles were separated by centrifugation (21,000 g, 20 min), the supernatant was discarded, and the pellet was washed three times by resuspending and pelleting in 1 ml physiological buffer (20 mM HEPES, 100 mM NaCl, pH 7.4) before final resuspension in 100 µL.

The washed nanoparticles were then incubated with the 1 µg protein to be encapsulated. The suspension with the nanoparticles and the protein to be encapsulated was placed on a heat block at 45 °C for 10 min. Samples were subsequently incubated on a shaker at room temperature for 2 h. Nanoparticles were separated by centrifugation, and the supernatant was retained as the unloaded (UL) protein fraction.

To remove excess unbound/free protein, nanoparticles were washed with 100 µL of competitor protein solution (10 mg/ml in physiological buffer) and incubated for 1 h at room temperature on a wheel. Nanoparticles were separated by centrifugation, and the supernatant was retained as the first wash fraction. This process was repeated 5–10 times, with each wash solution collected for further analysis. Protein-loaded nanoparticles were then immediately used for the release experiments.

2.3.6 Protein release assays

Protein-loaded PNIPMAM-coated SPIONs (0.5 mg) were subjected to temperature variation in 100 µL of competitor protein solution (10 mg/mL in physiological buffer). To study the release triggered by heating above the polymer LCST without magnetic stimulation, nanoparticles were suspended in competitor protein solution and incubated at 45 °C for 15 min and 60 min. Samples were regularly agitated, and at designated time points, nanoparticles were magnetically separated and 15 µL of supernatant was removed for analysis. The 15 µL collected was then centrifuged to separate nanoparticles. The supernatant (10 µL) was then collected for further analysis.

2.4 Wnt-reporter assay

Wnt reporter cells were seeded overnight in 24-well plates at a density of 57,000 cells per well. The following day, cells were treated with Wnt3a for 24 hours. After incubation at 37 °C, cells were detached using 100 µL of trypsin (0.5%) at 37 °C. Fresh DMEM was dispensed into 96-well V-bottom plates, and the trypsinised cells were added to achieve a final volume of 200 µL. Cells were centrifuged at 300 × g for 5 min in a plate spinner, washed once with 3% (w/v) BSA in 1× PBS, the supernatant discarded, and the pellet resuspended in 3% BSA/ PBS prior to flow cytometry analysis. Wnt3a standards (0–100 ng/mL) were used in the described assay to generate a calibration curve

2.4.1 Flow cytometry

Samples were analysed on a flow cytometer (CytoFLEX, Beckman Coulter) at a flow rate of approximately 100 events per second, with each run stopped after ~10,000 events were recorded. Lasers at 405 nm, 488 nm, and 633 nm were operated throughout, with GFP excited primarily at 395 nm and secondarily at 475 nm, producing an emission peak at 509 nm. Data were processed using CytExpert software, and analysis was performed by gating on eGFP-positive live cells. The proportion of GFP-positive cells was expressed as a percentage of the total live population.

2.5 Statistical analysis

In this study, comparisons across multiple groups were conducted using two-way ANOVA. Post-hoc analyses were performed using the Tukey method to assess specific group differences where all the experimental values were pooled. The statistical analysis was conducted using OriginPro software. Significance levels were denoted as follows: * = $p < 0.1$, ** = $p < 0.01$, *** = $p < 0.001$, and **** = $p < 0.0001$. Data sets lacking asterisks indicate non-significant differences.

Chapter 3

3. Optimisation of polymer-coated SPION synthesis and *in vitro* toxicology assessment

3.1 Aims and rationale

The field of nanomedicine holds transformative promise for diagnostics, imaging, and therapeutics, enabling interventions at previously unattainable scales. This capacity directly addresses the limitations of conventional medical approaches, which often struggle with issues such as poor drug solubility, rapid systemic clearance, non-specific biodistribution leading to off-target toxicity, and challenges in achieving therapeutic concentrations at disease sites [118]. Engineered nanomaterials, typically ranging from 1 to 100 nm, offer unique physicochemical properties, including a high surface area-to-volume ratio, tunable morphology, and the ability to encapsulate diverse payloads that can be precisely tailored for specific biological interactions [119]. However, the successful translation of these advanced materials from laboratory to clinic is critically dependent on their biocompatibility [120]. In the context of nanomaterials, biocompatibility signifies not merely the absence of acute toxicity but also the dynamic ability to perform the intended function without eliciting undesirable local or systemic responses over time within the complex biological environment [121]. A thorough understanding of these intricate interactions is paramount because nanoparticles directly interact with cells, proteins, and tissues [120]. Failure to ensure robust biocompatibility can lead to immediate cytotoxicity, chronic inflammation, undesirable immune responses, altered cellular function, or long-term adverse effects, any of which would fundamentally negate their potential therapeutic benefits [121].

Beyond these critical biocompatibility concerns, a significant hurdle in regenerative medicine lies in effectively delivering therapeutic drugs to specific endogenous cells, such as MSCs, at the site of bone injury. This targeted delivery is crucial because, while MSCs are naturally recruited to damaged bone for their regenerative potential, ensuring that therapeutic drugs reach these specific cells with high precision without affecting surrounding healthy cells or being rapidly cleared remains a considerable challenge for enhancing bone regeneration strategies [3, 122]. Therefore, methods of targeting tissue regeneration in a localised manner have become an appealing application [123]. The use of biomaterials in regenerative medicine has emerged as a promising tool. Research in this field has largely focused on producing biocompatible scaffolds designed for implantation at damaged sites. These scaffolds are often highly porous and engineered to sequester and release biomolecules, such as growth factors, to activate MSCs [61, 124, 125]. However, despite their promise as templates for tissue formation, scaffolds face several significant developmental hurdles, including the need for reliable cell adherence, effective immune response evasion, and precise control over therapeutic cargo release, including optimal drug loading and sustained delivery [126].

Given these challenges, the field of regenerative medicine beyond scaffolds, nanoparticles offer a compelling alternative that has been extensively studied in biomaterial applications involving MSCs. A key advantage of nanoparticles is their design capability for triggered molecular release at target sites, which often eliminates the stringent requirement for cell adherence to the biomaterial, a factor that is typically crucial for scaffolds. Among the many types of nanoparticles offering unique advantages, SPIONs have largely been utilised as a tool for cell tracking, notably as an MRI contrast agent [20, 21]. However, bare SPIONs inherently possess high surface energy, rendering them acutely prone to aggregation in physiological solutions [127]. Such aggregation not only diminishes their colloidal stability, but also leads to rapid opsonisation, undesirable coating by plasma proteins, and subsequent accelerated clearance by the reticuloendothelial system (RES), predominantly through phagocytic macrophages in the liver and spleen [128]. Beyond this rapid clearance, the direct interaction of uncoated SPIONs with cellular components can induce oxidative stress and cytotoxicity [129]. Therefore surface modification is a prerequisite for SPIONs [14]. This process fundamentally transforms their surface properties, typically yielding a stable hydrophilic interface that enhances colloidal stability, improves biocompatibility, reduces nonspecific interactions, and prolongs systemic circulation, thereby enabling their safe and effective use in vivo [14, 130, 131].

This stability is critical for minimising protein adsorption and preventing aggregation. While extensive research has focused on various coatings to achieve this, such as dextran [130, 132], polyethylene glycol (PEG) [14], polyethylenimine (PEI) [133], polyxamers [134], and poly(N-isopropylacrylamide) (PNIPAM) [17, 135]. While these have been extensively studied in biomedical science, poly(N-isopropylmethacrylamide) (PNIPMAM) presents an alternative, owing to its structural similarity to PNIPAM and potential for enhanced properties [42]. Since it has a higher LCST which offers appropriate thermal responsiveness for applications at human body temperature.

Despite these attributes, PNIPMAM remains comparatively underexplored in biomedical sciences, with a notable lack of comprehensive toxicity studies for its application, particularly concerning PNIPMAM-coated SPIONs. Therefore, this chapter aims to address this gap by thoroughly investigating the toxicity and biocompatibility of PNIPMAM-coated SPIONs and PNIPMAM. Specifically, the cytotoxic effects were evaluated on the Y201 cell line. Y201 cells are particularly valuable as a model because of their tripotency and accurate representation of MSC characteristics, making them relevant for assessing the safety and in vitro biological interactions of these nanoparticles within a regenerative medicine context [91]. The use of human cells in this study further enhances the relevance and applicability of the findings to human health and therapies.

3.2 Results

3.2.1 Optimising polymer coating on the SPION core

A crucial step in creating functional nanoparticles is coating SPIONs with PNIPMAM. However, this approach presents considerable challenge when the SPIONs are synthesized using methods that result in a hydrophobic surface. This hydrophobicity stems from the oleic acid and oleylamine long-chain hydrocarbons used during SPION synthesis to achieve monodispersity and a controlled particle size [18]. To make the particles water-soluble and suitable for bio-applications requiring triggered protein release, PNIPMAM coating is essential, as this approach successfully renders the nanoparticles water-soluble for use under physiological conditions *in vitro*.

The established protocol for this coating involves functionalizing the PNIPMAM polymer with nitrodopamine (NDA), a chelator that can actively bind to the SPION surface. The NDA-functionalized polymer then undergoes ligand exchange with the oleic acid and oleylamine on the SPION surface, a procedure that involves five hours of sonication in an ultrasonic water bath [18]. This sonication temporarily loosens the interactions between oleic acid and oleylamine and the SPION surface, allowing the NDA-functionalized polymer to attach during temporary detachments.

A successful PNIPMAM coating is typically indicated by two key behaviours: the nanoparticles should be soluble in water without aggregation at temperatures below 45°C and consistently precipitate at elevated temperatures, specifically between 45 and 50°C. Initial attempts to recreate this established protocol proved difficult, as shown by the particles not precipitating within the expected 45-50°C range, even though the coated particles were soluble in water. This lack of precipitation suggested potential issues with the coating process, indicating that PNIPMAM may not have been uniformly or adequately coated onto the SPIONs. Insufficient attachment of the NDA-functionalized polymer to the SPION's surface was hypothesized as the root cause. Efficient polymer attachment is crucial for achieving the high polymer chain density required for temperature-dependent precipitation.

Successful work by R. Sharma utilized a specific Grant MXB14 ultrasonic water bath for this critical sonication step. Following the irreparable damage to this unit, its replacement proved notably less effective even with prolonged sonication. This disparity highlighted variations in specifications among different ultrasonic water baths, which directly impact the efficiency of ligand exchange [18].

To address this, an optimization where various models of ultrasonic water baths were evaluated (as detailed in **Table 3.1**) to identify the most effective model for ligand exchange, thereby enhancing the polymer coating density and ensuring reliable temperature-responsive precipitation of the polymer-coated SPIONs.

Name of the company	Grant MXB14	Fisher Brand FB11203	MXB6	Advantage-Lab AL04-12-230
Tank capacity (L)	14	5.75	6	12.75
Power (W)	RMS 162	180/150	RMS 89	200
Ultrasonic frequency	-	37kHz/80kHz	-	38kHz
Peak (W)	325	880	180	
w/h/d (mm)	325 x 310 x 380	255x115x75	325x310x205	365x321x200

Table 3.1: Specification of the tested ultrasonic water baths

Following coating, Nano Differential Scanning Fluorimetry (Nano-DSF) was used to accurately record precipitation events. While traditionally employed to analyse protein unfolding as a function of temperature via fluorescence detection, Nano-DSF demonstrates versatility by also enabling the recording of light scattering as a function of temperature [27]. This feature is crucial for observing coated nanoparticle aggregation during phase transition: as the completely water-soluble SPIONs aggregate at this point, the change in light scattering is detected and precisely visualized through deviations in its first derivative. This allows for the precise determination of the temperature at which particle precipitation occurs, a pivotal parameter for assessing coating efficiency.

The analysis of Nano-DSF data revealed discrepancies in the precipitation onset temperature among different concentrations of coated SPIONs. Notably, not all concentrations exhibited precipitation within the target range of 45–50 °C, indicating inconsistencies in coating quality and efficiency. These variations are likely attributable to incomplete ligand exchange during the coating process, which can leave nanoparticles unstable and prone to irreversible aggregation upon heating. The onset of this aggregation can vary from batch to batch, depending on the degree of ligand exchange achieved. Importantly, such aggregation produces a Nano-DSF signal that mimics a phase transition, which could lead to misinterpretation of the results. The arrows in **Figure 3.1** indicate the temperatures at which precipitation occurred, highlighting the differences within each coating batch at various concentrations.

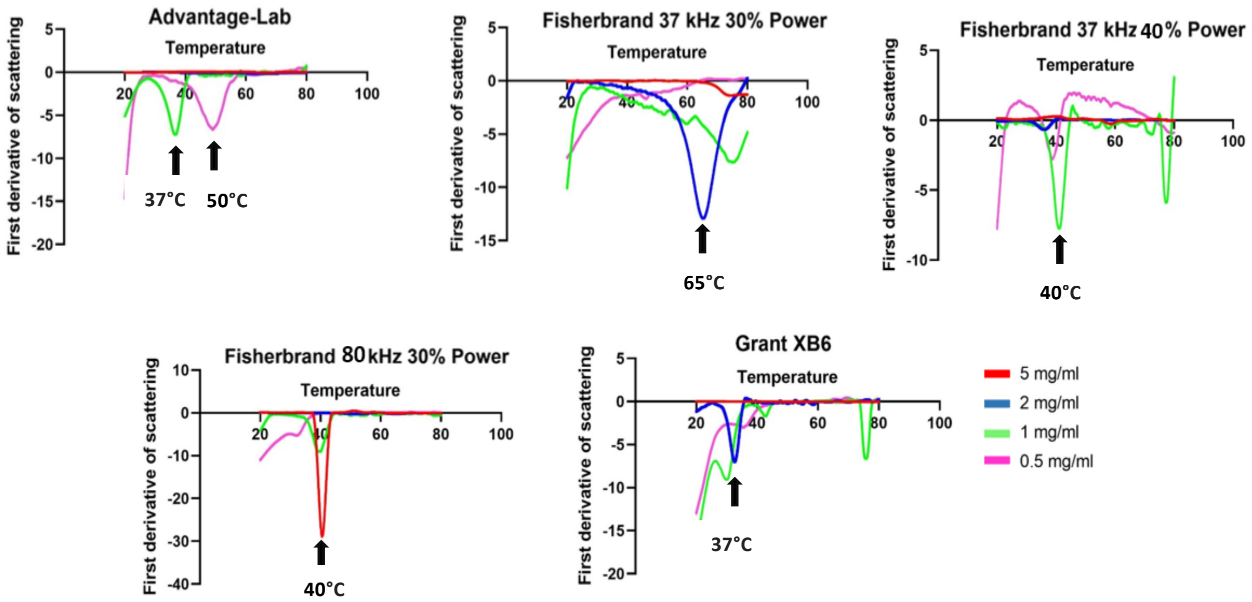

Figure 3.1: Ligand exchange efficiency promoted by different bath sonicators: The plots show the first derivative of the light scattering thermograms of coated SPIONs determined via nano-DSF at the indicated concentrations. Measurements were conducted on samples prepared using the indicated ultrasonic water bath and settings.

Achieving a uniform polymer coating is essential for obtaining PNIPMAM-Coated SPIONs both water-soluble and thermally sensitive. Despite the use of various ultrasonic water baths, a significant issue was that the obtained coated nanoparticles did not consistently precipitate at 45-50 °C. This observation prompted a comprehensive investigation into potential causes beyond the use of different ultrasonic water baths. Despite becoming water-soluble post-coating, the nanoparticles failed to exhibit the expected precipitation behaviour, suggesting that the NDA-NIPMAM polymer coating may not have been uniformly distributed around the SPIONs.

Further examination revealed that nitrodopamine (NDA), which is used in the synthesis to functionalize the PNIPMAM polymer, might have contributed to the improper coating. While free or unfunctionalized NDA is removed by dialysis this purification process may have been inefficient, leaving some unreacted NDA in the polymer solution. NDA has an iron-chelating property. NDA is also partially soluble in water. the presence of excess free NDA could cause it to independently bind to the iron oxide surface, thereby preventing the NDA-PNIPMAM polymer from binding correctly. This results in a non-uniform coating, which explains why the SPIONs precipitated at temperatures significantly different from 45–50°C, even within the same synthesis batch. To address this, we went back to the NDA-PNIPMAM synthesis and implemented an improved purification procedure.

To address this problem, we first extended the dialysis process in distilled water to enhance the removal of free NDA from the solution. However, extended dialysis alone proved insufficient for removing excess free NDA, as the polymer-coated SPIONs still did not precipitate above 45°C. Recognizing that NDA is partially soluble in water, we refined our approach. After dialysis of the NDA-functionalized polymer in distilled water, the dialysed solution was centrifuged at 21,000 × g for 10 min. This step was designed to effectively remove any remaining unbound and potentially aggregated NDA molecules which were not soluble in water (**Figure 3.1**).

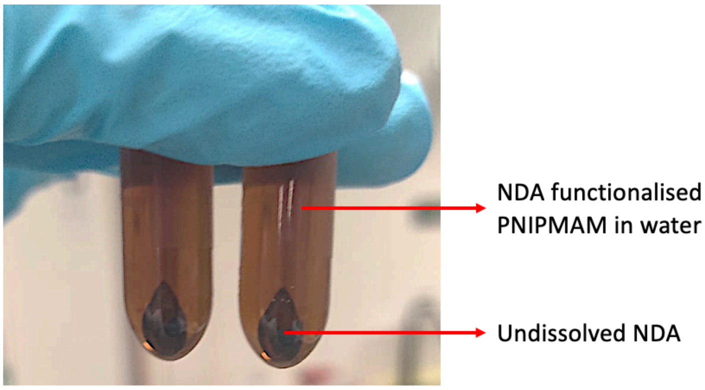

Figure 3.2: Removal of undissolved NDA: Purification of NDA-functionalized PNIPMAM solution by centrifugation.

The introduction of centrifugation after the dialysis process represented a significant improvement in coating methodology. This centrifugation facilitated the separation of insoluble NDA, ensuring that only NDA-functionalized polymer remained in the solution. This refinement in NDA-PNIPMAM preparation significantly enhanced the efficiency of ligand exchange, which is essential for successful coating. By ensuring that the NDA-functionalized polymer was the primary substance interacting with the SPIONs, a uniform and effective polymer coating was achieved. This success was directly evidenced by the Nano-DSF analysis, which consistently showed a sharp phase transition/precipitation at above 44°C, confirming the expected thermal responsiveness of the PNIPMAM coating on to SPIONs(**Figure 3.3**). For the subsequent coating, an 'Advantage-Lab AL04-12-230' ultrasonic water bath was used. This particular unit was chosen not only for its ready availability but also because the preceding optimization study revealed no systematic differences in coating efficiency among the various ultrasonic water bath models evaluated.

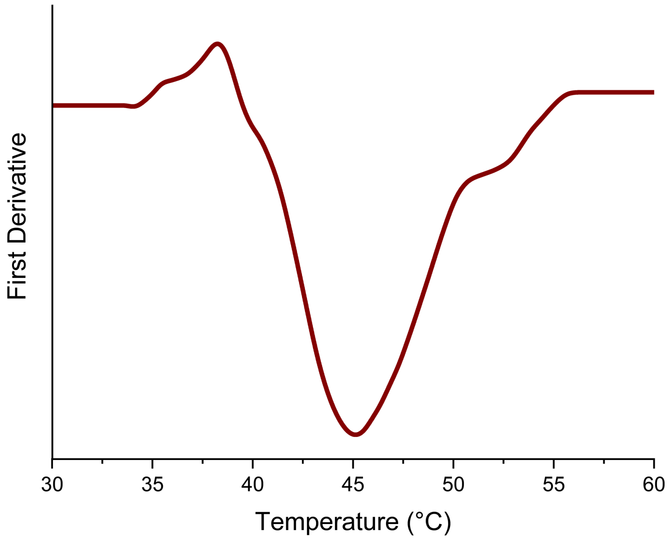

Figure 3.3: Thermal responsiveness of coated SPIONs following improved NDA removal: nano-DSF plot showing of 10 mg/ml of PNIPMAM-coated SPIONs prepared following improved NDA removal using high-speed centrifugation.

Thermal responsiveness and reversible precipitation of nanoparticles.

Further visual observation of precipitation at different temperatures. (**Table 3.2**, **Figure 3.4**) indicated that the nanoparticles did not precipitate at temperatures below 44°C but underwent a distinct phase transition and consistently precipitated at temperatures above 44°C. This finding is significant as it demonstrates that the behaviour of the nanoparticles can be controlled more accurately with the improved coating process. Importantly, this precipitation process was found to be reversible, as the temperature decreased below 44 °C, the nanoparticles reverted to being completely soluble in water. This reversibility is crucial for biomedical applications, where precise control over nanoparticle behaviour is essential.

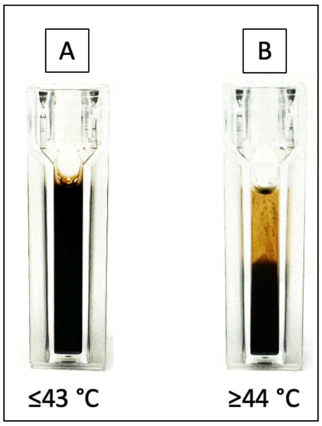

Figure 3.4: Visual representation of nanoparticles precipitation: Phase transition analysis of 5 mg/mL PNIPMAM-coated nanoparticles following heating at the displayed temperatures.

Temperature	42°C		43°C		44°C		45°C	
Time (Minutes)	5	10	5	10	5	10	5	10
Polymer coated SPIONs	X	X	X	X	✓	✓	✓	✓

Table 3.2: Monitor the stability of the coated SPIONs at various temperature: 200 µL of a 10 mg/mL solution was added to a 500 µL microcentrifuge tube and placed in a heat block. At each designated time point, the tube was inverted and checked for nanoparticle precipitation. "X" indicate no precipitation, and "✓" indicates precipitation.

3.2.2 Thermogravimetric analysis (TGA) of polymer coated SPIONs

To further validate the ligand exchange process, TGA was employed to assess the amount of polymer in the polymer-coated SPIONs. Coated SPIONs were exposed to a controlled temperature program in a controlled atmosphere while monitoring their weight change as a function of the temperature. The results revealed a 36% mass loss recorded above 300°C (**Figure 3.5**), the temperature range where organic material is decomposed when subjected to heating, confirming the presence of 36% (w/w) polymer on coated nanoparticles. The gradual weight loss observed as the polymer component decomposed upon heating further supports this presence.

In conjunction with TGA, Transmission Electron Microscopy (TEM) was used to measure the size and morphology of the SPIONs. The grafting density of the polymer on the SPION surface was calculated by combining the TEM data, which revealed that the SPIONs were approximately 14 nm in diameter, with the TGA results. The grafting density was approximately 0.07 chains/nm². This grafting density represents a significant improvement, as previous studies on nanoparticles ranging from 11 nm to 16 nm reported polymer mass losses of only 15-18%, which is considerably less than the mass loss achieved in this study. This enhanced polymer coating was attributed to the addition of a specific step in the synthesis protocol. This comprehensive analysis, encompassing both the substantial polymer mass fraction demonstrated by TGA and the calculated grafting density, this confirms the successful implementation of the modified ligand-exchange process for enhanced polymer coating on the SPIONs.

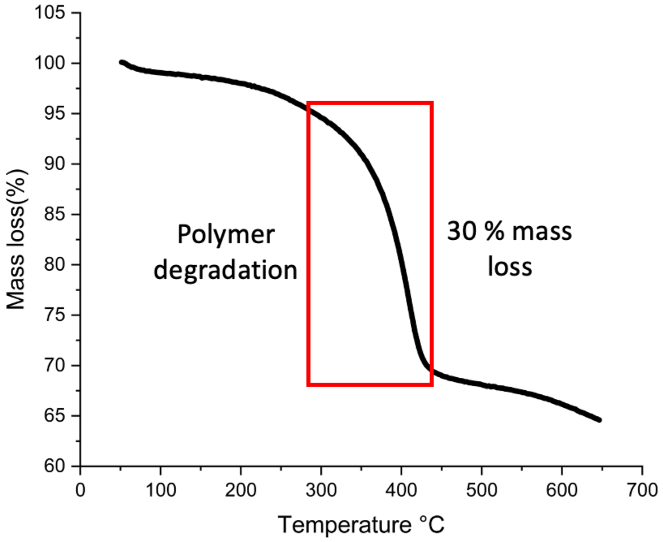

Figure 3.5: TGA of polymer-coated SPIONS: 10 mg of dry PNIPMAM-coated SPIONs samples heated under air at a ramp rate of 5°C /min between 0-600°C.

3.2.3 Investigating the physiological effects of polymer-coated SPIONs on MSCs

To establish whether the coated SPIONs would be usable as a therapeutic delivery vehicle, a comprehensive assessment of their physiological effects on the Y201 cell line was performed. For this, cells were seeded at a low density, and their metabolic activity was was monitored over a three-day period after treatment and taken to consideration as viability with respect to the untreated control conditions, as detailed in the following section, utilizing rezasurin dye r assays with fluorescence readings correlated to cell number. Additionally, the effects of polymer-coated SPIONs on cell differentiation was also measured.

3.2.3.1 Assessing the toxicity of polymer NIPMAM.

To assess the toxicity of PNIPMAM and NDA-PNIPMAM, a series of toxicity tests were conducted using Y201 cell lines. This experiment is particularly noteworthy as it represents the first known assessment of the effects of these polymers on cellular proliferation, providing new insights into their potential applications in the biomedical field. To plan these experiments, the TGA results were used (**Figure 3.5**), which showed that 36% of the total mass of the polymer-coated SPIONs was the polymer. Thus, it was inferred that 1 mg of coated SPIONs contained 0.36 mg polymer. To thoroughly investigate the polymer's inherent toxicity across a relevant range, and to encompass the polymer content at the initial target SPION concentration (0.36 mg/ml), polymer concentrations from 0.2 to 0.8 mg/ml were tested. This range was also selected to provide a broader safety profile for the polymer

To evaluate the cytotoxic effects, different polymer concentrations were tested. The proliferation rates of MSCs were assessed in the presence of PNIPMAM and NDA-functionalized PNIPMAM (**Figure 3.6**). Data from toxicity tests on Y201 cell lines showed consistent metabolic activity readout proportional to the cell number across all tested polymer concentrations (0.2–0.8 mg/ml) on day 1 and 2. With slight reduction in metabolic activity observed on day 3 at the highest polymer concentration. l Toxicity assays revealed no significant differences between the untreated and treatment groups at lower polymer concentrations, conclusively demonstrating PNIPMAM and NDA-functionalized PNIPMAM both soluble at the temperatures used for toxicity studies did not inhibited MSC proliferation. This successful demonstration that these polymers are not of toxic provides a solid foundation into their use in various medical applications.

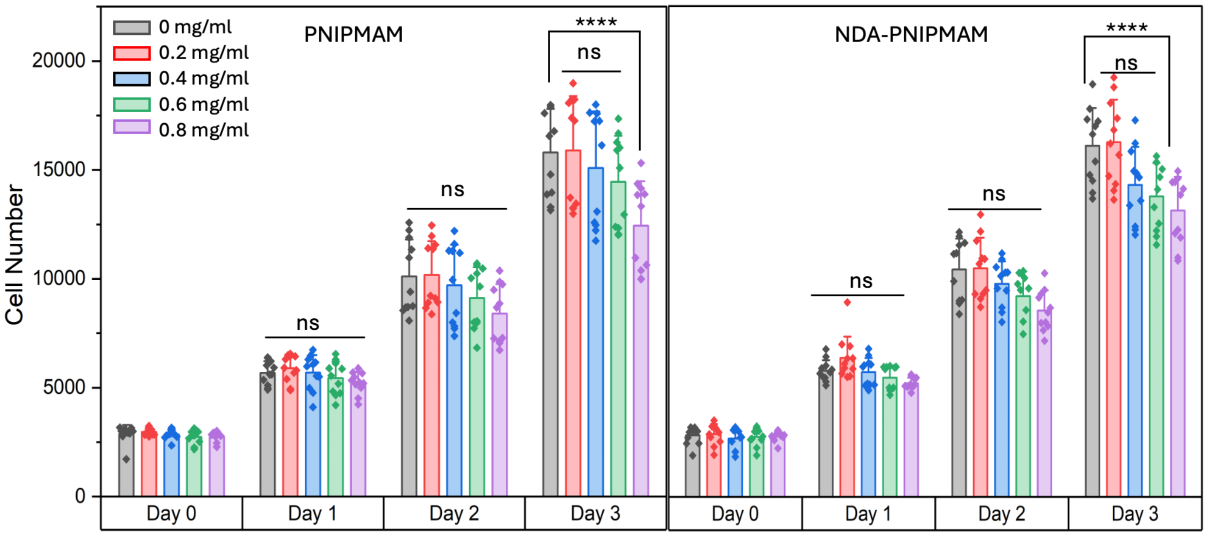

Figure 3.6: Effect of PNIPMAM (A) and NDA-PNIPMAM (B) on Y201 cells:

The fluorescence intensity is presented as a readout to metabolic activity which is proportional to the cell number. (N=2) are presented as mean ± SE. Statistical significance (****, P<0.0001) was determined using Two-way ANOVA with Tukey's post hoc test.

3.2.3.2 Comparing Toxicity of Polymer-Coated and Citric Acid-Coated SPIONs with Focus on Short-Term and Long-Term Exposure

A comparative toxicity assay was designed to investigate the potential biological effects of polymer-coated SPIONs and to precisely identify whether any observed impact stemmed from the SPION core or the polymer coating. Citric acid-coated SPIONs (synthesized by Rajat Sharma) served as a critical control to isolate the effects of the bare nanoparticle. These particles were of the same size and citric acid was used as a coating agent instead of PNIPMAM. Citrate coated particles do not show phase transition but are soluble in water and were stable over the experiment duration. A concentration of 5 mg/ml was used for these assays, as established protocols for protein encapsulation were at this specific concentration [18].

The results revealed a notable difference in cell metabolic activity rate between the two nanoparticle-coated groups(**Figure 3.7**A). Specifically, cells exposed to polymer-coated SPIONs exhibited significantly showed lower metabolic activity than those exposed to citric acid-coated SPIONs. Furthermore, the citric acid-coated SPIONs showed reduced cell metabolic activity compared to the control group, which was not exposed to any nanoparticles. The decrease in cell metabolic activity observed with citric acid-coated SPIONs indicates that the SPION core has an inherent level of toxicity at a concentration of

5 mg/ml. However, this is significantly aggravated by the polymer coating. In parallel with other assessments, an experiment was conducted to evaluate the short-term toxicity of polymer-coated SPIONs on Y201 cells, hypothesizing that brief exposure durations might mitigate adverse effects relevant to *in vivo* treatment scenarios. Cells were treated for an hour at concentrations of 5 mg/ml and 2 mg/ml to assess their short-term toxicity. The results indicated that even after an hour, both the 5 mg/ml and 2 mg/ml concentrations exhibited some toxicity but it is vastly reduced compared to the longer incubation. The short-term exposure experiment demonstrated that the toxic effects of the polymer coating manifested quickly, within an hour of exposure. The polymer coating, while intended to provide biocompatibility and functionalisation, might have contributed to the observed toxicity at concentrations of 2 mg/ml and 5 mg/ml.

Moving forward, lower concentrations of polymer-coated SPIONs were explored as the current concentration was causing toxicity.

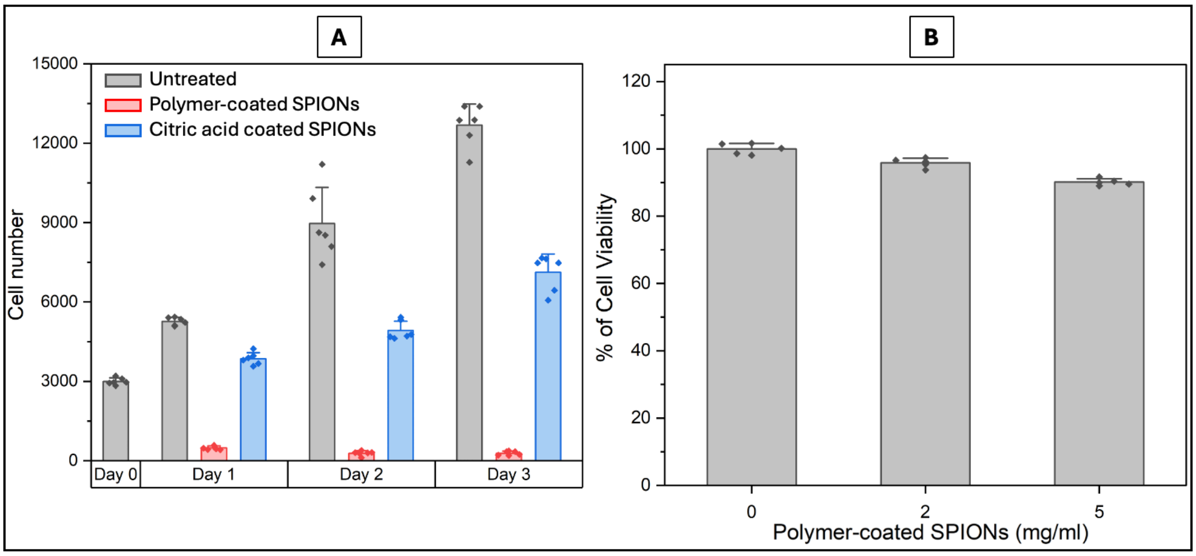

Figure 3.7: Comparative cytotoxicity and proliferation effects of polymer-coated SPIONs on Y201 cell line: (A) Cells were exposed to coated and citric acid-coated SPIONs (5 mg/ml) for 1, 2, and 3 days; fluorescence intensity was normalised to cell number using a standard curve. (B) Y201 cells were treated with polymer-coated SPIONs; fluorescence intensity represents the percentage of A) cell number B)% cell viability, 0 mg/ml consisted of medium only, without nanoparticles.

3.2.3.3 Evaluating the toxicity of polymer-coated SPIONs at lower concentrations

Building upon previous toxicity assessments, we next aimed to refine the understanding of polymer-coated SPIONs' impact on cell proliferation at lower concentrations. The goal was to determine the specific threshold where polymer-coated SPIONs no longer exerted adverse effects on cellular proliferation. Concentrations ranging from 2 mg/ml down to 0.25 mg/ml were systematically evaluated through twofold dilution steps. Figure 3.8 highlights a significant decrease in cell metabolic activity at 2 mg/ml, as expected from the results above (Figure 3.7B), indicating a notable decrease effect compared to the control. The polymer-coated SPIONs demonstrated less toxicity compared to the previously tested 5 mg/ml concentration and did not significantly affect cell growth at concentrations below 2 mg/ml. This is evidenced by the robust maintenance of cellular proliferation and metabolic activity dynamics within the control range, affirming that these nanoparticles allow cells to grow and function optimally, completely unaffected by exposure to polymer coated SPIONs at concentrations of 1 mg/ml and below.

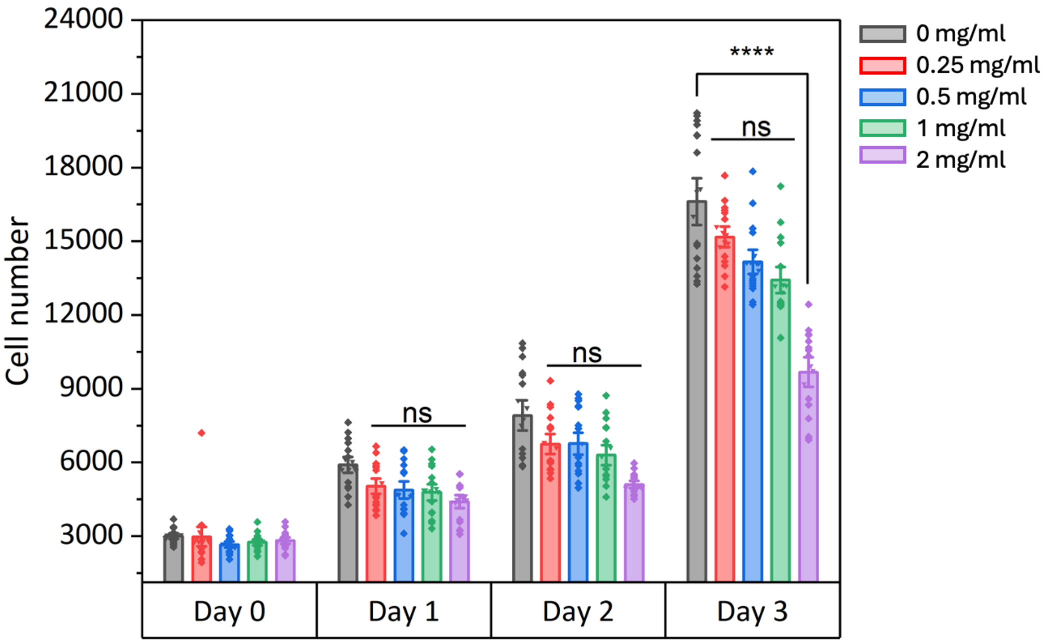

Figure 3.8: Effect of polymer-coated SPIONs on Y201 cell proliferation: The fluorescence intensity was normalised to the cell number and measured using a standard curve. (n=3) are presented as mean ± SE. Statistical significance (****, P<0.0001) was determined using Two-way ANOVA with Tukey's post hoc test.

3.2.3.4 Evaluation of influence of polymer-coated SPIONs on osteogenic differentiation potential.

After establishing that polymer-coated SPIONs were not toxic to Y201 MSCs at 1 mg/ml and below, their influence on the osteogenic differentiation of Y201 cells was investigated. This specific evaluation of the polymer-coated SPIONs without osteo-inducive proteins (BMP2 and Wnt3a) was performed to establish a crucial baseline reading, facilitating the detection of potential leakage or non-specific effects in future experiments involving encapsulated osteoinducive proteins. The assessment involved measuring the production of p-nitrophenol (pNP), a direct product of the alkaline phosphatase (ALP) reaction, over 9 days at various concentrations of polymer-coated SPIONs. The amount of pNP produced is directly proportional to ALP activity, a key marker of osteogenic differentiation.

For this purpose, Osteogenic differentiation medium (ODM) served as a positive control for differentiation, while the 0 mg/ml (untreated) group represented basal medium without polymer-coated SPIONs. All tested concentrations of polymer-coated SPIONs (0.25-1 mg/ml) consistently maintained low p-NP levels throughout the 9-day period, comparable to the untreated control (0 mg/ml) (**Figure 3.9**). While minor fluctuations were observed, sometimes showing a slight decrease around day 9 compared to day 6, this could be likely be attributed to the inherent assay noise common in *in vitro* measurements in the presence of polymer-coated SPIONs or potential interference from residual nanoparticles affecting the readings. Nevertheless, these findings clearly indicate that polymer-coated SPIONs alone do not induce osteogenic differentiation at the tested concentrations and time points. This data establishes a crucial baseline for future experiments involving the encapsulation of osteoinducive proteins, such as Wnt3a and BMP2, into polymer-coated SPIONs.

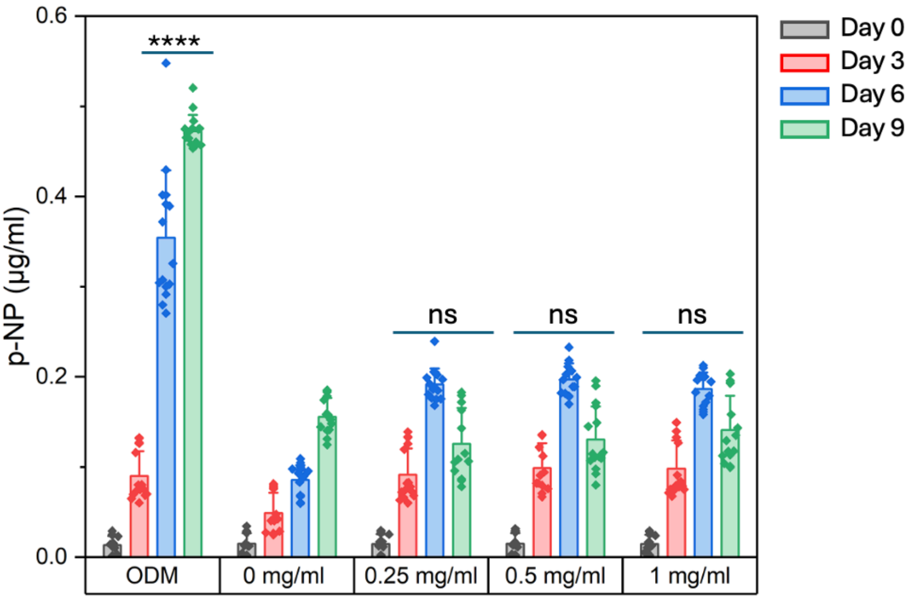

Figure 3.9: Osteogenic differentiation in Y201 cells treated with coated SPIONs: p-NP

measured over 9 days in the presence of varying polymer-coated SPION concentrations. (n=3) mean ± SE. Statistical significance (****, P<0.0001) was determined using Two-way ANOVA with Tukey's post hoc test.

3.3 Conclusion

This chapter has established an optimised approach for synthesising NDA-functionalised PNIPMAM-coated SPIONs and provided the first evaluation of their biocompatibility. Refinement of the coating process, particularly through the inclusion of a centrifugation step after dialysis, ensured a consistent and reliable polymer coating, as confirmed by nano-DSF and TGA which is also used by several studies to confirm the coating process [17, 18, 136, 137]. which together provided evidence of the coating's consistency and integrity. This methodological improvement represent an important advancement, ensuring that the nanoparticle system can be reliably reproduced.

Following successful optimisation of the synthesis, toxicity studies of both the polymer and the polymer-coated SPIONs were conducted. These revealed that while the polymer itself is biocompatible, the coated nanoparticles exhibit concentration-dependent effects on MSCs, with adverse outcomes becoming apparent at 2 mg/ml. Importantly, concentrations at and below 1 mg/ml were well tolerated. Approved by several studies which shows at toxicity at much lower concentrations compared what we have tested [129, 138].

The absence of osteogenic differentiation in MSCs exposed to polymer-coated SPIONs at concentrations up to 1 mg/ml indicates that the nanoparticles themselves are biologically inert with respect to osteogenesis. This is an important observation, as it confirms that any future induction of osteogenic differentiation in the presence of these nanoparticles will be attributable to the encapsulated proteins (e.g., BMP2 or Wnt3a). These nanoparticles act as a neutral carrier within the tested concentration range, providing a controlled baseline against which the true biological effects of loaded proteins can be evaluated.

This chapter provides valuable insights into the development and biological interactions of PNIPAM-coated SPIONs. While demonstrating promising biocompatibility at 1 mg/ml and below. Moving forward, the concentration decision depends on the release profile of BMP2/Wnt3a from the polymer-coated SPIONs and on determining the requisite amount of these growth factors for optimal MSC differentiation.

While the nanoparticles safety and functionality have been confirmed in a basic cellular environment, their ultimate purpose is to evaluate the capability of the polymer-coated SPIONs to deliver bioactive molecules. Consequently, the subsequent chapter will investigate the system’s ability to encapsulate and release a key osteogenic growth factor, bone morphogenetic protein-2 (BMP2).

Chapter 4

4. Encapsulation and release of BMP2

4.1 Aims and rationale

Bone morphogenetic protein 2 (BMP2), a pivotal member of the transforming growth factor-beta (TGF-β) superfamily, is a glycosylated dimeric protein that orchestrates a diverse array of crucial biological processes most notably bone formation [59]. Its potent bioactivity stems from its ability to promote osteoblast differentiation from mesenchymal stem cells (MSCs) through its interaction with heteromeric complexes of specific BMP type I and type II serine/threonine kinase receptors (e.g., BMPRIA and BMPRII), thereby initiating intracellular signalling cascades that ultimately dictate cellular fate and function [139, 140] (**Figure 4.1**). This triggers phosphorylation and activation of SMAD1/5/8. Subsequently, SMAD4 binds, forming a complex that moves to the nucleus and activates runt-related transcription factor-2 (Runx2) and osterix (Osx). These transcription factors induce the expression of osteogenic genes, such as alkaline phosphatase (ALP), type I collagen, and osteocalcin, which are crucial for bone formation [65, 75].

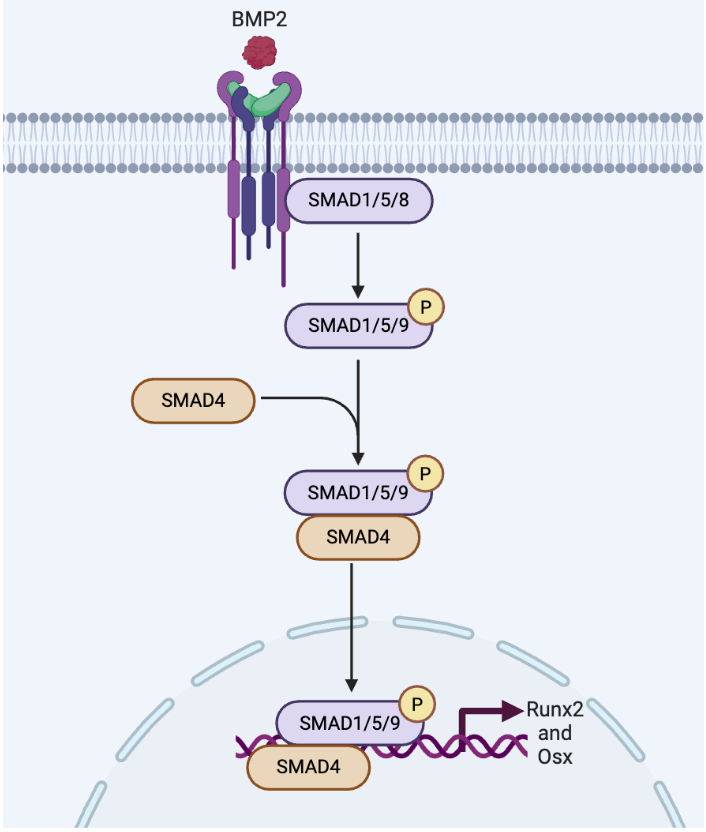

Figure 4.1: BMP2 canonical signalling pathway: BMP-2 binds to Type I and Type II serine/threonine kinase receptor, leading to phosphorylation and activation of SMAD1/5/8. Therefore, SMAD4 can bind to SMAD1/5/9 to form a complex. This complex moves to the nucleus and binds to a specific SMAD binding element. This stimulates the expression of osteogenic genes,such as RUNX2 and Osx. (Created with BioRender.com)

The potent osteogenic differentiation capabilities of BMP2 have positioned it as a cornerstone in regenerative medicine, with applications ranging from spinal fusion to fracture healing and dental implants [125, 141]. However, the clinical use of BMP2 is hindered by challenges such as broad biological activity affecting multiple cell types, potential for systemic diffusion and induction of ectopic bone formation, susceptibility to degradation, and the requirement for high doses at physiological levels, which can lead to adverse effects. [76, 79, 142, 143].

Understanding the intricate interplay between BMP2 and its receptors is fundamental to harnessing its therapeutic potential for bone regeneration. The expression patterns of BMP2 receptors comprising both Type I and Type II receptors these receptors presence are highly cell type and developmental stage specific, fine tuning cellular responsiveness and enabling BMP2’s pleiotropic effects [144]. The specific complement and relative abundance of these receptors critically influence cellular outcomes, including osteogenesis and chondrogenesis [63, 77, 145]. Consistent with BMP2's crucial role in skeletal development and repair, these receptors are highly expressed in cells of the mesenchymal lineage [59, 145]. However, a significant challenge lies in the inherent heterogeneity of primary human MSC populations, which can lead to variability in receptor expression and responsiveness to BMP2. This variability in receptor expression and signalling capacity often results in less predictable and sometimes lower average responses to BMP2 in certain human MSCs [146, 147]. Furthermore, BMP2 receptors are also present in other cell types, including endothelial cells [148], epithelial cells (in the heart) [149], and certain neuronal populations [141]. reflecting BMP2's diverse roles in development and homeostasis. These inherent limitations and off-target effects underscore the need for innovative strategies. Therefore, to effectively leverage BMP2's therapeutic potential by ensuring controlled delivery and minimising off-target effects, advanced delivery systems are required to safeguard BMP2, regulate its release, and target specific tissues.

In this chapter, PNIPMAM-coated SPIONs were developed as a protein delivery platform, with BMP2 as the primary therapeutic candidate. The polymer coating serves a dual purpose: it protects BMP2 from premature degradation and facilitates controlled and sustained release, making it a promising candidate for therapeutic applications [46]. The polymer-coated SPIONs employed in this study exhibit a lower critical solution temperature (LCST) of 45 °C. This temperature threshold is advantageous for potential in vivo applications because it exceeds the physiological temperature of the human body, thereby minimising premature drug release. Consequently, an assessment of the release profile at 37 °C is crucial for characterising the system's behaviour under conditions relevant to physiological applications. Below the LCST, the polymer coating is expected to maintain a hydrated state, thereby preventing and uncontrolled drug release. Upon entering a biological environment, nanoparticles, such as SPIONs, are rapidly coated by a complex layer of biomolecules, forming a 'protein corona' that can significantly impact their behaviour and drug release kinetics [150]. Previous studies have demonstrated that the release of encapsulated proteins requires the presence of competitor proteins that simulate the protein-rich environment of serum *in vitro* [17]. Furthermore, various nanoparticle-based delivery systems have been explored for the triggered release of therapeutic proteins. For instance, temperature-sensitive nanoparticles, similar to the PNIPAM system used here, have shown promise for controlled release upon localised heating through an external magnetic field [17], and pH-responsive nanoparticles have been designed to release their cargo in specific microenvironments [16]. Another study utilising this delivery system demonstrated a comparatively higher protein release at 45 °C than at 37 °C for encapsulated apotransferrin, GFP, and IgG, as determined by western blot analysis [18]. However, these studies did not evaluate the bioactivity of the released protein at 45 °C. Given the therapeutic significance of BMP2 and the absence of prior evaluations of its bioactive release from this specific delivery system, this chapter aims to investigate the release of BMP2 at both 37 °C and 45 °C in the presence of various competitor proteins and to assess its bioactivity under these conditions.

4.2 Results

4.2.1 Silver staining analysis of BMP2 glycoform stability under simulated encapsulation conditions

To evaluate BMP2's compatibility with our delivery system, both glycosylated and non-glycosylated forms were investigated. BMP2 is commercially available in two glycoforms: a standard non-glycosylated recombinant protein and a glycosylated variant. Glycosylation, a common post-translational modification, can significantly influence a protein's stability, solubility, and bioactivity[74, 151]. Despite these differences, many studies do not clearly specify which form is used in BMP2 delivery systems. By examining both variants, we aimed to determine which form better withstands the encapsulation and release processes.

To assess the thermal stability of glycosylated and non-glycosylated BMP2 in the encapsulation buffer without polymer-coated SPIONs, the samples were incubated at 45 °C for 10 min, mimicking the encapsulation conditions described in the Methods section. Additionally, samples were incubated overnight at room temperature (RT) to evaluate stability using silver staining analysis of these samples, comparing non-glycosylated and glycosylated BMP2.

The first three lanes in each part of the silver-stained gel (non-glycosylated and glycosylated) represent 100, 50, and 25 ng of pure BMP2, which did not undergo any temperature treatment. These lanes served as a control to demonstrate the intact protein and allow for comparison with samples that underwent thermal stress. All other lanes, including those representing temperature-treated samples and the 'UL' (Unloaded) and

'W3' (Wash 3) fractions, were loaded with 100 ng of protein. This 100 ng amount was equivalent to the protein expected in 10 µL of a 100 µL sample, thereby simulating the concentration during encapsulation. The 'UL' and 'W3' fractions specifically indicate samples collected at different incubation time points during the washing steps. Each of the remaining lanes, including those for the temperature-treated samples and UL and W3 fractions, was loaded with 100 ng of protein, equivalent to the amount expected in 10 µL of a 100 µL sample, simulating the concentration during encapsulation. It is crucial to note that this experiment was conducted without nanoparticles. This setup was designed to simulate the thermal stress experienced by proteins during nanoparticle encapsulation (**Figure 4.2**). Both non-glycosylated and glycosylated BMP2 exhibited bands at the expected molecular weight, indicating the presence of the protein. However, the intensity of the bands varied between the two glycoforms. Notably, even without a centrifugation step performed during the washes, non-glycosylated BMP2 showed a decrease in intensity after temperature stress (**Figure 4.2**), indicating that proteolysis likely contributes to its instability alongside direct temperature effects. In contrast, glycosylated BMP2 showed a consistent band intensity after the temperature regime, closely matching that of the untreated control. This suggests greater stability than the non-glycosylated form and indicates that glycosylation enhances the stability of BMP2 under the tested temperature and incubation conditions.

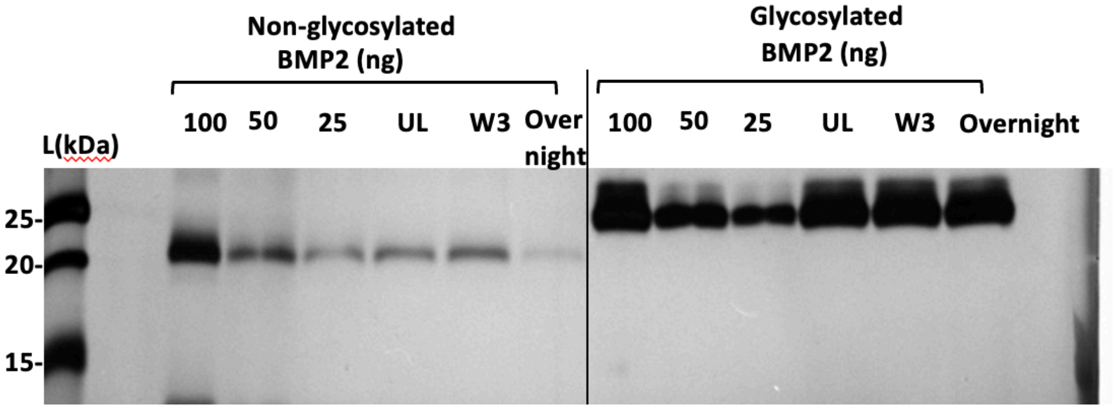

Figure 4.2: Testing the temperature regime without nanoparticles of glycosylated and non-glycosylated BMP2 using silver staining: Comparison of samples heated at 45 °C for 10 min and incubated overnight at room temperature. Lanes show BMP2 standards (100, 50, and 25 ng), unloaded (UL), wash 3 (W3), and overnight incubation. "L" represents the protein ladder.

4.2.2 Using Y201 for measuring BMP2 bioactivity

Human MSCs exhibit significant heterogeneity in terms of surface markers, differentiation potential, and functional properties [90]. Studies using human MSCs isolated from patients have indicated that a high proportion of samples do not display the expected osteogenic response to BMP2 in cell culture. This lack of responsiveness, observed in a diverse set of human MSCs, may be attributed to the inherent variability within the MSC population [92, 152, 153]. The Y201 cell line was selected for this study because it demonstrates tripotency, enabling differentiation into multiple cell lineages [91]. As a homogeneous MSC subtype, the Y201 cell line offers enhanced experimental reproducibility while maintaining MSC characteristics, which is a distinct advantage over heterogeneous primary populations. Although Y201 is an established model, its responsiveness to BMP2 induced osteogenesis has not been previously characterised. This study aimed to determine whether the Y201 cell line could serve as a reliable model for BMP2-driven differentiation, particularly in its ability to respond to BMP2 signalling. The primary objective of this validation was to establish a quantitative framework for assessing BMP2 encapsulation efficiency and the amount of BMP2 released from the polymer-coated SPIONs. To achieve this, we required markers that reflect both the immediate activation of the canonical BMP2 signalling pathway (pSMAD1/5/9) and an early indicator of long-term differentiation (ALP activity). Should these responses yield a consistent correlation between BMP2 concentration and cellular activity, a standard curve could be generated, enabling the precise quantification of bioactive BMP2. The aim is to quantify bioactive BMP2, as only the biologically active form contributes to therapeutic efficacy. By establishing a correlation between BMP2-induced cellular responses and known BMP2 concentrations, a standard curve can be generated. This allows for the accurate assessment of the amount of bioactive BMP2 released from or retained in the delivery system, which is essential for evaluating its performance.

4.2.2.1 Evaluation of time points and concentrations for pSmad detection in response to BMP2 in human MSC

To evaluate the bioactivity of BMP2 released from polymer-coated SPIONs, the Y201 cell line was treated with BMP2. This approach was employed to assess the immediate downstream activation of the Smad1/5/9 signalling pathway, specifically the phosphorylation of Smad1/5/9 (pSmad1/5/9), which is a canonical response to BMP2. While studies have demonstrated peak pSmad activation approximately 30 min post-stimulation in human foetal osteoblast cell lines (hFOBs) [154], the temporal and dose-dependent responses in the Y201 cell line remain uncharacterised. Therefore, a series of experiments was conducted to determine the optimal parameters for BMP2-induced Smad1/5/9 activation in this cell line model. Y201 cells were exposed to BMP2 at concentrations of 5-135 ng/mL and harvested 15-120 minutes post-treatment. These time points and concentrations were chosen to comprehensively assess the dynamic range of BMP2-mediated signalling in Y201 cells.

Western blot analysis revealed a time-dependent increase in pSmad1/5/9 in Y201 cells treated with BMP2, with peak activation observed 30 min post-stimulation (**Figure 4.3**). pSmad levels were indistinguishable from basal levels at 15 min, and activation decreased at later time points (90 and 120 min). Tubulin served as a loading control to confirm consistent protein loading across samples. Notably, treatment with the 4mM HCl control alone did not elicit pSmad activation, which was crucial because lyophilised BMP2 was dissolved in 4mM HCl. This result confirmed that the observed pSmad was specifically induced by BMP2. Furthermore, the "Control" lane, where medium without BMP2 was added, also showed no Smad activation. These results collectively demonstrate a clear temporal response of the Smad signalling pathway to BMP2 in Y201 cells, with 30 min as the optimal time point for assessing BMP2-mediated pSmad at a BMP2 concentration of 5 ng/ml, a trend observed across all tested concentrations (**Figure 4.3**).

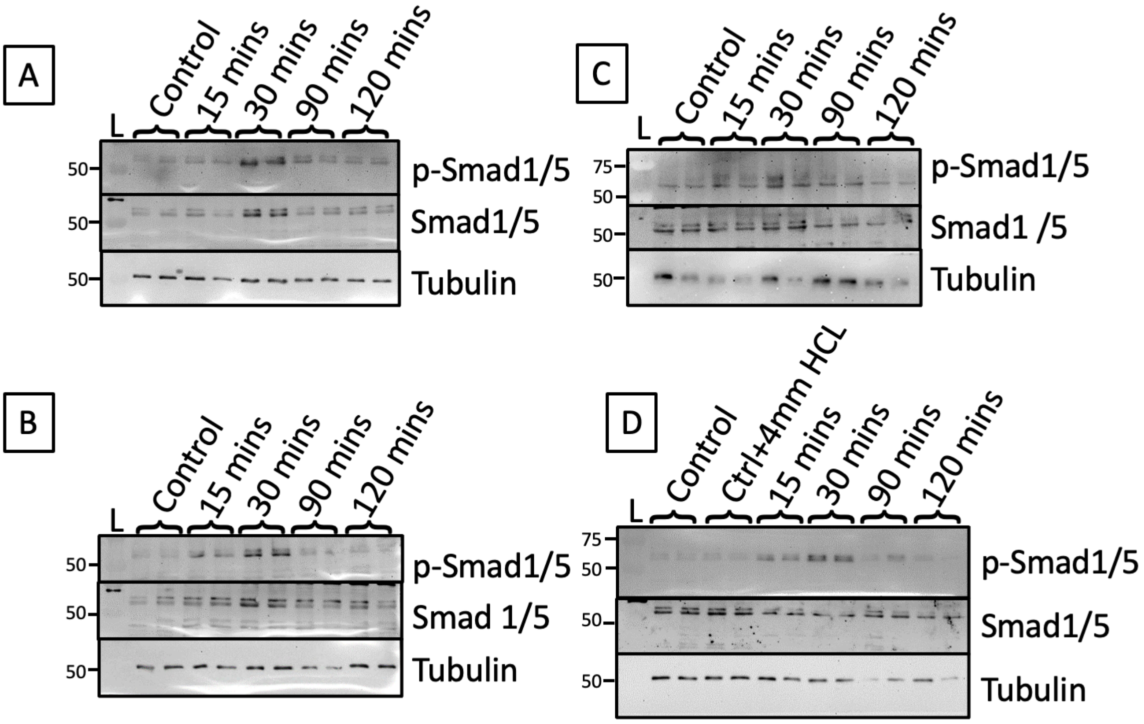

Figure 4.3: Time-dependent pSmad activation in Y201 cell line induced with BMP2: Y201 cell cultures were stimulated with (A) 5 ng/ml, (B) 15 ng/ml, (C) 45 ng/ml, and (D) 135 ng/ml of BMP2 and harvested post-treatment. Western blot analysis shows the levels of pSmad1/5/9, total Smad1/5, and tubulin (loading control)

4.2.2.2 Establishment of a pSMAD1/5/9 standard curve for bioactive BMP2 quantification

Based on initial experiments, 30 min post-BMP2 stimulation was identified as the best time point for observing pSmad1/5/9 activation Compared to 15 min and 90 min timepoints (section 1.2.3) in Y201 cells. To further refine this parameter, a time-course analysis was conducted to examine pSmad1/5/9 activation following treatment with 15 ng/mL BMP2 for 20, 30, 40, and 50 min. This analysis, when quantified, revealed 40 min as the optimal time point for maximal pSmad1/5/9 signal (Figure 4.4).

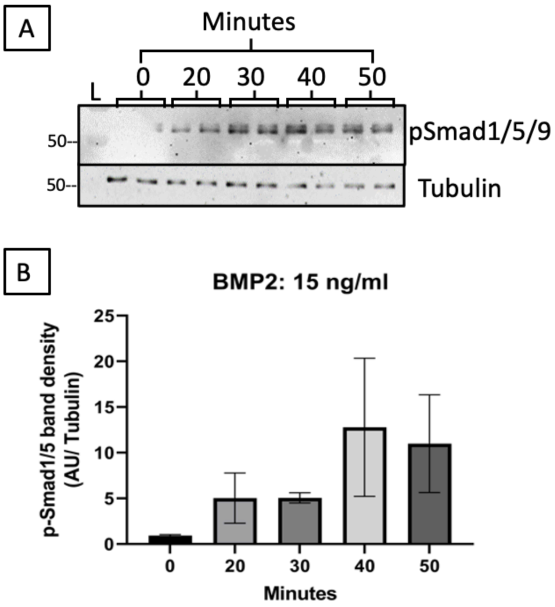

Figure 4.4: Time-dependent and dose-dependent pSmad1/5/9 activation in Y201 cells following BMP2 treatment: (A) Western blot analysis of pSmad1/5/9 phosphorylation in Y201 cells treated with 15 ng/mL BMP2 for the indicated time points. (B) Quantification of pSmad1/5/9 band density from (A) normalised to tubulin, presented as mean ± SD (arbitrary units, AU) from two technical l replicates.

Subsequently, a dose-response experiment was performed to establish a standard curve for quantifying pSmad1/5/9. Cells were treated with BMP2 concentrations ranging from 0 to 60 ng/mL, using 2.5-fold dilutions, and were harvested after 40 min. Contrary to the expectation of a linear increase in pSmad1/5/9 expression with increasing BMP2 concentration, saturation was observed at concentrations above 4 ng/mL (**Figure 4.5**). Consequently, a lower range of BMP2 concentrations is necessary to generate a reliable standard curve for pSmad1/5/9 quantification.

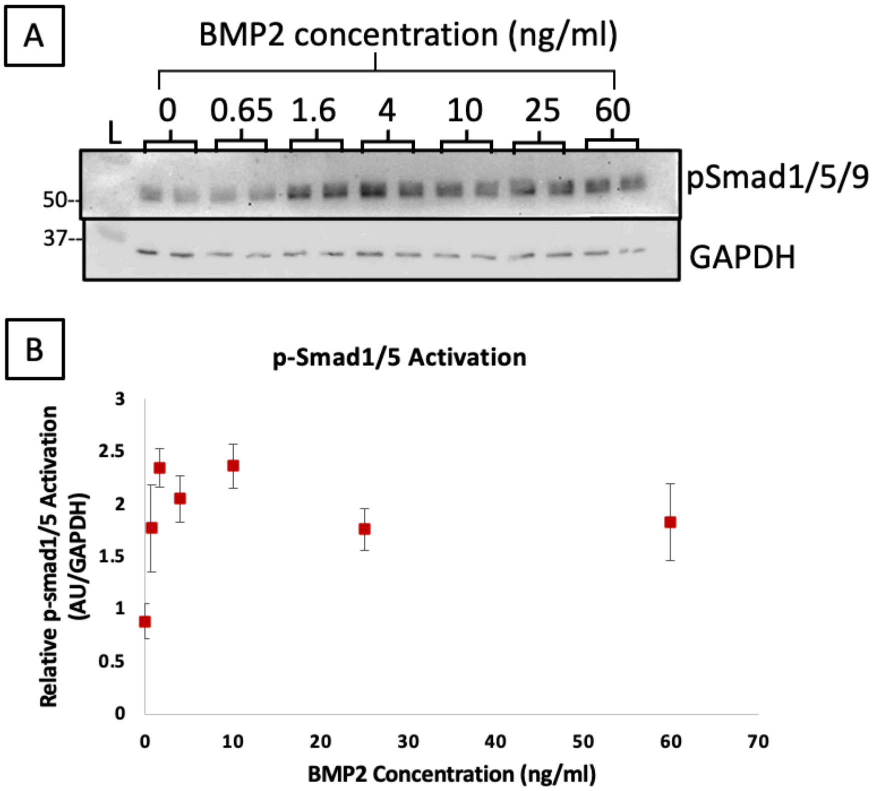

Figure 4.5: Dose-dependent pSmad1/5/9 activation in Y201 cells following BMP2 treatment: (A) Western blot analysis of pSmad1/5/9 phosphorylation in Y201 cells treated with the indicated concentrations of BMP2 for 40 min. (B) Quantification showing pSmad1/5/9 activation from (A), normalised to GAPDH. "L" represents the protein ladder.

To further optimise the assay for BMP2 bioactivity assessment, a reduced BMP2 concentration range was employed to ensure that the data points fell within the linear portion of the dose-response curves. The resulting r^2 values (0.9916, 0.9944, and 0.9397) indicated a strong linear correlation between BMP2 concentration and pSmad1/5/9 activation, suggesting the potential of the regression model for predicting BMP2 concentration based on pSmad1/5/9 band density. However, experimental replicates (**Figure 4.6**) revealed variability, and notably, the absence of a pSmad1/5/9 signal at 6 ng/mL in one replicate (**Figure 4.6** (B1)) raised concerns about the reliability of the Western blot-based assay, despite the high r^2 values. Consequently, 3 and 6 ng/mL BMP2 concentrations were excluded from the dose-response curve analysis (**Figure 4.6** (C2)) because of significant deviations from linearity, likely indicating saturation. This exclusion, although limiting the assay's dynamic range, was necessary to prevent the skewed quantification of BMP2 bioactivity and maintain data integrity.

Subsequent attempts to reproduce the dose-response relationship at an even lower concentration revealed significant challenges, mainly the variability of the pSmad1/5/9 band intensity across replicates, despite consistent tubulin loading. Consequently, the dose-response curves exhibited lower r² values (0.813 and 0.6778), indicating weaker correlations and reduced predictive power (**Figure 4.6** (D2) and (E2)). This inconsistency likely stems from the inherent limitations of western blotting, including variable protein transfer, antibody binding, ECL signal development, and imaging sensitivity. These uncontrollable factors highlight the challenges of relying solely on western blotting for accurate BMP2 bioactivity quantification. To address this, a 96-well plate-based colourimetric ALP activity assay using Y201 cell line was explored. This assay could be developed with a larger number of technical repeats, potentially offering a more robust and reproducible approach.

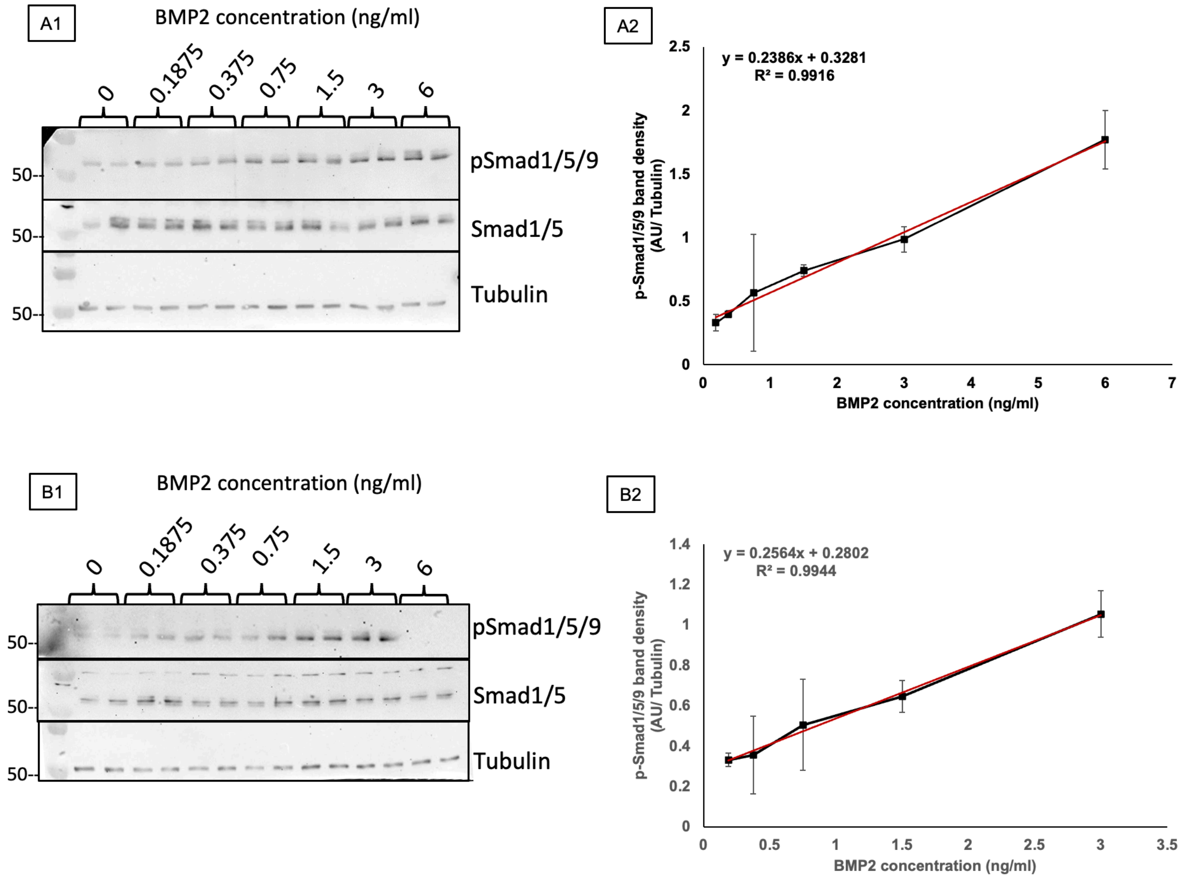

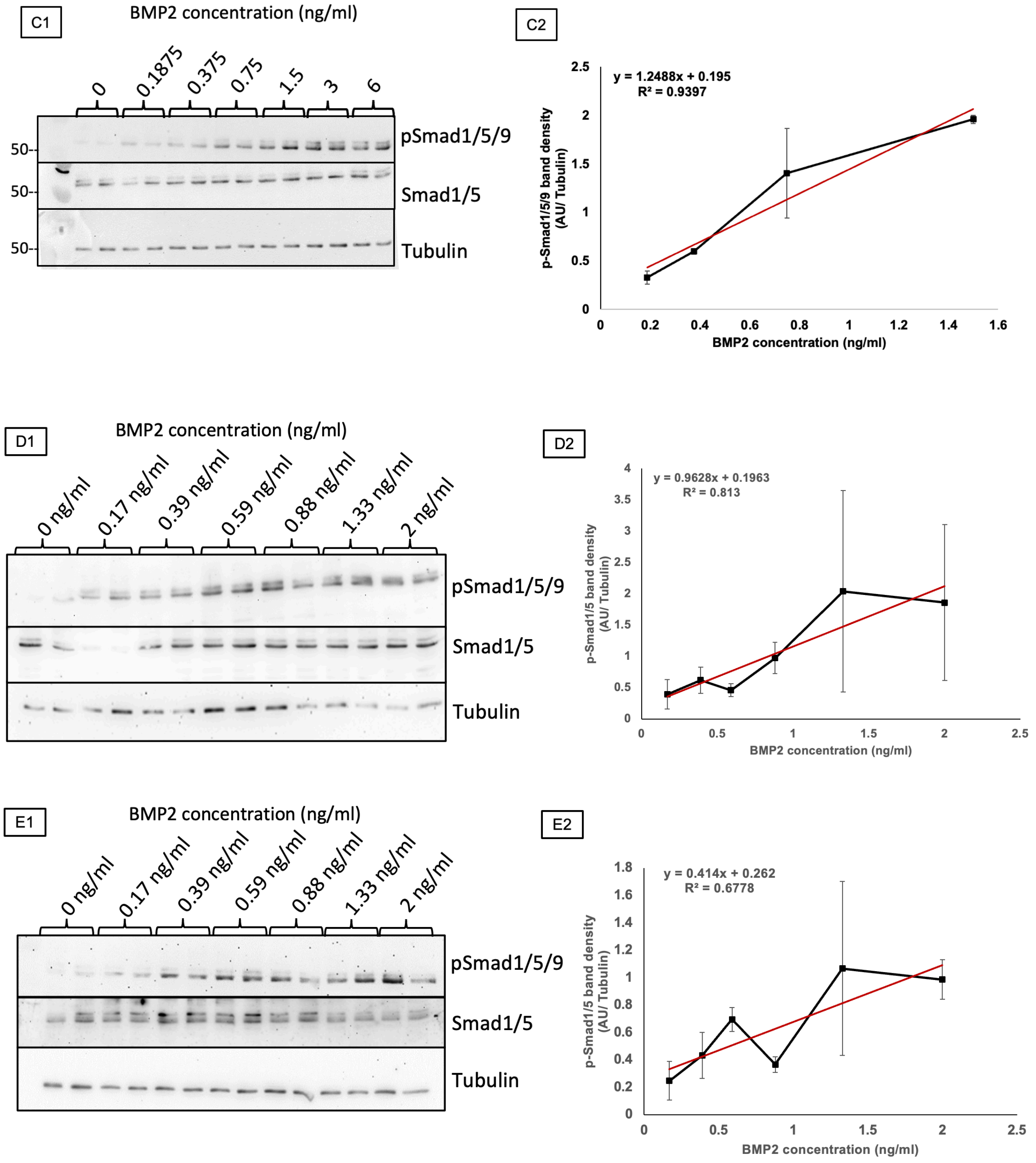

Figure 4.6: Inconsistent dose-dependent pSmad1/5/9 phosphorylation in Y201 cells following BMP2 treatment: A1, B1, C1, D1, and E1 are western blot analyses of pSmad1/5/9 phosphorylation in Y201 cells treated with the indicated concentrations of BMP2 for 40 min. A2, B2, C2, D2, and E2 are dose-response curves showing pSmad1/5/9 band density (normalised to tubulin) plotted against BMP2 concentration. Data are presented as mean ± SD (arbitrary units, AU) from two technical replicates per group.

4.2.3 Evaluation of BMP2-mediated osteogenic differentiation in Y201 Cell line

To assess the bioactivity of BMP2 released from polymer-coated SPIONs, the dose response of Y201 cells to BMP2 was first investigated. To determine the optimal BMP2 concentration for osteogenic differentiation in the Y201 cell line, ALP activity, a key early marker of osteogenic differentiation, was measured. Based on the literature demonstrating differentiation in human MSCs at 100 ng/mL BMP2 [153, 155, 156], Y201 cells were cultured for 9 days with BMP2 concentrations ranging from 5 to 100 ng/mL, using a two-fold increase between concentrations. ALP activity was quantified using a colorimetric assay that converts p-nitrophenyl phosphate (pNPP) to p-nitrophenol (pNP), and the absorbance of the latter was measured at 405 nm to directly reflect ALP activity. Osteogenic differentiation medium (ODM) served as a positive control, demonstrating robust ALP activity. However, no significant increase in ALP activity was observed across the tested BMP2 concentrations, with absorbance values remaining consistently low, similar to the medium lacking BMP2. This indicated that the tested exposure paradigms (9 days, 5-100 ng/mL BMP2) might not be sufficient to induce osteogenic differentiation in Y201 cells (**Figure 4.7** A).

To further explore the potential for BMP2-induced osteogenesis in Y201 cells, the experiment was extended to a 21-day culture period. BMP2 concentrations of 50, 100, and 200 ng/mL were tested. Additionally, given the synergistic effects of osteogenic components (dexamethasone, L-ascorbic acid, and β-glycerophosphate) with BMP2 in MSC differentiation, as reported in the literature [66, 153], the experiment was conducted both with and without osteogenic components. Furthermore, to isolate the specific effect of BMP2, a condition without dexamethasone was included in the study. However, no significant increase in ALP activity was observed in Y201 cells treated with BMP2, either at basal levels or in combination with osteogenic supplements (**Figure 4.7**).

To accurately quantify BMP2 encapsulated and released from polymer-coated SPIONs, a cellular system exhibiting a reliable and quantifiable dose-dependent response to BMP2 is essential. Two other cell line options were considered: MC3T3-E1and C2C12. Although both are responsive to BMP2, their suitability for this specific application varies. MC3T3-E1 cells, pre-osteoblastic cells, are a common model for osteogenesis studies; however, their relatively differentiated state may limit their sensitivity to BMP2 [157]. C2C12 cells, mouse myoblasts, are known for their robust and well characterised osteogenic differentiation in response to BMP2 [158, 159]. Their ability to consistently upregulate ALP activity makes them ideal for testing the suitability of measuring bioactive BMP2.

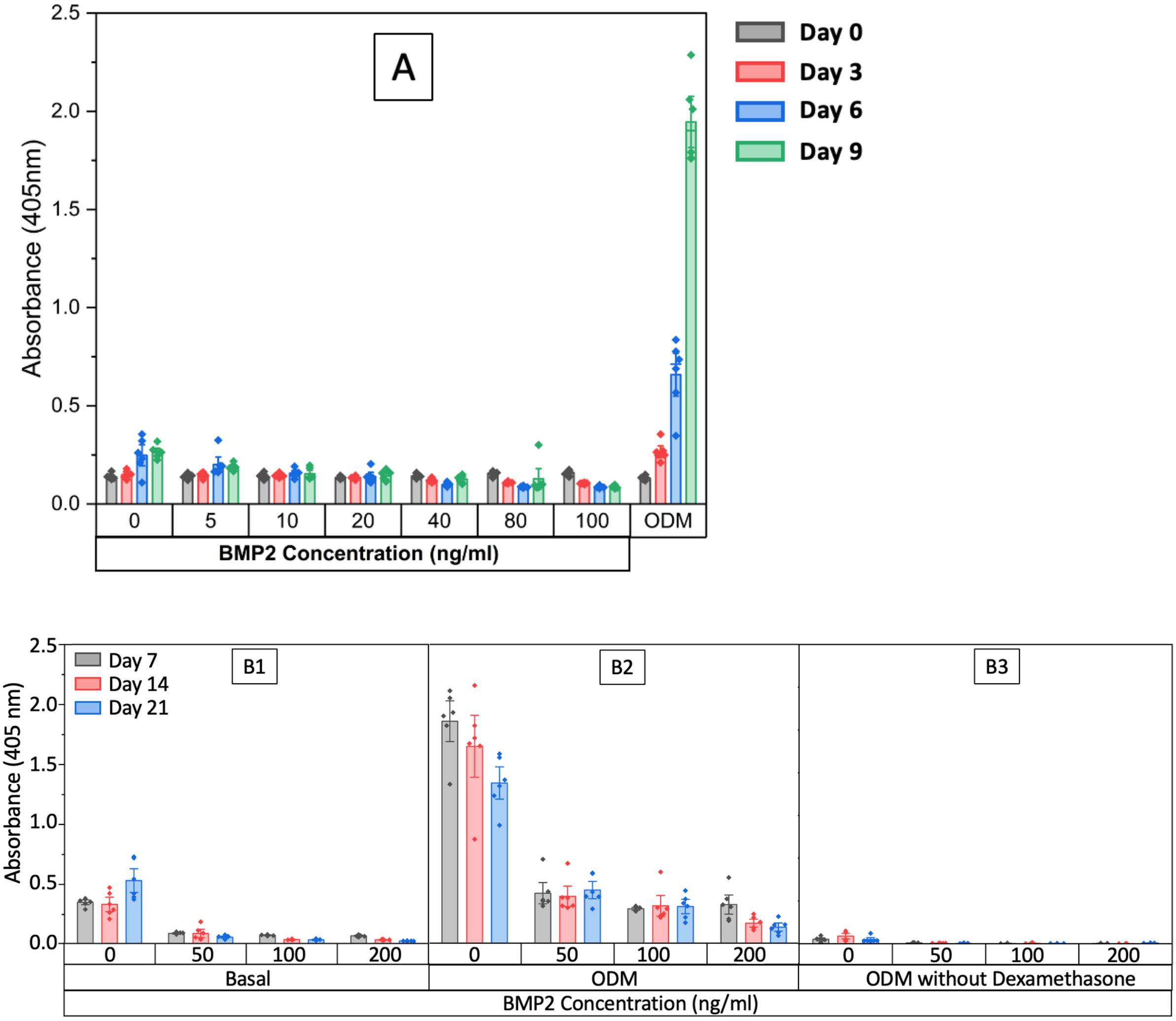

Figure 4.7: Effect of BMP2 on in vitro osteogenic differentiation of Y201 cells: (A) Y201 cells were treated with BMP2 at the indicated concentrations, and ALP activity was measured at days 3, 6, and 9 using a p-nitrophenyl phosphate (pNPP) assay. (B1, B2, B3) Y201 cells were treated with BMP2 at the indicated concentrations, and ALP activity was measured on days 7, 14, and 21 using a p-nitrophenyl phosphate (pNPP) assay. Data are presented as mean absorbance (405 nm) ± SD from six technical replicates. Osteogenic differentiation medium (ODM) was used as a positive control.

4.2.4 Effect of BMP2 on C2C12 cell line

To establish a BMP2 dose-response profile in C2C12 cells, ALP activity was measured over 9 days across a range of BMP2 concentrations (0–200 ng/mL), with a two-fold increase between each concentration. The normalised ALP activity (pNP/DNA) demonstrated a substantial increase by day 3, indicating an early response to BMP2 (**Figure 4.8** A). To further investigate this early response, we focused on time points within the first three days. This allowed for the detection of subtle ALP activity changes that may be missed at later times, which is crucial for quantifying low levels of BMP2 release. This analysis revealed a rapid increase in ALP activity within 24 h of treatment, with significant elevation observed on day 2 (**Figure 4.8** B). Thus, an early time point was essential for assessing BMP2 release from polymer-coated SPIONs. These results indicate that C2C12 cells exhibit a dose-dependent response to BMP2, with a concentration-dependent increase in ALP activity evident by day 2. This response can be used to generate a standard curve for quantifying BMP2 released from polymer-coated SPIONs.

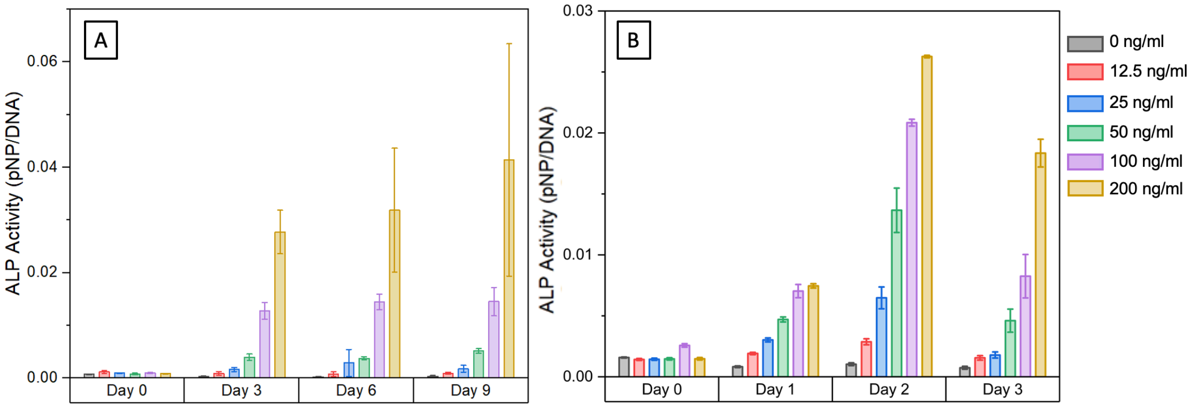

Figure 4.8: Dose-dependent ALP activity in C2C12 cells treated with BMP2: (A) and (B) ALP activity (pNP/DNA) measured on different days. C2C12 cells were treated with BMP2 at concentrations of 0, 12.5, 25, 50, 100 ng/mL, and 200 ng/mL. Data are presented as mean ± SD (N=6).

4.2.5 Glycosylated and non-glycosylated BMP2

Previous studies have demonstrated that C2C12 cells exhibit a dose-dependent increase in ALP activity in response to glycosylated BMP2. To examine the role of glycosylation, we assessed the effects of glycosylated and non-glycosylated BMP2 on C2C12 cells by measuring ALP activity following treatment with varying concentrations of each form. Glycosylated BMP2 elicited a clear dose-dependent increase in ALP activity, with a significant elevation observed at 200 ng/mL compared to 50 ng/mL and 0 ng/mL concentrations (**Figure 4.9**). In contrast, non-glycosylated BMP2 showed minimal ALP activity at all tested concentrations. These findings indicate that glycosylated BMP2 is more effective in stimulating ALP activity in C2C12 cells in a dose-dependent manner, whereas non-glycosylated BMP2 exhibits significantly reduced bioactivity.

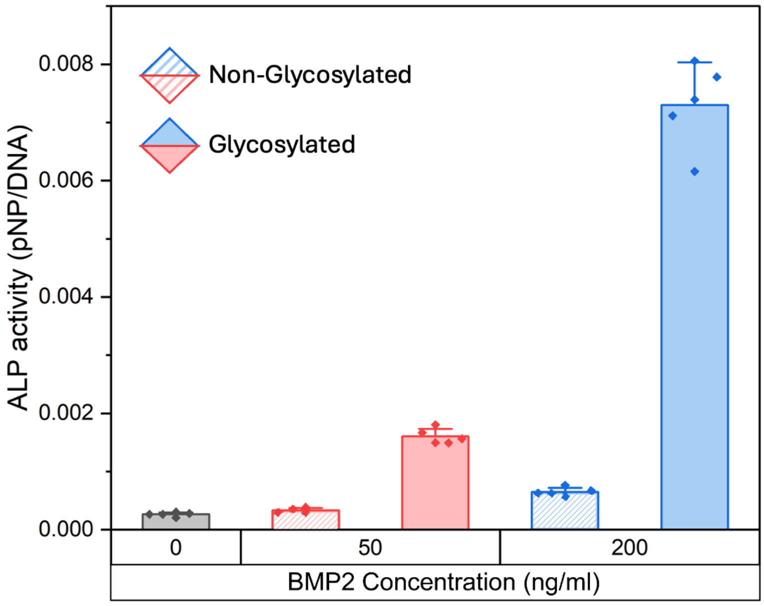

Figure 4.9: Effect of glycosylation on BMP2-induced ALP activity in C2C12 cells: ALP activity (pNP/DNA) measured at day 2, C2C12 cells were treated with BMP2 at concentrations of 0, 50, and 200 ng/mL of glycosylated BMP2 and non-glycosylated BMP2. Data are presented as mean ± SD (five technical replicates).

4.2.6 Standard curve for BMP2 induced ALP Activity in C2C12 Cells

A standard curve for quantifying bioactive BMP2 release was established by measuring the dose-dependent ALP activity in C2C12 cells on day 2 (**Figure 4.8** B). ALP activity (µmol pNP) normalised to DNA (µg) was plotted against BMP2 concentration (ng/mL), revealing a direct linear correlation, where ALP activity increased proportionally to BMP2 concentration. Linear regression analysis of this relationship yielded a high coefficient of determination ($R^2 = 0.99$) (**Figure 4.10**), indicating a strong linear fit and demonstrating that ALP activity in C2C12 cells was reliably proportional to the BMP2 concentration within the tested range. This standard curve served as a quantitative tool for assessing the bioactive BMP2 released from the polymer-coated SPIONs.

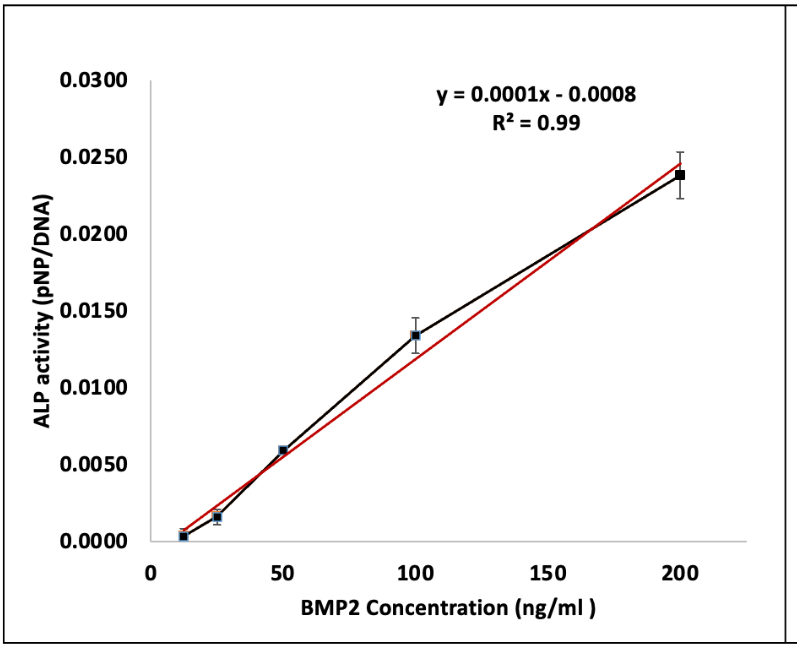

Figure 4.10: Standard curve for BMP2 bioactivity quantification using day 2 ALP activity in C2C12 cells: Relationship between BMP2 concentration (ng/mL) and ALP activity (pNP/DNA). Data are presented as mean ± standard deviation (SD) (n=6).

4.2.7 The effect of encapsulation and release temperature regime on the bioactivity of BMP2

The previous silver staining experiment demonstrated the thermal stability of glycosylated BMP2 in buffer without nanoparticles. However, this does not reflect the protein's behaviour within the complete encapsulation and release system, particularly regarding its impact on bioactivity. To bridge this gap, we conducted an ALP activity assay using C2C12 cells, as described above. This assay simulated the temperature regime and conditions of the encapsulation and release process, excluding nanoparticles, to assess whether BMP2 retained its bioactivity. This was done to ensure that any observed denaturation of BMP2 during the later experiments (with nanoparticles) was due to the nanoparticles themselves and not other parameters of the process. We also aimed to determine if any changes had to be made to the procedure to maintain BMP2 activity during encapsulation and release.

ALP activity, expressed as a percentage, was measured in C2C12 cells treated with 25, 50, and 100 ng/mL of BMP2 under various conditions: room temperature (RT) for sample handling between incubation steps, constant rotator mixing to ensure homogeneity, 37 °C incubation (1 h) as a basal release condition, and 45 °C incubation (1 h) to induce polymer phase transition during release. HEPES buffer was chosen because the encapsulation and release of protein from polymer-coated SPIONs was performed in HEPES buffer. DMEM was included to assess potential BMP2 activity in comparison with HEPES. The results demonstrated a dose-dependent increase in ALP activity in both the buffers. Importantly, no significant reduction in ALP activity was observed under any of the tested conditions, indicating that BMP2 maintained its bioactivity throughout the simulated encapsulation and release process. These findings suggest that glycosylated BMP2 retains its bioactivity after the simulated encapsulation and release process, as evidenced by ALP activity on day 2 in C2C12 cells (**Figure 4.11**). This approach enabled a biologically relevant evaluation of the BMP2's functional integrity and stability after exposure to the temperature regime and the entire simulated procedure.

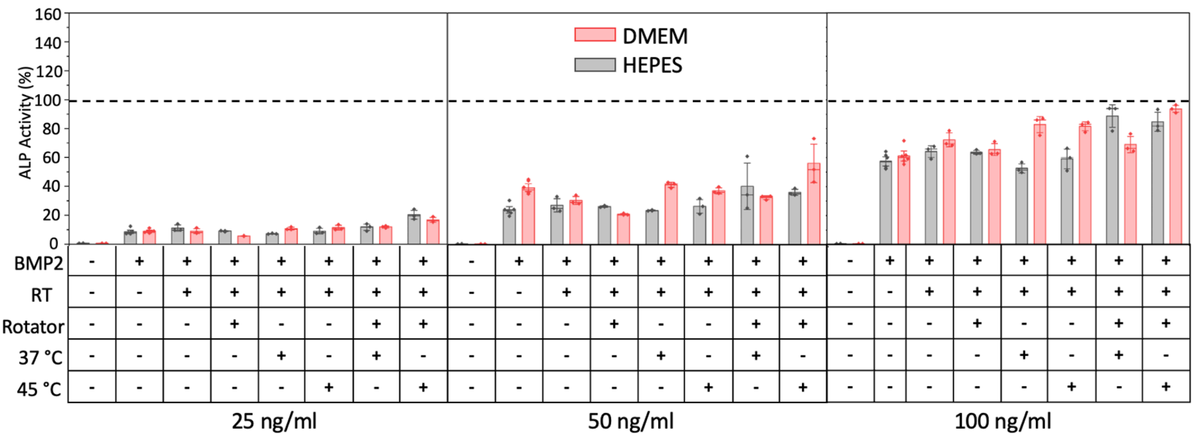

	25 ng/ml								50 ng/ml								100 ng/ml							
BMP2	-	+	+	+	+	+	+	+	-	+	+	+	+	+	+	+	-	+	+	+	+	+	+	+
RT	-	-	+	+	+	+	+	+	-	-	+	+	+	+	+	+	-	-	+	+	+	+	+	+
Rotator	-	-	-	+	-	-	+	+	-	-	-	+	-	-	+	+	-	-	-	+	-	-	+	+
37 °C	-	-	-	-	+	-	+	-	-	-	-	-	+	-	+	-	-	-	-	-	+	-	+	-
45 °C	-	-	-	-	-	+	-	+	-	-	-	-	-	+	-	+	-	-	-	-	-	+	-	+

Figure 4.11: Testing the temperature regime of BMP2 on C2C12 cells: Cells were subjected to various conditions: room temperature (RT), rotator mixing, 37 °C incubation, and 45 °C incubation. ALP activity (µmol pNP/µg DNA, expressed as %) in C2C12 cells treated with 25, 50, and 100 ng/mL glycosylated BMP2 in DMEM and HEPES buffer.

4.2.8 Using C2C12 cell line as model to detect the encapsulated and released BMP2

To accurately determine the amount of BMP2 encapsulated and released from the polymer-coated SPIONs, a corresponding standard curve was generated using known BMP2 concentrations for each encapsulation and release experiment. This approach ensured that variations in the experimental conditions were accounted for during quantification. Since 100 µL of known BMP2 concentrations were added to 96-well plates, this standard curve was used to calculate the amount of BMP2 in the samples. This allowed us to measure the amount of BMP2 present in the 20 µL samples from the unloaded, wash, and release fractions. The strong linear correlation ($R^2 = 0.99$) demonstrated the reliability of using ALP activity as a proxy for BMP2 amount in ng. The calculated BMP2 amounts from the 20 µL samples were scaled up to represent the total BMP2 in a 100 µL volume for each condition. The total amounts were presented as bar graphs. The percentages in the release graphs represent the proportion of the initial 1 µg of BMP2 loaded. A detailed workflow for determining the amount of bioactive BMP2, including the unloaded, washed, and released samples (**Figure 4.12**). This methodology enabled an accurate assessment of BMP2 encapsulation efficiency by quantifying the total amount of BMP2 in unloaded and wash samples. Similarly, we assessed the release samples at both 37 °C and 45 °C to determine the amount of BMP2 released from the BMP2-encapsulated polymer-coated SPIONs.

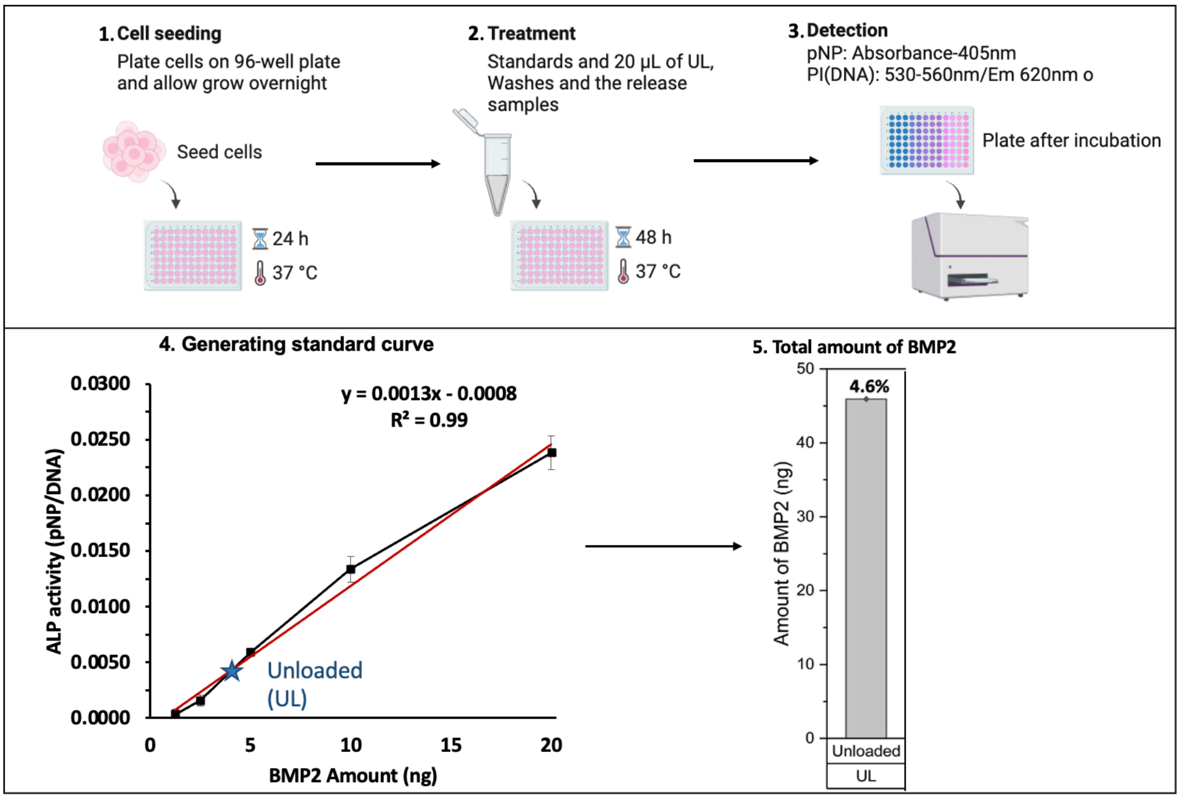

Figure 4.12: Experimental workflow used to assess bioactive BMP2 from washes and release from the polymer-coated SPIONs: (1) C2C12 cells were seeded in 96-well plates and incubated for 24 h at 37 °C. (2) Cells were treated with standards and 20 µL of 'unloaded' (UL), washed, and released samples, followed by a 48-hour incubation at 37 °C. (3) ALP activity was detected by normalising pNP absorbance at 405 nm to propidium iodide (DNA) fluorescence, which was detected using excitation at 530-560 nm and emission at 620 nm, using a CLARIOstar® plate reader. (4) A standard curve was generated relating BMP2 amount (ng) to ALP activity (pNP/DNA), with error bars representing the standard deviation. The 'Unloaded (UL)' data point is highlighted. (5) The total amount of BMP2 in the 'Unloaded' sample is shown, representing 4.6% of BMP2 compared to the initial 1000 ng.

Previous studies have consistently shown that competitor proteins typically at concentrations around 10 mg/mL are required to facilitate protein release by displacing bound proteins from polymer-coated nanoparticle surfaces [17, 18]. This requirement goes beyond simply replicating the serum environment, as serum itself has been observed to directly compete with encapsulated proteins for binding sites [18]. To investigate the influence of competing proteins on BMP2 release, four distinct competitor proteins were tested: ovalbumin, IgG, apotransferrin, and RNase B. These were selected based on prior work that had established a framework using these proteins, as well as to represent a range of molecular weights (15–160 kDa) states features characteristic of proteins found in human extracellular fluids [18].

The aim of these experiments was to encapsulate BMP2 within the polymer-coated SPIONs, demonstrate its successful encapsulation, quantify the encapsulated amount, and subsequently characterize its controlled release profile. As a first step, BMP2 was incubated with the polymer-coated SPIONs to facilitate encapsulation. Successful encapsulation was then confirmed by quantifying the unbound protein. In the following sections, Panel (A) presents the amount of BMP2 found in the 'Unloaded' (UL) sample, which represents protein that did not bind to the SPIONs during the initial encapsulation step. Subsequent washes were performed in the presence of competitor protein to remove any remaining unbound or loosely bound protein. The sum of the protein in the UL sample and these subsequent wash fractions directly indicates the total quantity of BMP2 that was not successfully encapsulated, thereby allowing for the calculation of BMP2 that is encapsulated within the polymer-coated SPIONs.

The BMP2 encapsulated polymer-coated SPIONs after washes are then subjected to the release in the presence of the same competitor protein used during the washes, In the following sections, Panel (B) shows the cumulative amount of BMP2 released from the SPIONs over a one-hour period. Release experiments were performed at two temperatures: 37 °C, to assess basal release at physiological temperature**,** and a temperature above 37 °C, to evaluate release triggered by the polymer’s phase transition. Released BMP2 is expressed in nanograms (ng). The percentages above each bar indicate.

4.2.8.1 Competitor protein ovalbumin mediated BMP2 release from polymer-coated SPIONs

Ovalbumin was chosen as the competitor protein due to its ability to release other proteins, such as apotransferrin (~15% release at 45 °C) and IgG (~12% ng) [18]. The 'unloaded' sample contained 4.6%. Successive washes demonstrated a progressive decrease in BMP2, with W1 containing 3.8% and W2-W5 showing consistently low amounts (0.6%, 0.5%, 0.6%, and 0.5%, respectively). This data indicates that approximately 90% of BMP2 was encapsulated (**Figure 4.13** A). The cumulative release of BMP2 from the SPIONs was minimal at 37 °C (0.7-0.8% of the total protein) across all time points (15, 30, and 60 min). However, a notable increase in BMP2 release was observed at 45 °C, demonstrating a time-dependent release profile, with the highest release occurring at 60 min (1.4% of total protein). Despite the temperature-triggered release, the overall percentage of BMP2 released from SPIONs remained low (**Figure 4.13** B). Ovalbumin was unable to achieve substantial BMP2 release from the polymer-coated SPIONs, suggesting a strong interaction between BMP2 and the polymer coating that may limit its therapeutic availability under these conditions. These findings indicate that although PNIPMAM-coated SPIONs can effectively encapsulate BMP2, achieving significant and controlled release using ovalbumin as a competitor protein presents a challenge that requires further investigation.

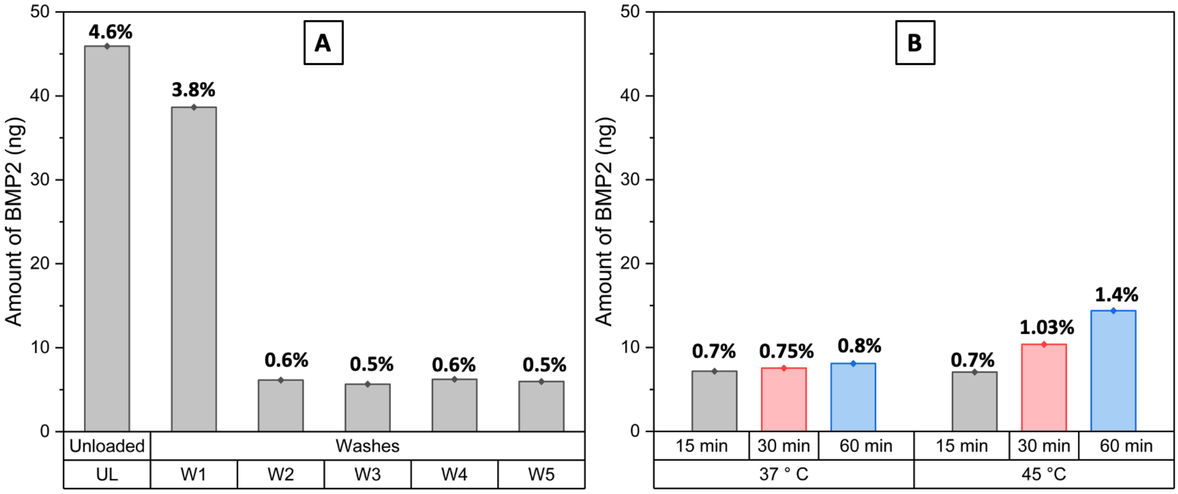

Figure 4.13: Ovalbumin-mediated release of BMP2 from PNIPMAM-coated SPIONs. (A) BMP2 in 'Unloaded' sample and washes after encapsulation. (B) BMP2 release at 37 °C and 45 °C in the presence of ovalbumin. The percentages are relative to the initial 1000 ng of BMP2.

4.2.8.2 IgG competition mediated BMP2 release from polymer-coated SPIONs

Given that IgG previously facilitated a 30% release of encapsulated apotransferrin at 45 °C and achieved ~90% encapsulation efficiency with polymer-coated SPIONs [18], it was investigated as a competitor protein for BMP2 washing and release. First, the encapsulation efficiency was evaluated. The 'Unloaded' sample contained a small amount of BMP2, indicating approximately 99% protein encapsulation as compared to the previous experiment, which was a 5% increase in the encapsulation. Subsequent washes revealed 7% BMP2 in W1, suggesting the removal of loosely bound BMP2. Washes W2-W5 showed a further minimal BMP2 removal of 1.2% (**Figure 4.14** A), indicating that over 90% of the BMP2 was effectively encapsulated. The release profile was minimal at both 37 °C and 45 °C over time (**Figure 4.14** B). Notably, the presence of bovine IgG as a competitor protein, similar to ovalbumin in previous experiment, did not significantly enhance BMP2 release, as the overall release remained relatively low even at elevated temperature.

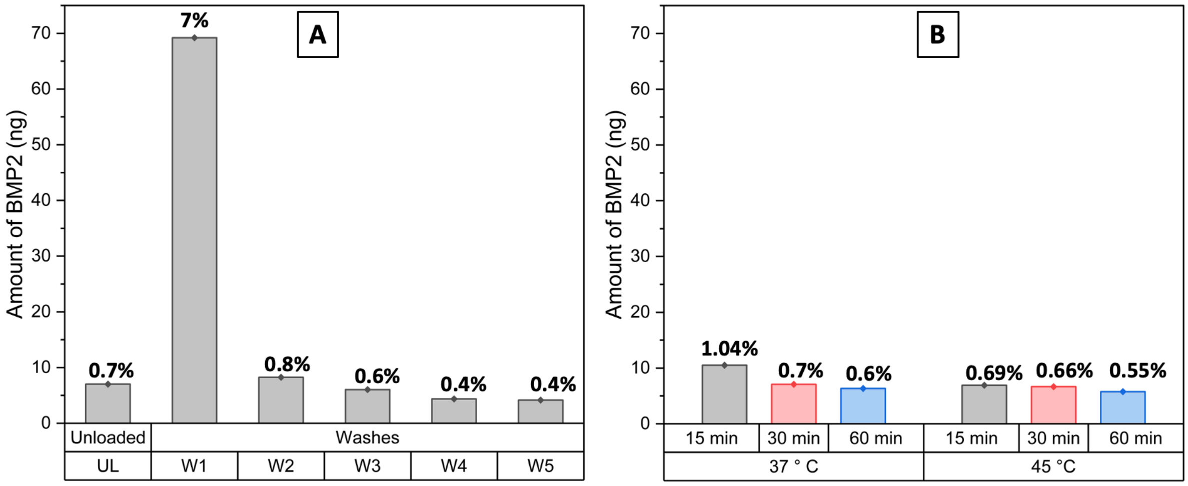

Figure 4.14: IgG-mediated Release of BMP2 from PNIPMAM-coated SPIONs: (A) BMP2 in 'Unloaded' sample and washes after encapsulation. (B) BMP2 release at 37 °C and 45 °C in the presence of ovalbumin. The percentages are relative to the initial 1000 ng of BMP2.

4.2.8.3 Competitor protein apotransferrin mediated BMP2 release from polymer-coated SPIONs

Next, we tested apotransferrin as a competitor, which has previously been successfully encapsulated with 40% efficiency [18]. However, its role as a competitor in release studies has not been examined. The 'Unloaded' sample (0.7%) indicated approximately 99% protein encapsulation, similar to the previous experiment. However, W1 revealed 6.3% of BMP2, suggesting potential protein displacement or removal of some BMP2 that are loosely bound. Subsequent washes (W2-W5) showed a further decrease in BMP2, but still indicated slightly low amounts (1.8%, 1.4%, 0.9%, 0.7%), confirming approximately 90% BMP2 protein encapsulation (**Figure 4.15** A). The release profile showed a slight increase in release at 45 °C compared to 37 °C over 1 h, but not at earlier time points. However, the overall release remained relatively low. Notably, the presence of apotransferrin as a competitor protein, like bovine IgG and ovalbumin in previous experiments, showed minimal BMP2 release at the elevated temperature (**Figure 4.15** B).

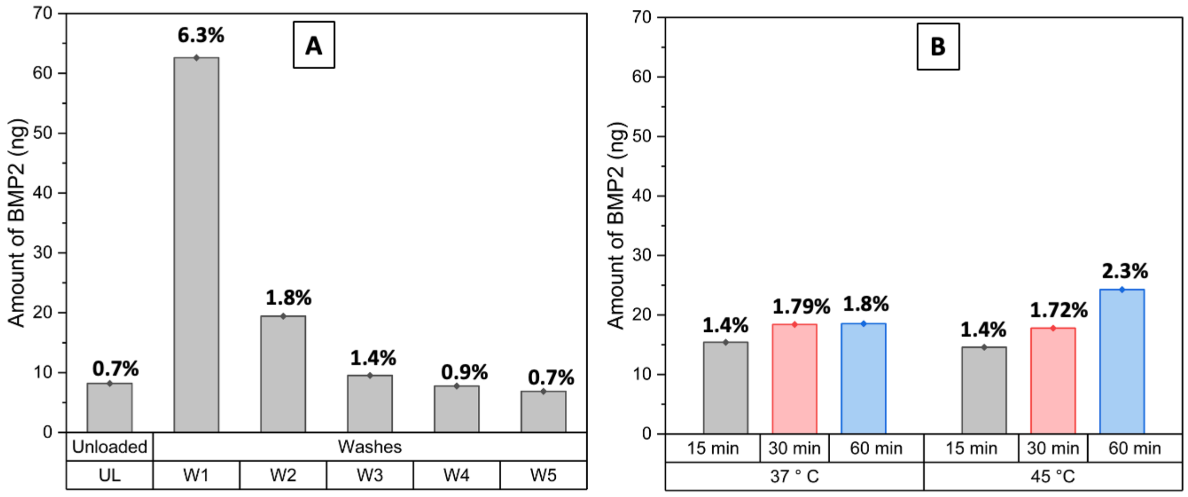

Figure 4.15: apotransferrin-Mediated Release of BMP2 from PNIPMAM Nanoparticles. (A) BMP2 in 'Unloaded' sample and washes after encapsulation. (B) BMP2 release at 37 °C and 45 °C in the presence of ovalbumin. The percentages are relative to the initial 1000 ng of BMP2.

4.2.8.4 Competitor protein RNaseB mediated BMP2 release from polymer-coated SPIONs

RNase B was used as a competitor protein based on previous studies indicating efficient release with glycosylated compared to non-glycosylated RNase A, which shares the same sequence. Prior experiments using RNase B as a competitor showed 8% Wnt3a release and 2% temperature triggered apotransferrin release [17, 18]. To investigate its effect on BMP2 release, the 'Unloaded' sample contained 0.08% BMP2, suggesting an high protein with 99% encapsulation, consistent with previous experiments. However, the first wash (W1) revealed a moderate 5% BMP2, and subsequent washes (W2-W5) showed similar amounts (4.8%, 4.3%, 4.3%, 4.3%), indicating moderate protein loss and an estimated BMP2 encapsulation of approximately 77% (**Figure 4.16** A). This higher percentage of BMP2 in the wash samples compared to the washes when ovalbumin or IgG was used could be due to displacement by or competition with RNase B. For the release, a temperature-time dependent profile was assessed at 37 °C and 45 °C over one hour. However, overall BMP2 release remained relatively indifferent across temperatures (**Figure 4.16** B). Notably, RNase

B, unlike bovine IgG, ovalbumin, and apotransferrin, resulted in a slightly enhanced 6.4% compared to 0.7-2.3% with other proteins in the previous experiments at 45 °C, but BMP2 release remained similar at both physiological and elevated temperatures. This might indicate that BMP2 was loosely bound to the polymer-coated SPIONs or that RNase B played a role in replacing the encapsulated BMP2. To further investigate the nature of BMP2 binding and the potential displacement by RNase B, the number of washes was increased in subsequent experiment with the hypothesis that more loosely bound BMP2 would be removed, potentially affecting the subsequent release profile of BMP2.

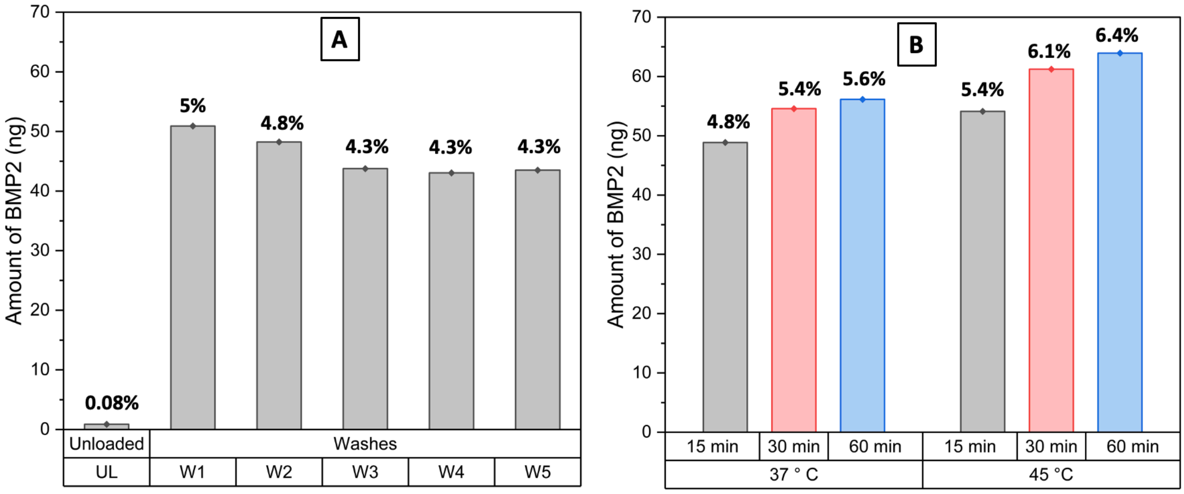

Figure 4.16: RNase B-mediated release of BMP2 from PNIPMAM nanoparticles. (A) BMP2 in 'Unloaded' sample and washes after encapsulation. (B) BMP2 release at 37 °C and 45 °C in the presence of ovalbumin. The percentages are relative to the initial 1000 ng of BMP2.

In the experiment with added washes, the 'Unloaded' (UL) sample indicated that 3.3% of the initial BMP2, indicating ~94% encapsulation. Subsequent washes (W1-W10) consistently removed detectable amounts of BMP2, culminating in a significant total loss of 76.7% of the initially added protein amount. This substantial loss during washing resulted in a low estimated BMP2 encapsulation efficiency of approximately 20%, suggesting that a large fraction of BMP2 remained unbound or was displaced from the SPIONs (**Figure 4.17** A). This led to poorer encapsulation compared to previous experiments, in which fewer washes were performed. The subsequent release at 45 °C ranged narrowly from 8.9% to 9% across the measured time points (15, 30, and 60 min), and a similarly constrained release (9.1% to 9.9%) was observed at 45 °C (**Figure 4.17** B). This release was observed to be nearly equal amount at both 37 °C and 45 °C, in contrast with observations for other competitor proteins like Ovalbumin, IgG, and apotransferrin, where minimal release of BMP2 was observed at both temperatures. This suggests that the released BMP2 was not weakly bound to the polymer-coated SPIONs. Instead, the observed results suggest that in the presence of RNase B, BMP2 was likely efficiently displaced during the washing steps, leading to poor encapsulation and a non-temperature responsive release.

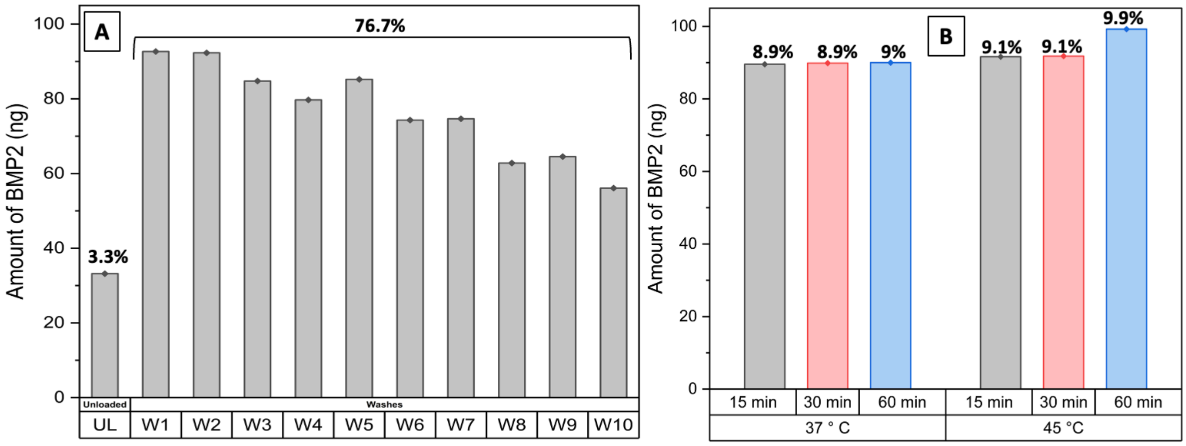

Figure 4.17: RNase B-mediated release of BMP2 from PNIPMAM nanoparticles with an increase in washes: (A) BMP2 in 'Unloaded' sample and washes after encapsulation. (B) BMP2 release at 37 °C and 45 °C in the presence of ovalbumin. The percentages are relative to the initial 1000 ng of BMP2.

4.2.9 Releasing the encapsulated BMP2 at pH-11.5.

Previous findings on apotransferrin showed pH-dependent release patterns, indicating that an increase in pH facilitated the detachment of apotransferrin from PNIPAM-coated SPIONs [17]. Given that BMP2 exhibited strong binding to the PNIPMAM-coated SPIONs, we investigated whether BMP2 exhibited high pH-dependent release like apotransferrin. To assess this, BMP2 was encapsulated at its typical encapsulation pH of 7.4, and release was performed at pH 11.5 because the highest apotransferrin release was observed at this pH. To assess the presence of BMP2 in the release samples and potentially quantify the amount released at elevated pH, this was assessed using silver staining of the gel, which revealed the presence of BMP2 across the various release fractions collected. To enable the estimation of the released BMP2 concentration, a series of decreasing concentrations of

BMP2 (2.5, 5, 10 and 20 ng) were loaded onto the gel as a standard. As expected, this standard series demonstrated a clear concentration-dependent decrease in band intensity, providing a reference for comparison with the bands observed in the release samples. The 'Unloaded' (UL) lane showed intensity similar to the 5ng standard, indicating the presence of unbound BMP2 that did not associate with the SPIONs during the encapsulation process. The wash fractions (W1, W2, and W3) displayed faint or no bands, suggesting that the washing procedure effectively removed unbound BMP2 without the use of a competitor protein. The absence of intense bands in these lanes indicates successful removal of loosely bound protein from the SPIONs and suggests that a high percentage of BMP2 (potentially around 95%) was effectively encapsulated. The '3 days' lane, representing the encapsulated BMP2 with SPIONs sample kept at pH 11.5 for three days to induce release, showed no visible band. This absence of a band might be due to the strong adherence of BMP2 to the polymer-coated SPIONs, preventing its release and subsequent detection.

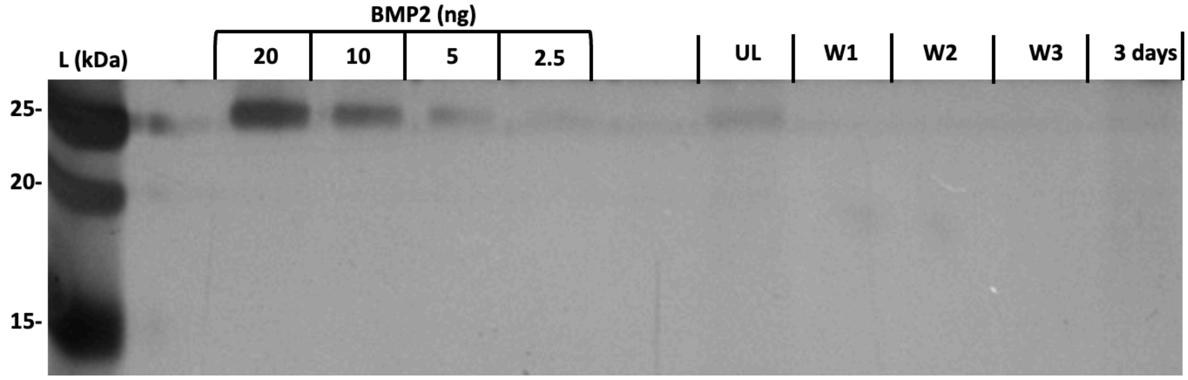

Figure 4.18: Silver staining of BMP2 showing encapsulation at pH 7.4 and release at pH 11.5: protein ladder L (kDa), BMP2 standards (20-2.5 ng), and unloaded (UL) and wash (W) fractions, 3 days representing release at pH 11.5.

4.3 Conclusion

This chapter aimed to utilise the PNIPMAM-coated SPION-based delivery system developed in the previous chapter to encapsulate and characterise the release of bioactive BMP2. As the toxicity and differentiation assays had been conducted in the Y201 cell line, this model was initially selected to assess bioactive BMP2, given that its responsiveness to BMP2 had not previously been tested. However, Y201 cells proved only partially responsive: while they activated the BMP2 signalling pathway, they produced insufficient ALP activity for reliable quantification, making it difficult to perform the full set of confirmatory assays on the released bioactive BMP2. The limited responsiveness of human MSCs to BMP2 has also been reported in other studies, supporting the present findings [92, 152].

An alternative model was then explored. C2C12 cells, a mouse myoblast line, demonstrated robust responsiveness to BMP2 demonstrated by several studies [80, 87, 94, 160], with detectable ALP activity across a concentration range of 6.25–200 ng/ml. Importantly, BMP2 retained full activity following exposure to these conditions. Encapsulation and release experiments of BMP2 released from the polymer-coated SPIONs. The nanoparticles achieved approximately 95% protein encapsulation. However, the release profiles at 37 °C and 45 °C showed minimal differences in the presence of previously studied competitor proteins. In the previous studies showed that glycosylation influences release dynamics [18]. However, the inclusion of ovalbumin, a glycosylated protein, had no measurable effect on BMP2 release in this study, suggesting that glycosylation alone is not the determining factor. It was also shown that protein size could influence the release which could be true as all of the competitor proteins examined were larger than BMP2, except RNase B, which is smaller [18]. Notably, RNase B promoted the release of BMP2, supporting that size can affect encapsulation and release behaviour. But, this effect was observed at both temperatures, implying that size-related competition may contribute to BMP2 displacement but is insufficient to drive a temperature-dependent release profile. These findings indicate that while the platform is effective at protein encapsulation, additional factors such as protein size, protein's charge and competitive binding might play key roles in governing release.

I also tested release at a higher pH, as previous work had shown that apotransferrin was released more effectively under alkaline conditions than at physiological pH when using

PNIPAM-coated SPIONs [17]. I wanted to determine whether the same applied to BMP2, but no release was observed. One possibility is that BMP2 was completely denatured at high pH, making it undetectable. However, a study reported that unglycosylated BMP2 was less stable at pH 11 at room temperature than under neutral conditions, yet it still retained some structural integrity and biological activity [161]. Based on this, it is also possible that glycosylated BMP2 did not fully denature but instead remained strongly bound to the SPIONs. According to a study, this strong binding to the SPIONs is likely due to multiple factors, including its amino acid sequence, native protein conformation, isoelectric point, and surface potential. Specifically, cysteine residues which are strong candidates for binding to the nanoparticle surface [162]. This strong affinity contrasts with apotransferrin, which is known to bind poorly to SPIONs, in part due to its availability if less cysteine residues to bind with the magnetic nanoparticles [162]. Taken together, these factors are likely to have created a tight association that prevented BMP2 release, even under alkaline conditions.

Since BMP2 did not exhibit the desired temperature-dependent release for which the nanoparticles were designed, the next chapter shifts focus to the encapsulation and delivery of Wnt3a using PNIPMAM-coated SPIONs. The aim is to evaluate whether this system can be applied to other proteins, thereby positioning PNIPMAM-coated SPIONs as a versatile delivery platform for targeting specific signalling pathways and advancing their potential applications in regenerative medicine. Wnt3a represents a particularly compelling candidate due to its central role in promoting proliferation, regulating osteoblast differentiation, maintaining bone homeostasis, and its synergistic interactions with BMP2 signalling pathways. Importantly, a system to test Wnt3a bioactivity had already been established within this project, providing a robust platform for evaluating its delivery. Previous studies have also investigated Wnt3a in conjunction with PNIPAM-coated SPIONs, demonstrating the feasibility of encapsulation and controlled release using thermos-responsive polymers.

Chapter 5

5. Encapsulation and release of Wnt3a

5.1 Aims and rationale

Wnt3a, is a secreted glycoprotein belonging to the Wnt family of signalling molecules. Beyond its crucial functions during embryogenesis [163], Wnt3a signalling has emerged as a key regulator in adult tissue homeostasis and regeneration, holding significant therapeutic potential for conditions such as bone fracture healing [111, 164]. However, the clinical translation of Wnt3a is hampered by several limitations. The protein exhibits a relatively short half-life *in vivo* and is prone to aggregation and denaturation, particularly under physiological conditions [114]. Systemic administration of recombinant Wnt3a can also lead to undesirable off-target effects due to its widespread influence on various cell types and signalling pathways [165]. Therefore, the development of controlled and localised delivery systems capable of preserving Wnt3a bioactivity is paramount for realising its therapeutic potential.

Biomolecule entrapment and release from temperature-responsive polymers continue to be an active area of investigation, extending beyond small molecules to encompass more complex therapeutics. Recent research has demonstrated the potential of stimuli-responsive nanomaterials for the controlled release of complex therapeutics. For instance, a near-infrared (NIR)-responsive collagen hydrogel system was developed for controlled, dual delivery of proangiogenic growth factors (PDGF/VEGF). This system utilizes gold nanorods-conjugated liposomes, enabling independent and rapid growth factor release via NIR-induced membrane changes. Its deep tissue penetration makes it suitable for in vivo applications [166]. Another study developed PLGA nanocapsules incorporating both VEGF165 and SPIONs were developed for potential local delivery in human brain endothelial cells. These nanocapsules exhibited sustained VEGF165 release (over two weeks) while maintaining protein bioactivity [167].

Despite such advancements, there remains a critical need for systems capable of delivering proteins in a truly controlled manner to target sites, necessitating release mechanisms that are more precisely tuned to specific physiological conditions [168]. In this context, SPIONs offer unique advantages due to their inherent magnetic properties, which enable non-invasive, externally controlled targeted delivery to specific tissue sites [9].

Building on this in the previous chapter, we established the efficacy of this system for the controlled release of BMP2, demonstrating temperature-responsive release behaviour attributed to the thermosensitive properties of the PNIPMAM. However, this approach did not yield the desired release. While protein size is certainly a key consideration, it is unclear to what extent the overall protein release from nanoparticle matrices can also be significantly influenced by various other factors, such as the presence of competing proteins that can interact with the nanoparticle surface or the degree of protein encapsulation.

In Chapter 2, we also explored the effects of several competitor proteins (ovalbumin, IgG, apotransferrin, and RNase B) on the release of BMP2 from a nanoparticle system. The findings revealed minimal temperature-dependent release of BMP2 in the presence of most competitor proteins, with the notable exception of RNase B, which facilitated its release at both 37 °C and 45 °C. This observation suggests a potential role for protein size in the competitive displacement mechanism [18]. Given that BMP2 (28 kDa) and Wnt3a (approximately 42 kDa) are both larger than RNase B (15 kDa), we hypothesized that the competitor proteins, particularly RNase B, previously investigated for BMP2 release might exhibit a similar effect on Wnt3a release.

Therefore**,** the current chapter focuses on the encapsulation and release of Wnt3a using the developed PNIPMAM-coated SPION platform, addressing the gap as Wnt3a has not been encapsulated using PNIPMAM-coated SPIONs before. A critical aspect of designing effective protein delivery systems, especially for growth factors like Wnt3a, is maintaining their structural and functional integrity during both encapsulation and subsequent release. Previous studies in our laboratory indicated that Wnt3a is particularly susceptible to heat-induced inactivation, losing its bioactivity at temperatures above 37 °C. Preventing such denaturation represented one of the primary challenges addressed in this work, leading us to investigate various formulation strategies to enhance Wnt3a's thermal stability and preserve its integrity within the PNIPMAM-coated SPIONs. This chapter provides critical insights into the feasibility of using PNIPMAM-coated SPIONs for controlled, bioactive protein delivery of Wnt3a, thereby optimizing the platform for therapeutic applications.

5.2 Results

5.2.1 Wnt Reporter System

To assess the bioactivity of released Wnt3a, we employed a well-established Wnt reporter cell line [17, 169]. This reporter cell line is responsive to part of canonical Wnt/β-catenin signalling pathway, produce GFP which can be used as a readout. The production of GFP in the reporter cell line upon exposure to Wnt3a serves as a sensitive and reliable indicator of its bioactivity (**Figure 5.1**). This system was employed to quantify the bioactive Wnt3a released from the nanoparticles across a 6.25-100 ng/mL concentration range. This will facilitate the establishment of a dose-response curve, allowing for the evaluation of the protein's functional integrity post-encapsulation and release.

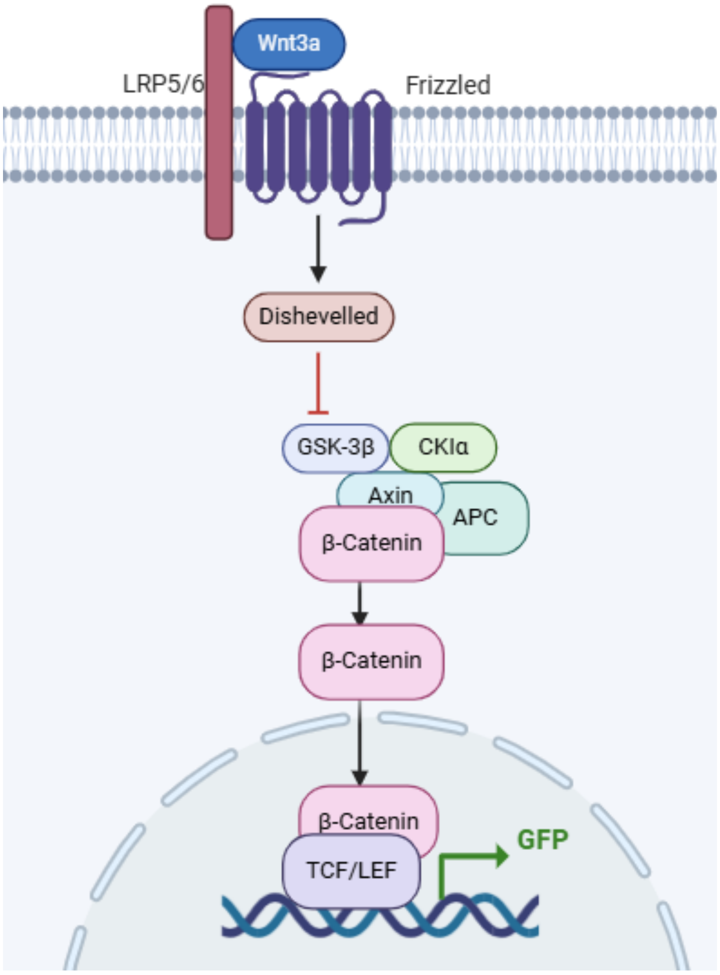

Figure 5.1: Schematic representation of the canonical Wnt/β-catenin signalling pathway and the Wnt3a reporter assay: Binding of Wnt3a to its receptors, Frizzled and LRP5/6, initiates a signalling cascade that activates Dishevelled. Activated Dishevelled inhibits the β-catenin destruction complex, composed of GSK-3β, CK1α, Axin, and APC. This inhibition prevents the phosphorylation and subsequent degradation of β-catenin, leading to its accumulation in the cytoplasm and translocation into the nucleus. In the nucleus, β-catenin associates with TCF/LEF transcription factors to activate the expression of target genes, including the reporter gene for GFP.

5.2.2 Validation of a Wnt reporter cell line assay for quantifying bioactive Wnt3a

Wnt3a bioactivity was measured using a Wnt reporter cell line that expresses GFP upon activation of the canonical Wnt/β-catenin signalling pathway. Flow cytometry dot plots illustrate the cellular response to increasing concentrations of Wnt3a (0–100 ng/ml) in a 2-fold dilution series. Flow cytometry dot plots illustrate the cellular response to increasing concentrations of Wnt3a (0–100 ng/ml) in a 2-fold dilution series (**Figure 5.2**). A clear, dose-dependent increase in the percentage of GFP-positive cells (gated in green) was observed with higher Wnt3a concentrations, indicating the corresponding activation of the Wnt/β-catenin pathway (**Figure 5.2**A). The percentage of GFP-positive cells ranged from 0.61 % in the absence of Wnt3a to 54.12 % at the highest concentration tested. This relationship is quantified by plotting the percentage of GFP-positive cells against the amount of Wnt3a used in the assay. The resulting graph demonstrated a strong linear correlation between the amount of Wnt3a and the percentage of activated reporter cells, as evidenced by the high coefficient of determination ($R^2 = 0.9931$) (**Figure 5.2**B). These results confirmed the bioactivity of Wnt3a used in this study and establish a reliable standard curve that can be utilized to quantify the amount of bioactive Wnt3a released from the nanoparticle delivery system in subsequent experiments. The observed dose-dependent activation of the Wnt/β-catenin pathway validates the sensitivity and responsiveness of the reporter cell line to Wnt3a.

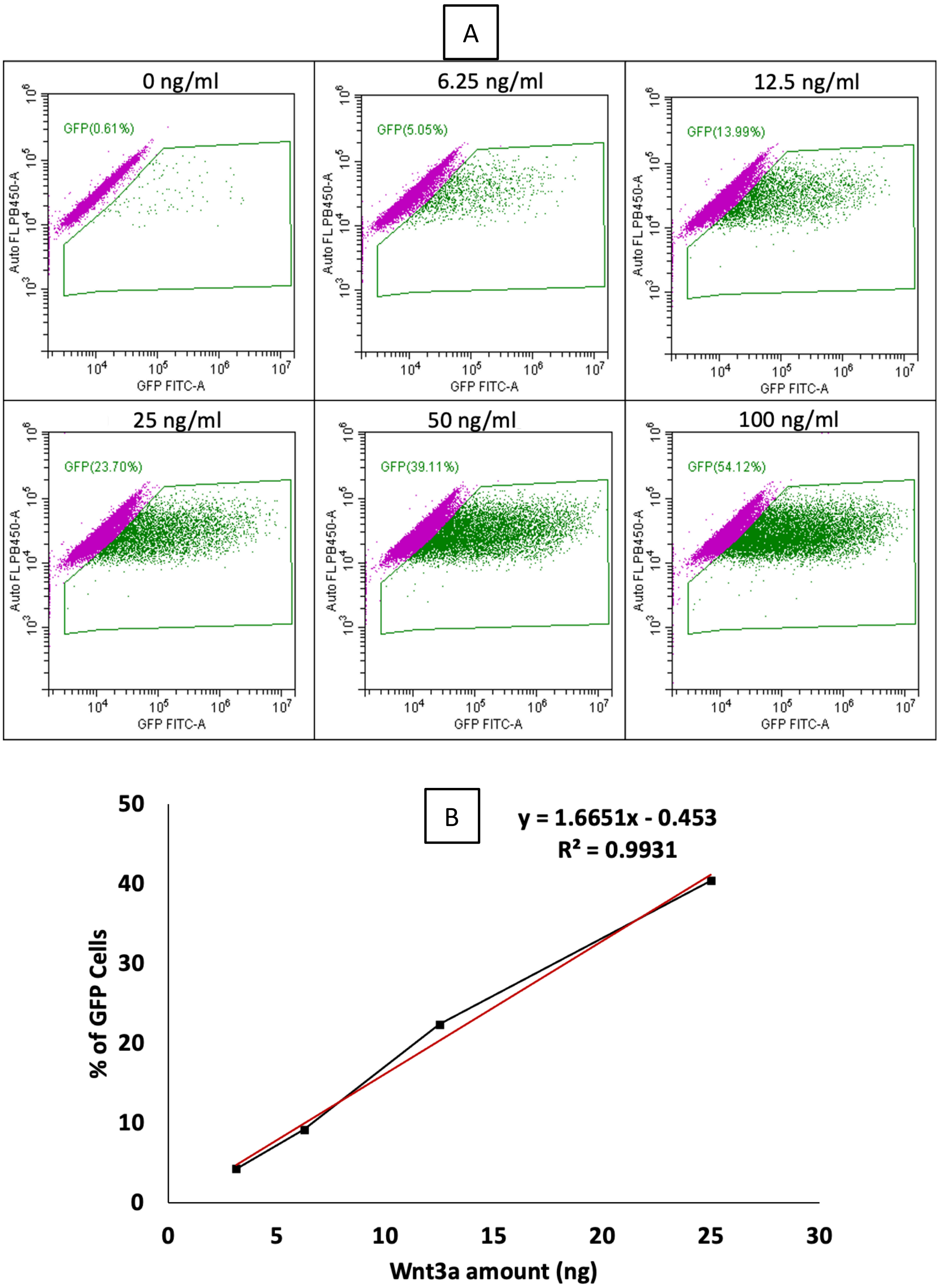

Figure 5.2: Flow cytometry analysis of Wnt reporter cell line: Panel (A) displays flow cytometry dot plots illustrating the percentage of GFP-positive cells (gated in green) treated with Wnt3a. The percentage of GFP-positive cells is indicated in the top left corner of each plot. The bottom graph (B) plots the percentage of GFP-positive cells against the corresponding amount of Wnt3a (calculated based on 500 µL used in the assay).

5.2.2.1 Optimization of Wnt3a bioactivity assay for enhanced sensitivity

For effective assessment of our nanoparticle delivery system's performance, precise and reliable quantification of bioactive Wnt3a is fundamental. Therefore, to establish the most sensitive assay conditions for this quantification in subsequent experiments, we evaluated the dose-response of Wnt reporter cells across different well formats (48-well and 24-well) and varying volumes of Wnt3a solution (150 µL, 200 µL, and 250 µL for 48-well; 250 µL, 375 µL, and 500 µL for 24-well) at the same concentrations (0–50 ng/ml). The percentage of GFP-positive cells following treatment was measured under different conditions. A clear, dose-dependent increase in Wnt signalling was observed across all tested conditions. The total amount of Wnt3a per well directly influenced the magnitude of the response, as indicated by the maximum percentage of GFP-positive cells.

To further analyse the assay sensitivity, linear regression was performed for each well format and volume, plotting the percentage of GFP-positive cells against the calculated amount of Wnt3a (in ng) per well (**Figure 5.3**). Strong linear correlations ($R^2 > 0.98$) were observed across all conditions, confirming a reliable dose-response relationship within the tested range of Wnt3a. The slopes of these linear regressions, indicative of the assay sensitivity to the amount of Wnt3a, differed depending on the well format and volume. For example, the 48-well plate with 150 µL exhibited steeper slopes, suggesting a higher sensitivity to the total amount of Wnt3a delivered under this condition. Consequently, this specific condition was adopted as the standard for all subsequent experiments unless otherwise mentioned. The strong linearity observed provides a basis for accurate quantification of bioactive Wnt3a in subsequent experiments based on the amount of protein delivered to the cells.

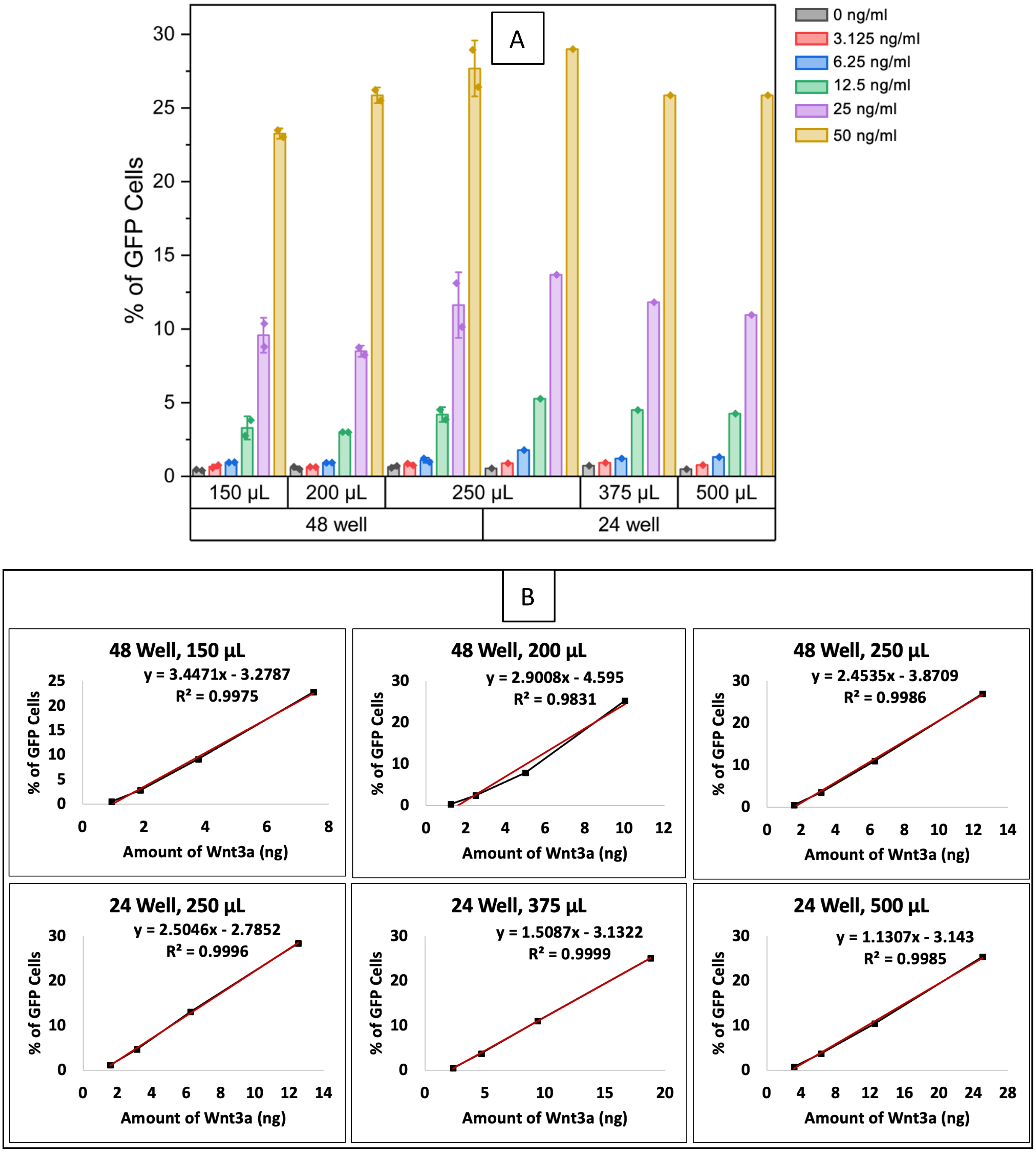

Figure 5.3: Optimization of Wnt3a bioactivity assay sensitivity using different well formats and volumes: (A) Dose-response of GFP-positive Wnt reporter cells to Wnt3a (0-50 ng/ml) across varying well formats (48-well: 150-250 µL; 24-well: 250-500 µL). (B) Linear regression of GFP-positive cells versus Wnt3a amount (ng) per well, showing the equations and R^2 values for each condition. Data represents mean ± SD (N=2)

5.2.3 Assessing Wnt3a stability and bioactivity under different buffer condition

To evaluate the stability and bioactivity of Wnt3a in the intended encapsulation and release buffer (20mM HEPES with 100mM NaCl, pH 7.4), GFP responses across different medium conditions were recorded. In the positive control condition (DMEM with FBS), which is typically used and known to support optimal GFP activity, Wnt3a elicited a robust response, reaching approximately 69.5% GFP-positive cells at the highest tested concentration (100 ng/ml), as expected (**Figure 5.4**). A similar trend was observed in DMEM without FBS, although the overall percentage of GFP-positive cells was slightly reduced compared to the FBS-supplemented media, peaking at approximately 48.8% at 100 ng/ml Wnt3a. Crucially, Wnt3a retained significant bioactivity when diluted in 20mM HEPES with 100mM NaCl (pH 7.4) buffer (**Figure 5.4**). Although the signalling response was generally lower than that of the DMEM-based media, a clear dose-response was still evident. At the highest Wnt3a concentration (100 ng/ml) in HEPES buffer, 43.2% of the reporter cells were GFP-positive, indicating that a substantial portion of the Wnt3a protein remained functional and capable of activating the Wnt/β-catenin pathway after being diluted in this buffer. Even at lower concentrations, Wnt3a in HEPES buffer induced a noticeable signalling response, suggesting reasonable stability across the tested concentration range. These findings indicate that the HEPES-based buffer, intended for Wnt3a encapsulation within the nanoparticle delivery system, does not abolish Wnt3a bioactivity, thus supporting its suitability for encapsulation within polymer-coated SPIONs.

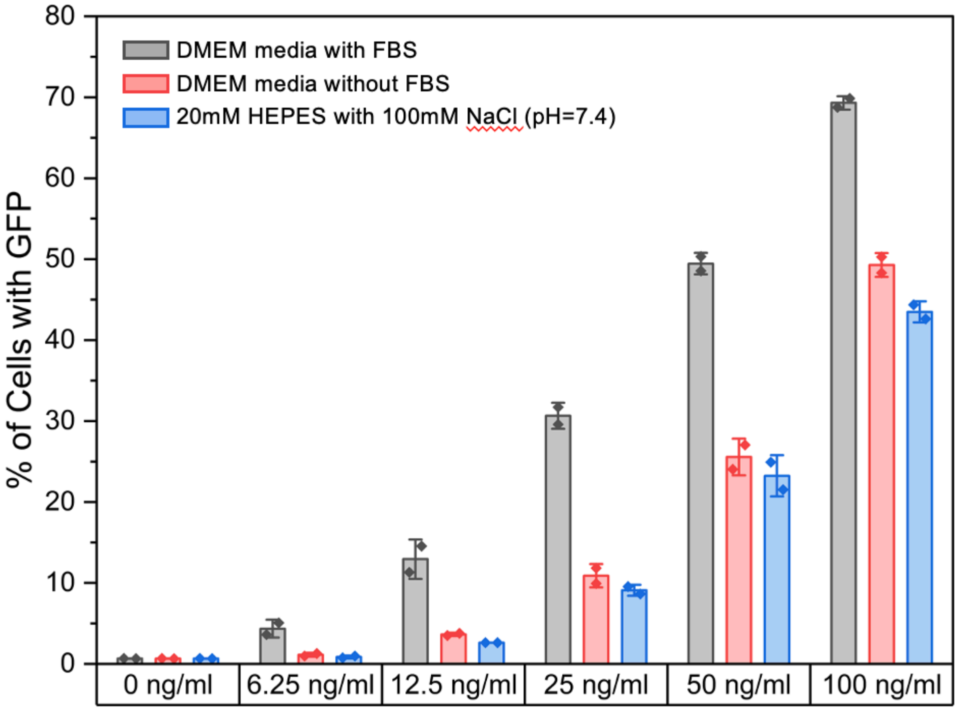

Figure 5.4: Bioactivity of Wnt3a standard in different medium conditions assessed by flow cytometry using the Wnt reporter cell line: A) Percentage of GFP-positive Wnt reporter cells after treatment with Wnt3a (0 to 100 ng/ml) in three different media. Data are presented as mean ± SD (N=2).

5.2.4 Testing Wnt3a stability during the temperature regime used for nanoparticle encapsulation and release

To assess the thermal stability of Wnt3a under conditions mimicking the temperature fluctuations during the simulated encapsulation and release process, the Wnt reporter cell line was treated with Wnt3a that had undergone specific temperature treatments. It is important to note that these experiments were conducted using Wnt3a protein alone, without the presence of nanoparticles. The temperature regimes which mimic the conditions used for protein encapsulation and release with the coated SPIONs, are depicted in the inset (**Figure 5.5**). They involve an initial incubation at 45 °C for 10 minutes, followed by a transition through 25 °C to a final release temperature of either 37 °C or 45 °C over a period of 1 hour. Wnt/β-catenin signalling activation, as measured by GFP expression in the Wnt reporter cell line, served as the readout for this comparison. (**Figure 5.5**). Untreated Wnt3a (grey bars) induced a clear dose-dependent response in the reporter cells. At 12.5 ng/ml, approximately 8.3 % of the cells were GFP-positive, whereas at 50 ng/ml, this percentage increased significantly to 34.2 %. In contrast, Wnt3a subjected to heat treatment mimicking a potential encapsulation and release cycle exhibited a complete loss of bioactivity, regardless of the final temperature used.

These results indicate that the temperature fluctuations associated with the simulated encapsulation and release conditions, possibly during the initial exposure to 45 °C for 10 min, severely compromise the bioactivity of Wnt3a, highlighting its inherent thermal instability under these conditions. This observation aligns with existing research demonstrating that Wnt3a can denature and lose its activity almost immediately in the absence of stabilizing factors [114]. We therefore explored the use of other signalling proteins that can activate Wnt signalling.

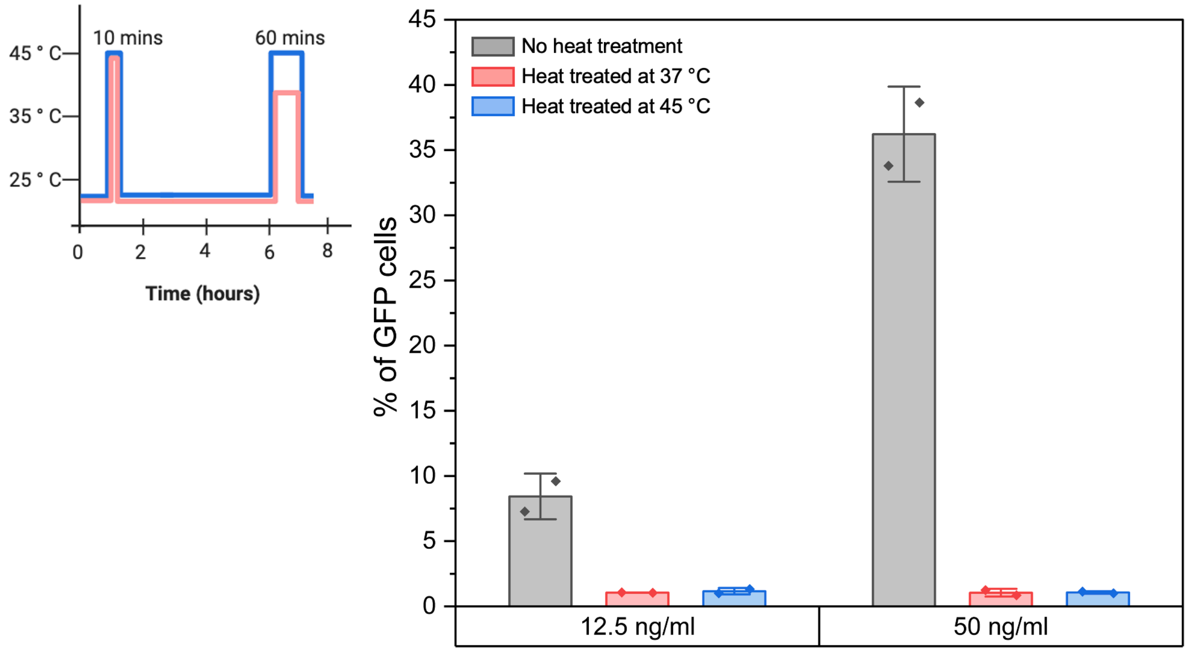

Figure 5.5: Impact of encapsulation/release treatment regime on Wnt3a bioactivity: Percentage of GFP-positive Wnt reporter cells after Wnt3a exposure to simulated temperature transitions. Inset details heat protocols (10 min at 45 °C, then 6 h cycling between 25 °C-37 °C/45 °C). Gray bars: untreated Wnt3a. Mean ± SD (N = 2).

5.2.5 Testing potential heat-resistant alternative protein for Wnt reporter cell line

Wnt signaling is regulated by a diverse array of proteins, including Wnt ligands and other agonists such as Norrin and R-spondin, all of which are capable of activating the pathway and play critical roles in early embryonic development as well as adult tissue homeostasis and regeneration. [170, 171]. Among the many ligands that activate the Wnt pathway, Norrin is unique. It's the only protein that forms a homodimer and possesses a cysteine knot motif, similar to BMP2 [172], a structural feature known to enhance thermal stability, making it a suitable candidate [173]. To assess the specificity of the Wnt reporter cell line, the response to increasing concentrations of Wnt3a (0–100 ng/ml) was compared with the response to Norrin (0–200 ng/ml) (**Figure 5.6**). Consistent with our previously described findings, Wnt3a treatment (red bars) again elicited a clear, dose-dependent increase in the percentage of GFP-positive cells, indicating activation of the canonical Wnt signalling pathway, reaching approximately 40 % at the highest concentration (200 ng/ml). Conversely, Norrin treatment (grey bars) did not result in increase in GFP-positive cells across all tested concentrations. These findings suggest that Wnt3a is the only suitable signalling molecule for our subsequent studies, since we already have an established reporter cell line for detecting its bioactivity. However, its susceptibility to thermal denaturation during encapsulation and release from polymer-coated SPIONs necessitates the incorporation of protective additives.

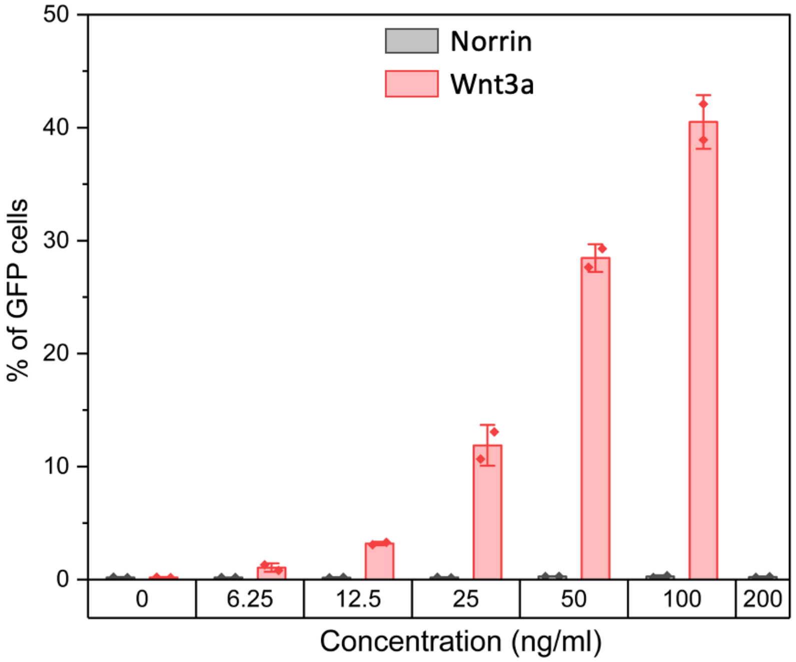

Figure 5.6: Comparative Wnt/β-catenin signalling activation by Wnt3a and Norrin: Percentage of GFP-positive reporter cells in response to Wnt3a (red) and Norrin (grey). Mean ± SD, (N=2).

5.2.6 Comparative thermal stability of Wnt3a with different thermos-protective additives

To mitigate the risk of Wnt3a denaturation, particularly during encapsulation and release processes that may involve temperature fluctuations, we incorporated thermo-protective additives, such as glycerol, in an attempt to make the Wnt3a protein more stable at higher temperature. Glycerol was primarily chosen because, as demonstrated for various other proteins, a 40 % concentration substantially increases their thermal denaturation temperature (T_d) compared to lower concentrations or the absence of glycerol. While higher glycerol concentrations might offer further increases in T_d for some proteins, 40 % often appeared to approach a plateau. A preliminary study showed that the addition of glycerol increased the denaturation temperature of proteins by approximately 6 °C, making it a promising candidate [174]. Sorbitol was also considered, as another study indicated that it could increase the protein denaturation temperature by approximately 10 °C [175]. Given the potential for temperature variation throughout the encapsulation and release conditions, we aimed to assess if these additives could help Wnt3a withstand the initial heating stages of the encapsulation process alone. Therefore, Wnt3a with the selected additives was heated at 45 °C for various time points to evaluate its stability under these initial heating conditions.

The thermal stability of Wnt3a in the presence of different additives was evaluated by measuring its bioactivity after heating at 45 °C for varying durations (**Figure 5.7** A). The activity of Wnt3a was normalised to that of the protein without any temperature stress and without any additives. HEPES buffer was chosen to stimulate the condition at which Wnt3a denatures most under heat stress, aligning with our earlier observation that denaturation would occur during encapsulation. In both HEPES buffer and 1M sorbitol, a noticeable loss of Wnt3a activity was observed within 10 min of heating at 45 °C. In stark contrast, Wnt3a in 40 % glycerol exhibited significantly enhanced thermal stability. Interestingly, the initial bioactivity of Wnt3a in 40 % glycerol (before heating was started) was already elevated compared to that of the non-heat-treated control, and after 60 min of heating at 45 °C, the activity remained considerably higher than that observed in 1M Sorbitol (**Figure 5.7** A).

This demonstrates that 40 % glycerol significantly enhanced Wnt3a's resistance to thermal denaturation at 45 °C. It is important to note that this assessment only involved heating to 45 °C, not the complete temperature profile of the encapsulation and release process. After establishing the protective effect of 40 % glycerol at this temperature, we investigated the efficacy of lower glycerol concentrations under identical heating conditions (**Figure 5.7** B). Wnt3a dissolved in 5 % and 15 % glycerol showed high bioactivity at 0 min of heating. However, upon heating to 45 °C, the bioactivity at both 5 % and 15 % glycerol rapidly declined, reaching near zero after just 15 min and remaining negligible at 30 and 60 min. In contrast, 30 % glycerol provided a noticeable improvement in thermal stability compared to the lower percentages, although its bioactivity also decreased to near zero after 60 min. These findings indicate that 30 % glycerol provides a temporary enhancement of Wnt3a's resistance to thermal denaturation at 45 °C compared to the rapid degradation observed at 5 % and 15 % glycerol. These findings underscore that glycerol, especially at a high concentration of 40 %, offers considerable protection against Wnt3a thermal inactivation at 45 °C, whereas 1M sorbitol and lower glycerol concentrations fail to provide comparable stabilization.

To thoroughly assess Wnt3a bioactivity in the presence of 40% glycerol, a complete temperature regime must be tested. Further investigation is specifically needed to determine the effect of glycerol on the LCST of polymer-coated SPIONs, as the LCST is known to change with altered in the presence of salt and agents like glycerol [176, 177]. While much of the existing research on this effect has concentrated on PNIPAM, it is crucial to evaluate the LCST directly in the presence of glycerol to determine any potential shift in the phase transition of the PNIPMAM coating. Understanding the effects of glycerol and temperature is crucial for optimizing the preliminary controlled delivery system by ensuring the bioactivity of Wnt3a is maintained**.**

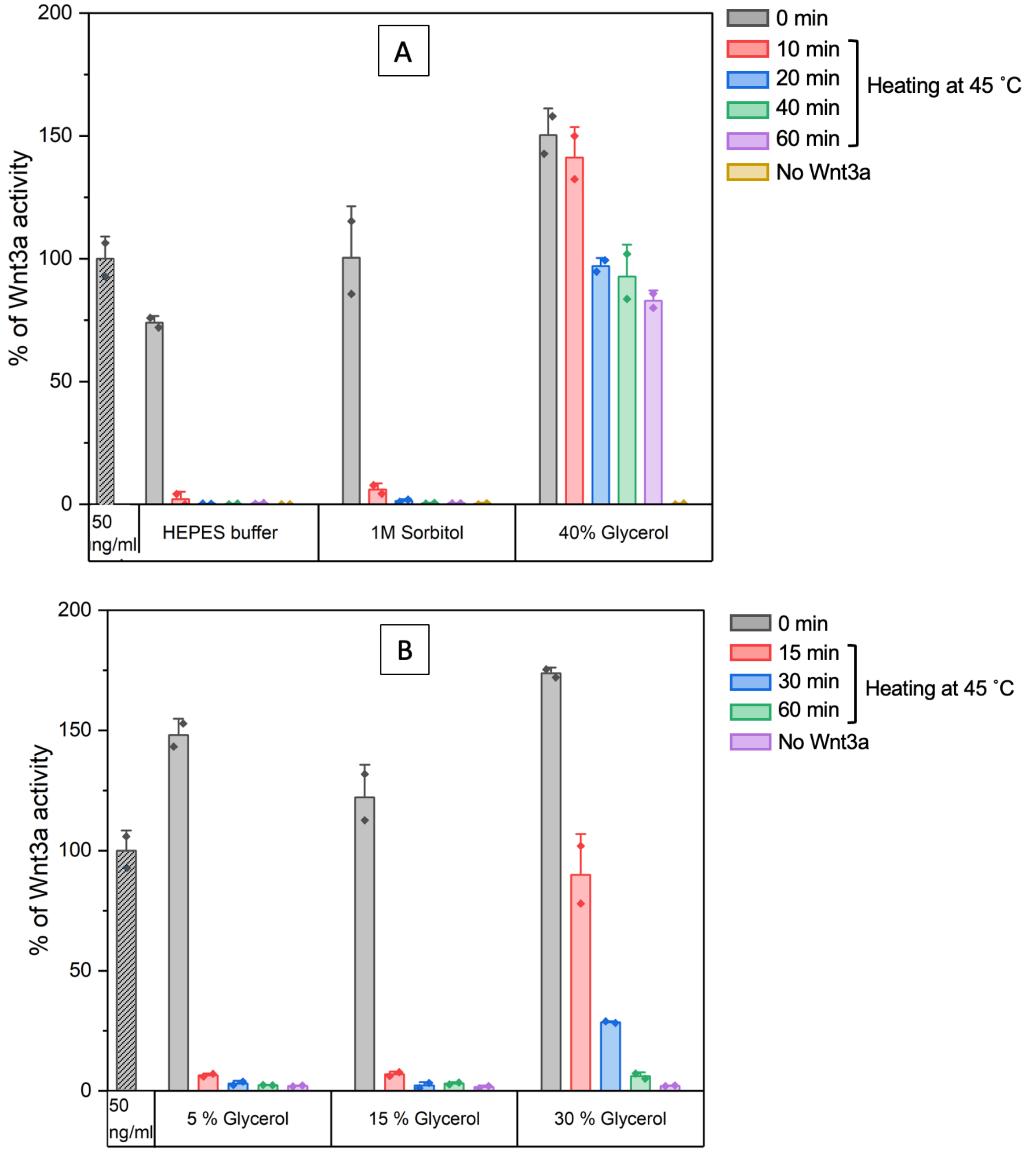

Figure 5.7: Effect of additives on Wnt3a thermal stability at 45 °C: Percentage Wnt3a activity of 50 ng/mL Wnt3a (normalised to untreated) after heating for the indicated time points. Hatched grey bar: non-heat-treated Wnt3a. (A) Stability in HEPES, 1M Sorbitol, and 40 % glycerol. (B) Stability in the presence of indicted glycerol concentrations. Coloured bars denote heated samples. Mean ± SD, (N=2).

5.2.7 Effect of glycerol concentration on the LCST of polymer-coated SPIONs

The influence of varying glycerol concentrations on the LCST behaviour of polymer-coated SPIONs was investigated by observing the precipitation of nanoparticles at different temperatures. Precipitation signifies that the temperature has exceeded the LCST, causing the polymer to become hydrophobic and the SPIONs to aggregate. As shown in result **chapter 1**, polymer coated SPIONs precipitate at the LCST of 45°C under normal physiological buffer conditions. The LCST of the polymer-coated SPIONs was found to be modulated by the concentration of glycerol in the solution. At 10 % glycerol, precipitation was not observed across the temperature range of 20–37 °C. However, precipitation occurred at 38 °C, suggesting that the LCST for the polymer-coated SPIONs in 10 % glycerol was slightly above 37 °C. Increasing the glycerol concentration to 20 % resulted in a significant decrease in LCST. Precipitation was observed at 30 °C, although no precipitation occurred at 20 and 25 °C. This indicates an LCST for the polymer-coated SPIONs in 20 % glycerol between 25 °C and 30 °C. A further increase in the glycerol concentration to 30 % resulted in a similar LCST range as that observed at 20 % glycerol. No precipitation was observed at 20 and 25 °C. The highest glycerol concentration tested (40 %) exhibited the lowest LCST. Precipitation was observed at 25 °C and all subsequent higher temperatures, whereas no precipitation occurred at 20 °C. This indicates that the LCST for polymer-coated SPIONs in 40 % glycerol was 25 °C or lower (**Table 5.1**).

These results demonstrate a clear inverse relationship between glycerol concentration and the LCST of the polymer-coated SPIONs. As the percentage of glycerol in the solution increased, the temperature at which the nanoparticles precipitated decreased, indicating a lowering of the polymer's LCST. This suggests that glycerol acts as a co-solvent that influences the polymer-water interactions, leading to a reduction in the temperature at which the polymer undergoes a phase transition and the SPIONs aggregate.

Given that glycerol affects the precipitation temperature and that the polymer-coated SPIONs were designed to remain stable above physiological temperature, even with a potential 10 % glycerol carryover from previous steps, and considering the observed denaturation of Wnt3a at 45 °C, we decided to move forward with release experiments at 38 °C. With the use of 10% glycerol this temperature potentially allowed us to investigate the encapsulation and release of Wnt3a using PNIPMAM-coated SPIONs, a condition that has not been previously explored. Furthermore, to assess potential Wnt3a stabilisation strategies, we investigated the different competitor proteins, as their presence could enhance Wnt3a stability without significantly affecting the precipitation temperature.

Temperature	20 °C	25 °C	30 °C	35 °C	37 °C	38 °C
10 % Glycerol	x	x	x	x	x	✓
20 % Glycerol	x	x	✓	✓	✓	✓
30 % Glycerol	x	x	✓	✓	✓	✓
40 % Glycerol	x	✓	✓	✓	✓	✓

✓ : Precipitated

x : Not precipitated

Table 5.1: Effect of glycerol concentration on polymer-coated SPIONs' LCST: Precipitation behaviour of polymer-coated SPIONs (✓: precipitated, x: not precipitated) at various temperatures (20-38 °C and glycerol concentrations (10-40 %).

5.2.8 Simulating encapsulation and release condition for Wnt3a in the presence of glycerol

In the previous section, glycerol's ability to act as a thermo-protector for Wnt3a was tested by heating the protein at 45°C for various durations. However, this did not simulate the complete encapsulation and release temperature regime.. In continuation of our assessment of potential Wnt3a stabilization strategies, and as an alternative approach, we investigated a system employing 40% glycerol during encapsulation, with subsequent washes and release conducted in pure FBS. The rationale for using FBS in the release phase stemmed from its high protein concentration [178], which we hypothesized could maintain Wnt3a bioactivity during temperature stress, leveraging the known principle that proteins are generally more stable in the presence of other proteins. This approach aimed to facilitate the removal of any residual glycerol during washing and potentially enable release at 45 °C if FBS [179] successfully maintained Wnt3a bioactivity at that elevated temperature. While 10% glycerol could also serve as a viable testing condition, this specific combined approach offered distinct advantages for evaluating Wnt3a stability.

To assess Wnt3a survival during encapsulation and release temperature regimes, the entire process was simulated with Wnt3a dissolved in 40 % glycerol and FBS in the absence of coated SPIONs. Following incubation that mimicked the temperature regime of encapsulation and release with 40 % glycerol, Wnt3a exhibited a gradual decrease in bioactivity when maintained at 45 °C. At 15 min, the remaining activity was approximately 66 %, which slightly decreased to approximately 64 % at 30 min and further to approximately 50 % at 60 min. However, Wnt3a subjected to simulated washes and release conditions without glycerol, in the presence of FBS, demonstrated a significantly more pronounced loss of bioactivity (~25% activity remaining) at the 0 min time point (before heating at 45 °C). After 15 min at 45 °C in FBS, Wnt3a activity plummeted to approximately 6 %. This minimal activity persisted at subsequent time points of 30 and 60 min. (**Figure 5.8**). These findings indicate that while the tested temperature regime negatively impacts Wnt3a bioactivity, the presence of 40 % glycerol during the simulated encapsulation phase appears to offer a substantially greater retention of its signalling capacity during the subsequent 45 °C release phase compared to conditions mimicking release in FBS. This suggests that 40 % glycerol may offer a protective effect during encapsulation, preserving Wnt3a integrity during incubations at elevated temperatures, whereas FBS appears unable to protect Wnt3a bioactivity under these conditions.

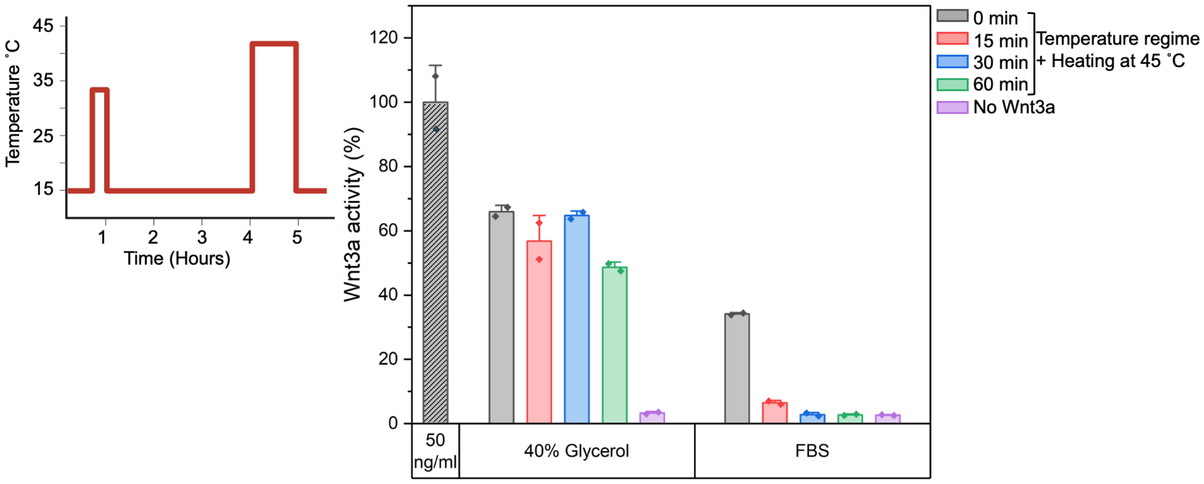

Figure 5.8: Wnt3a bioactivity following a simulated encapsulation and release temperature regime with 40 % Glycerol or FBS: Bar graph shows percentage of Wnt3a activity (50 ng/ml , activity normalised to unheated control) following temperature incubation (see inset) with 40 % glycerol or FBS. Hatched grey: unheated control. Mean ± SD, (N=2).

5.2.9 Testing the effect of temperature regimes on Wnt3a activity in the presence of competitor proteins

Given the lack of prior data on Wnt3a encapsulation and release using our delivery system and considering the potential for protein engineering to enhance stability, we explored alternative encapsulation and release temperature profiles owing to time constraints. Our strategy focused on utilising polymer-coated SPIONs with specific additives: 40 % glycerol during encapsulation and 10 % glycerol combined with 10 mg/ml of a competitor protein (apotransferrin, FBS, or RNaseB) for washing and release at 38 °C. This temperature was chosen because 10 % glycerol shifted the phase transition of the polymer-coated SPIONs to 38 °C. The strategy also called for the release profile at 38 °C to be compared with that at 37 °C to better understand release properties. We then assessed Wnt3a activity retention under these simulated encapsulation and release conditions without polymer-coated SPIONs. Following this treatment, Wnt3a incubated with apotransferrin retained approximately 50% of its bioactivity, indicating stability throughout the temperature regime and suggesting that apotransferrin, in combination with 10% glycerol, may be suitable for the encapsulation and release of Wnt3a from polymer-coated SPIONs.

Furthermore, when Wnt3a was incubated with FBS, it also demonstrated significant bioactivity retention, with approximately 90% activity remaining after 1 hour at 38 °, suggesting that FBS is highly effective in preserving Wnt3a activity at this temperature. This indicates that 10 % glycerol with FBS could also be suitable for washing and releasing Wnt3a without significant denaturation. Conversely, Wnt3a with RNase B demonstrated a substantial loss of bioactivity, decreasing to approximately 2 % after 15 min and remaining low. These results indicate that the choice of competitor protein significantly influences Wnt3a bioactivity following simulated encapsulation and release conditions at 38 °C (**Figure 5.9**). Although apotransferrin offered some preservation, FBS demonstrated a remarkable ability to maintain Wnt3a bioactivity. However, RNase B was detrimental. These findings suggest that FBS and apotransferrin, when combined with 10 % glycerol, could potentially serve as beneficial competitor proteins for maintaining Wnt3a stability and bioactivity during the washes and release process from the polymer-coated SPIONs. The observed activity retention indicates that significant Wnt3a denaturation did not occur due to the temperature or additives used in the simulated process. Therefore, if Wnt3a release is not observed in subsequent experiments, it is more likely due to a hindrance in the release mechanism rather than protein denaturation. Conversely, successful Wnt3a release was could be to the effective elution of the bioactive protein from SPIONs under these conditions.

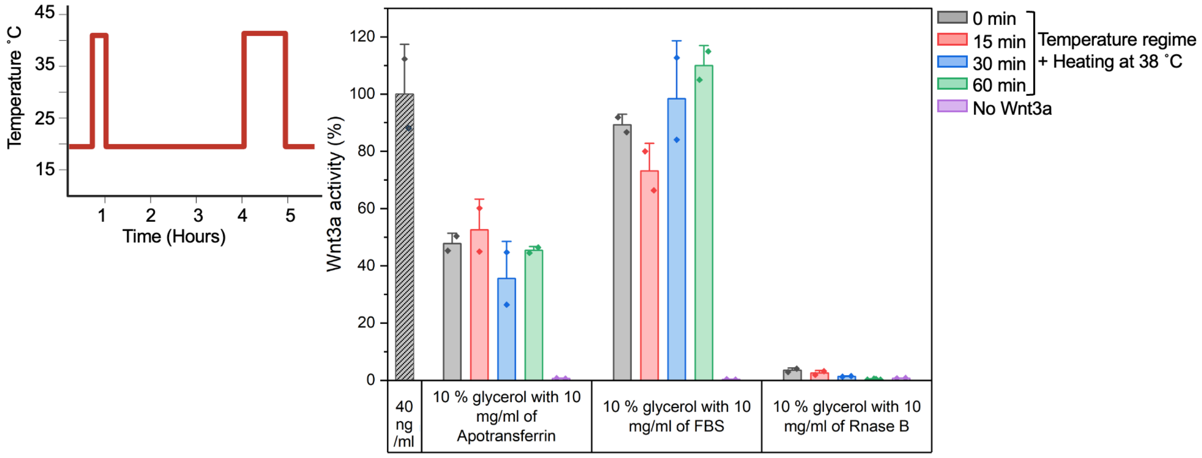

Figure 5.9: Wnt3a bioactivity (40 ng/ml) after simulated temperature regime during encapsulation/release at 38 °C with competitor proteins: hatched grey bar: unheated Wnt3a (40 ng/ml). Other bars: activity after temperature cyclin (inset) and subsequent 38°C incubation (15, 30, and 60 min) with 10 % glycerol and 10 mg/ml apotransferrin, FBS, or RNase. Grey bar (0 min): initial activity post-cycling. Purple bar: background. Mean ± SD,(N=2).

5.2.10 Using FBS with 10 % glycerol for releasing Wnt3a from polymer coated SPIONs

To translate our findings to our delivery system, we next evaluated the encapsulation of 1000 ng of Wnt3a onto polymer-coated SPIONs using 40% glycerol, and its subsequent release in the presence of 10% glycerol and FBS. Under these conditions, we then quantified the efficiency of Wnt3a loading and its subsequent release. Only a minimal amount was detected in the unloaded control sample (UL, 0.06%), indicating highly efficient binding to the nanoparticles. Following the washing (W1), 25.4 ng of Wnt3a was found associated with the SPIONs, corresponding to approximately 97% of the initial input, thereby confirming successful encapsulation. Subsequent washes with FBS and 10% glycerol efficiently removed loosely bound protein, as indicated by the progressive decrease in Wnt3a levels in the first (W2, 0.16 ng) and second (W3, 0.09 ng) washes. These results demonstrate that the encapsulation process successfully loaded the majority of Wnt3a (~97%). Subsequently, Wnt3a release was quantified at 37 °C and 38 °C. At 37 °C, the release was minimal, with only 0.25%, 0.31%, and 0.34% of the loaded Wnt3a released at 15, 30, and 60 minutes, respectively. Similarly, at 38 °C, release remained low, with 0.24%, 0.35%, and 0.46% released over the same time points (**Figure 5.10**).

These results indicate that although Wnt3a was successfully loaded onto the polymer-coated SPIONs, its release at both 37 °C and 38 °C was very limited under the tested conditions. While the washing steps effectively removed loosely bound Wnt3a, most of the protein remain strongly associated with the nanoparticles. As we already known that, based on the previous observation where FBS retained most of its activity during the stimulated temperature regime, even after 60 minutes above the polymer's transition point (**Figure 5.9**). This suggests a potential limitation in Wnt3a release efficiency in the presence of 10% glycerol and FBS.

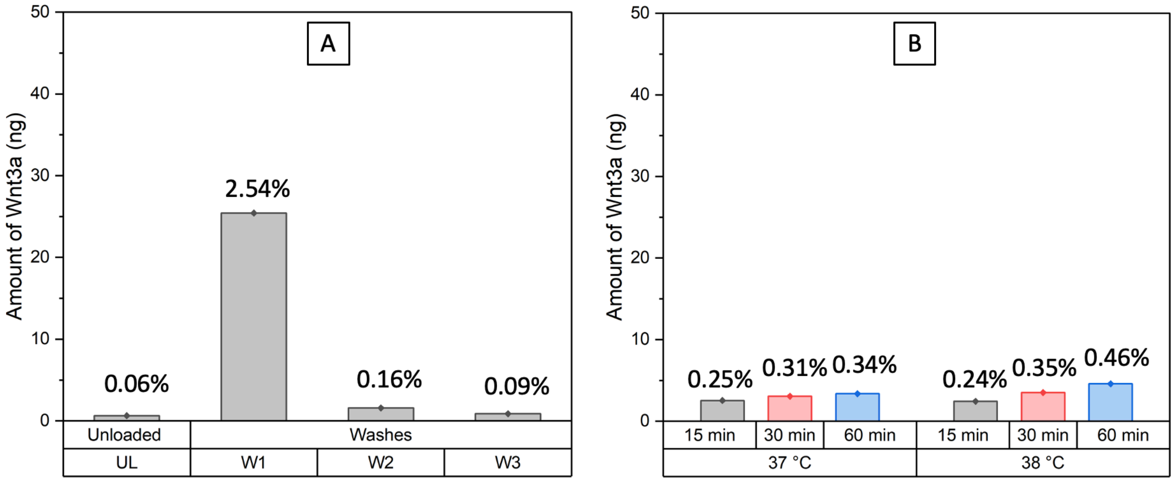

Figure 5.10: Wnt3a encapsulation at 40 % glycerol and washed/released with 10 % glycerol and 10 mg/ml FBS: (A) Wnt3a in 'Unloaded' sample and washes after encapsulation. (B) Wnt3a release at 37 °C and 38 °C in the presence of 10 % glycerol and FBS, Percentages are relative to the initial 1000 ng Wnt3a used for loading the coated SPIONs.

5.2.11 Apotransferrin mediated release of Wnt3a in polymer-coated SPIONs

The efficiency of Wnt3a association with polymer-coated SPIONs and its subsequent release at physiological (37 °C) and slightly elevated (38 °C) temperatures were quantitatively assessed in the presence of 10 mg/ml apotransferrin and 10 % glycerol in the washing and release buffers. The experiment was conducted in triplicate, with Panels A, B, and C representing individual experimental repeats.

In all three replicates, Wnt3a was successfully associated with the polymer-coated SPIONs following the loading procedure, with the percentage of total Wnt3a bound ranging from 1.14 % to 4.26 %. Subsequent washing steps (W2 and W3) effectively removed loosely bound Wnt3a, indicating approximately 95-98 % Wnt3a encapsulation efficiency.

The release profiles of Wnt3a from the washed SPIONs at 37 °C demonstrated consistently minimal release over the 60 min period. The percentage of initially loaded Wnt3a released at 37 °C remained below 1 % across all time points and replicates, indicating a limited release of Wnt3a at physiological temperature. In contrast, a comparatively higher release of Wnt3a was consistently observed at 38 °C across all three replicates (**Figure 5.11** A2, B2, and C2). While the overall release remained modest, a significant increase in Wnt3a release was evident at the 30-min, representing a notable, although temporary, enhancement in elution compared to the sustained low release at 37 °C.

However, beyond the 30-minute mark at 38 °C, the release percentage tended to plateau or even slightly decrease in all replicates, suggesting a nonlinear release. This might be due to the denaturation of the released Wnt3a in the presence of polymer-coated SPIONs when heated at 38 °C (**Figure 5.11**). These results indicate that the polymer-coated SPIONs system is capable of associating with Wnt3a and exhibiting a temperature-dependent release profile. The comparatively higher release observed at 38 °C than at 37°C, consistent across three independent experiments, suggests that the system's design, potentially linked to the polymer's LCST influenced by the 10 % glycerol, facilitates a modest release of the encapsulated Wnt3a at a slightly elevated temperature. However, the overall percentage of released Wnt3a remains low under these specific conditions with apotransferrin as the competitor protein, warranting further optimisation for more efficient and sustained protein delivery.

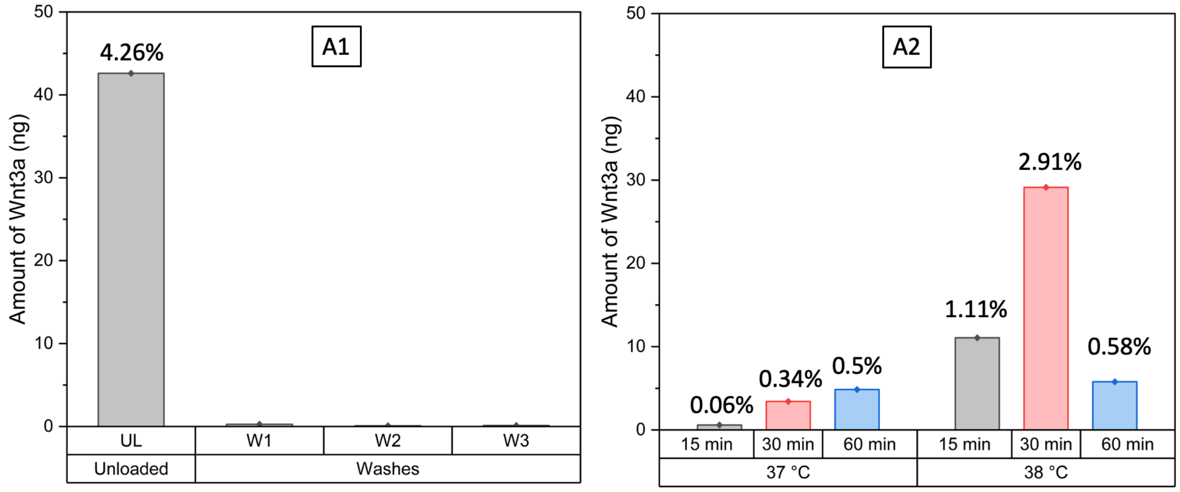

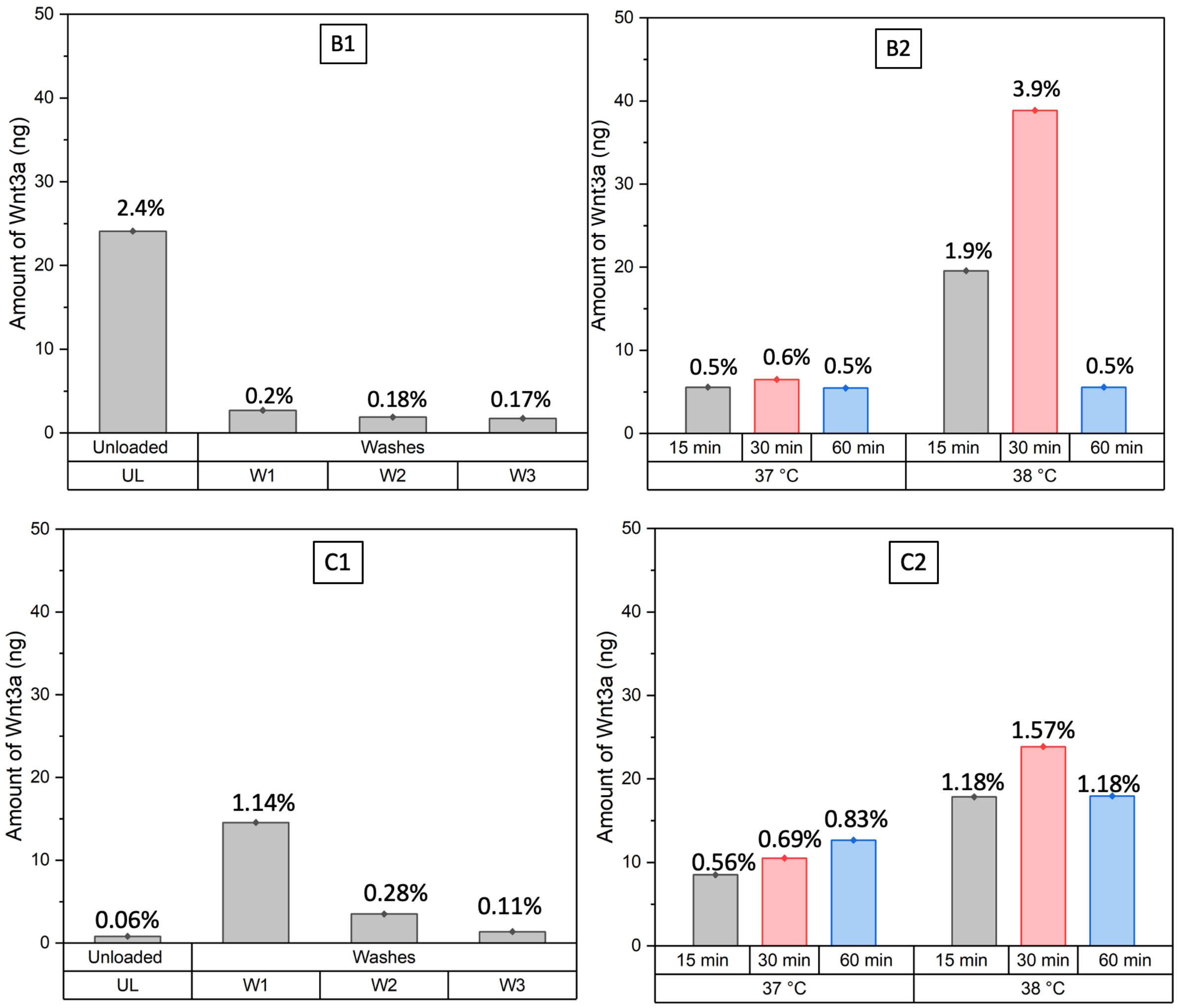

Figure 5.11: Wnt3a encapsulation at 40 % glycerol and wash/release with 10 % glycerol and 10 mg/mL apotransferrin: Panels A1, B1, and C1: Wnt3a (ng) not encapsulated into SPIONs: UL (Unloaded), W1, W2, W3 (washes). Panels A2, B2, and C2: Wnt3a (ng) released in the presence of 10 % glycerol 10mg/ml of apotransferrin. Percentages are relative to the initial 1000 ng Wnt3a used for loading the coated SPIONs.

5.3 Conclusion

This chapter investigates the use of PNIPMAM-coated SPIONs for the delivery of Wnt3a. When tested under the encapsulation and release temperature regime, Wnt3a was found to lose its activity immediately after heating to 45 °C, presenting a significant challenge for the development of the delivery system. As demonstrated by another study [174]. To address this, an alternative Wnt pathway activator was considered. Norrin was selected as a candidate. however, it failed to activate the reporter assay, rendering it unsuitable as a substitute. Since a functional reporter assay was already established, the focus shifted to enhancing the thermal stability of Wnt3a itself. Additives such as glycerol were evaluated, Various concentrations of glycerol were tested as a thermos stabilising agent [174], with 40% glycerol proving particularly effective in preserving Wnt3a activity following thermal exposure.

However, this high glycerol concentration affected the PNIPMAM-coated SPIONs LCST, thereby enabling the use of 10 % glycerol which shifted the LCST from 45 °C to approximately 38 °C. This specific shift provides a basis for triggered release slightly above physiological temperature, allowing preservation of Wnt3a activity. The addition of competitor proteins along with 10 % glycerol at temperatures below 45 °C further supported Wnt3a stability during simulated encapsulation and release temperature regimes, with apotransferrin and particularly FBS showing promising results in maintaining Wnt3a activity along with 10 % glycerol.

To maximize Wnt3a bioactivity encapsulation was done with 40 % glycerol and washing/releasing with a competitor protein in the presence of 10 % glycerol was adopted. Experiments using this system demonstrated the ability of SPIONs to associate with Wnt3a and exhibit, temperature-dependent release, with a significantly higher release observed at 38 °C than at 37 °C in the presence of apotransferrin, while offering less protection than FBS, showed discernible temperature-dependent release. Despite these advancements, the overall percentage of Wnt3a was ~3% of overall encapsulation, it was less compared to what was release by the previous study which used PNIPAM-coated SPIONs. Indicating the need for further optimisation of the release mechanism to achieve a more efficient and sustained delivery of bioactive Wnt3a for therapeutic applications.

Chapter 6

6. Discussion

This study set out to investigate PNIPMAM-coated SPIONs as a delivery system for osteoinducive proteins with potential application in bone regeneration. The approach was motivated by the need for reliable strategies to guide MSC behaviour through the provision of molecular cues that promote osteogenesis. While biomaterials capable of controlled release have shown promise in regenerative medicine, PNIPMAM-coated SPIONs offer additional advantages by combining the biocompatibility and magnetic properties of SPIONs with the thermo-responsive characteristics of PNIPMAM. Importantly, PNIPMAM's LCST above physiological temperature allows triggered release under mild hyperthermia, reducing premature leakage and preserving protein activity.

Within this context, BMP2 and Wnt3a were selected as model proteins due to their well-established roles in activating signalling pathways that stimulate MSC differentiation and bone formation. By evaluating the capacity of PNIPMAM-coated SPIONs to encapsulate and release these proteins in a bioactive form, the study aimed to establish a multifunctional platform for the controlled, localised delivery of osteogenic factors. The following discussion considers these findings in relation to current strategies for protein delivery, highlights the advantages and limitations of this approach, and outlines its potential implications for future bone tissue engineering applications.

6.1 PNIPMAM-coated SPIONs optimisation of ligand exchange

In this study I primarily focused on the optimisation and biocompatibility of NDA-functionalised PNIPMAM-coated SPIONs for potential applications in nanomedicine and regenerative medicine. A key advancement was the successful optimisation of the coating process, particularly through the inclusion of a centrifugation step following dialysis. This additional step proved critical for removing insoluble NDA and achieving a uniform NDA–PNIPMAM layer, as confirmed by thermal responsiveness, nano-DSF, and TGA analysis.

Challenges associated with the removal of excess NDA after functionalisation have been reported in previous studies. For example, in work involving NDA-functionalised PEG, multiple purification approaches were required to eliminate unbound NDA–PEG. Incomplete removal of excess ligand during ligand exchange was shown to cause nanoparticle instability [136]. In another study, SPIONs were first coated with NDA and subsequently grafted with a thermosensitive polypeptide, with the coating confirmed by dissolving the SPIONs. While effective, this method was lengthy and relied on an assumption of high reaction efficiency, which is not always realistic [137].

The NDA–PNIPMAM used in this study had a reaction efficiency of approximately 60%, which aligns with product recovery rates from the previous methods it was adapted from [18]. The additional post-synthesis purification step introduced here improved coating quality, as demonstrated by TGA. The TGA mass loss earlier was reported to be ~15% [18], while in the present study the mass loss is increased to 35% indicating a significant enhancement in nanoparticle coating. Having optimised the coating process, the next step was to evaluate the biological effects of these polymer-coated SPIONs, beginning with an assessment of their cellular interactions and biocompatibility.

6.2 Cellular interactions of PNIPMAM and PNIPMAM-coated SPIONs

The biocompatibility of the polymer and polymer-coated SPIONs was assessed by evaluating their toxicity towards the Y201 MSC cell line. Toxicity tests of polymer showed that for up to two days neither PNIPMAM nor NDA-PNIPMAM inhibited cell proliferation at concentrations ranging from 0.2 to 0.8 mg/mL. This agrees with the literature, which suggests that PNIPMAM is generally non-toxic. For example, one study reported that unloaded PNIPMAM-coated gold nanoparticles showed no cytotoxicity. Although, the cervical cancer cells were exposed for only 4 hours, the particles were subjected to radiofrequency for 3 minutes to heat the nanoparticles core for drug release, which did not adversely affect cell viability [49]. Similarly, another study using PTBMA-coated PNIPMAM core nanogels found no toxicity over a 24-hour period [47]. Collectively, these findings indicate that PNIPMAM itself is unlikely to be inherently toxic for short period of time, although further long-term studies are necessary to determine whether prolonged exposure could affect cell viability.

Toxicity of the PNIPMAM-coated SPIONs showed no significant effects at concentrations below 1 mg/ml but pronounced cytotoxicity at 2 mg/ml. Comparable findings have been reported in the literature. For example, one study using silica-coated SPIONs showed that concentrations above 100 µg/ml reduced the viability of human mesenchymal stem cells [138]. Similarly, dextran-coated SPIONs at 50 µg/mL induced toxic effects in human dermal fibroblasts, including cell death and inhibited proliferation, despite dextran’s generally non-toxic nature. In contrast, albumin-coated SPIONs enhanced proliferation at the same concentration [129]. Another study reported that human osteoblast-like cells treated with lauric acid-coated SPIONs at 10–1000 µg/mL for seven days showed reduced cell viability at all concentrations tested [180]. Taken together, these studies demonstrate that even at concentrations far lower than those used in this present work, SPIONs of various coatings have exhibited some level of toxicity. This supports the broader conclusion that nanoparticle toxicity is often dose-dependent, with potential mechanisms including oxidative stress, physical interactions with cellular components, or the release of iron ions, which catalyse the formation of reactive oxygen species (ROS) [181, 182]. Notably, a previous study in our laboratory using PNIPAM-coated SPIONs did not observe any toxic effects at 7 days. However, the work employed PicoGreen, which quantifies total DNA (from both live and dead cells) [17], whereas the present study used resazurin, which measures the metabolic activity of viable cells. As resazurin reflects active metabolism, it provides a more direct indication of cell viability under these experimental conditions.

Next I examined whether SPIONs and the polymer also affect osteogenic differentiation, using ALP activity as a functional readout. Polymer-coated SPIONs at concentrations up to 1 mg/mL did not significantly increase ALP production at any of the tested time points (days 3, 6, and 9), nor did they inhibit it. This outcome differs from several reports where specific concentrations of SPIONs stimulated ALP expression. For example, in MG-63 osteoblast-like cells, 50 µg/ml SPIONs addition increased ALP expression, whereas both 25 µg/ml and 100 µg/ml yielded lower levels compared to 50 µg/ml [183]. Another study showed that polyglucose-sorbitol-carboxymethyl ether-coated SPIONs enhanced ALP mRNA expression in precartilaginous stem cells at 200 µg/ml after 14 days, with no effect observed at 50 µg/ml or 100 µg/ml [184]. A key difference is that the SPION concentrations tested in the present study (0.25–1 mg/mL) are considerably higher than those reported in earlier studies (0.025–0.2 mg/mL). It is therefore possible that the tested concentrations were above the optimal range for ALP stimulation, as certain nanoparticles may exhibit a transient dose response where moderate concentrations stimulate osteogenic markers, but higher concentrations might fail to do so [183]. Additionally, differences in coating chemistry, cell type, and experimental duration could further contribute to the observed differences.

Interestingly, a couple of studies have shown that ALP activity increases in the presence of an external magnetic field. One such study reported that PLGA microspheres embedded with SPIONs, when combined with a magnetic field, effectively promoted osteogenic differentiation of bone marrow-derived MSC *in vitro*. However, the study did not assess how the microspheres alone (without the magnetic field) would influence ALP activity, which means the effect cannot be assumed to be universally applicable [185]. But, another study indicated that ALP activity increased in the presence of an external magnetic field (specifically a low-frequency pulsed electromagnetic field or LPEMF) when combined with SPION-labelled BMSCs. The study found that the ALP activity was significantly higher in SPION-labelled cells exposed to LPEMF compared to other groups [186]. These findings indicate that the combination of SPIONs and an external magnetic field could act as a potent physical stimulus to enhance osteogenic differentiation in stem cells. This suggests that SPIONs are not merely passive delivery vehicles but can actively influence cellular behaviour. While our research focused on temperature-triggered release of proteins, these studies highlight a potential synergistic effect where a magnetic field could not only trigger protein release from the nanoparticles but also provide an independent mechanical stimulus to the MSC. This presents a compelling avenue for future research to investigate a combined system and further optimize the therapeutic potential of this delivery platform.

While Y201 MSCs provided a consistent and well-characterised model for biocompatibility assessment. It would therefore be prudent to validate these findings in additional MSC lines, as well as in primary human cells, to confirm their broader applications.

6.3 Cell based assay to evaluate bioactivity and stability of BMP2 and Wnt3a

I used the PNIPMAM-coated SPION-based delivery system to encapsulate and characterise the release of bioactive BMP2 and Wnt3a. As the nanoparticles exhibited negligible toxicity at concentrations up to 1 mg/ml over a nine-day period, this study proceeded to test the system for its intended purpose the encapsulation and release of a therapeutic protein.

The Y201 cell line was initially selected as a model to measure BMP2 bioactivity. Western blot analysis indicated that BMP2 could activate its canonical signalling pathway by inducing immediate SMAD phosphorylation, Despite this initial signalling, Y201 cells showed no differentiation response, with insufficient ALP activity for quantification. This suggests that while BMP2 is capable of stimulating downstream signalling in Y201 cells, they are unable to consistently upregulate ALP expression. This observation is consistent with reports showing variable BMP2 responsiveness in human MSCs, with some donor-derived populations such as those from hip or femur samples exhibiting little or no ALP activity compared with rodent MSCs [92] similarly, another study also showed that human MSCs were not responsive to BMP2 [152]. However, there are also reports to show that BMP2 responsiveness in human MSCs either in the presence of osteogenic media or when pretreated with dexamethasone [66, 153], highlighting the complexity of MSC behaviour. Factors such as donor source, the *in vitro* environment, and the presence of other signalling proteins likely contribute to these differences, identifying the challenges of replicating *in vivo* conditions *in vitro*.

Other studies assessing BMP2 delivery have often relied on indirect measures of bioactivity rather than directly quantifying the amount of released bioactive BMP2. For example, BMP2 activity *in vitro* has frequently been inferred through RT-PCR analysis of osteogenic gene expression (ALP, osteocalcin, Runx2) and through ALP activity assays [97, 101]. In many cases, the primary focus was on demonstrating *in vivo* bone formation, with only limited *in vitro* validation, often using histology or immunoassays to assess tissue-level outcomes. Although these studies typically controlled the initial amount of BMP2 loaded into delivery systems, they rarely determined how much protein was actually released in an active form to confirm the release they often used methods like ELISA [9, 100] or Coomassie staining [97], were often used for quantification. Another study used radiolabelled BMP-2, specifically labelled with Iodine-125, to track its release and distribution both *in vitro* and *in vivo* [98]. Which measure total protein but cannot distinguish intact bioactive BMP2 from denatured protein.

In contrast, the present study emphasised quantifying the release of bioactive BMP2 using functional assays, thereby providing a more direct link between delivery and biological activity. Initial experiments utilized the Y201 human MSC line. However, these cells proved non-responsive to BMP2. This lack of responsiveness may be attributed from the donar from which the cells were isolated. A study demonstrated that the response of MSCs to BMP2 varies significantly depending on the age and source of the donor[187] Notably another study from the same lab also showed that removing serum from the medium and adding growth factors such as IGF-1 or insulin can increase the BMP2 response by up to 4-fold . While investigating whether Y201 responsiveness could be rescued with insulin/IGF-1 represents a valuable future direction to maintain a human-based model, the immediate goal of this work was to validate the encapsulation and release of bioactive BMP2 from PNIPMAM-coated SPIONs. Consequently, to ensure a robust detection of bioactivity, the study transitioned to a validated C2C12 cell-based ALP activity assay across a BMP2 concentration range of 6.25–200 ng/ml. However, it should be noted that these data represent a single-timepoint assessment of enzymatic activity. While this provides a comparative baseline for early osteogenic, there is an inherent risk of the reaction entering a saturation phase at high protein concentrations. To mitigate this in future studies, the adoption of kinetic monitoring (e.g., ALP/min) would provide a more robust quantification of initial reaction rates. This choice of C2C12 cells is supported by several studies showing that these cells, which are generally used for myoblastic differentiation are also highly responsive to BMP2 [80, 87, 94, 160]. Although many of these studies employed higher concentrations and longer incubation periods than those applied in the present study to induce measurable responses, the lower BMP2 concertation range was still effective to detect ALP activity and construct a dose response curve within a much shorter period compared to the one reported. The sensitivity of ALP activity from the C2C12 cells was advantageous for measuring low levels of BMP2 released from PNIPMAM-coated SPIONs. These cell lines also enabled validation that glycosylated BMP2 retained its bioactivity following the temperature regime of encapsulation and release, indicating enhanced thermal stability compared with its non-glycosylated counterpart. These findings are consistent with reports that BMP2 remains stable at elevated temperatures, with activity detectable even after exposure to 70 °C for 8 hours [188].

In contrast to the stability observed with BMP2, Wnt3a posed a major challenge, as its bioactivity was difficult to preserve, with experimental results demonstrating its sensitivity at temperature as low as 45 °C. This observation is consistent with previous reports showing that Wnt3a rapidly loses activity even at physiological temperature, with a half-life of less than one hour [114], a finding further supported by earlier work conducted in our laboratory [17]. This instability is likely caused by Wnt3a’s hydrophobic nature [189].

To overcome this, we initially investigated Norrin as a potential substitute owing to its cystine knot structure, which has been associated with enhanced thermostability in other proteins [73, 172]. However, the reporter cell lines were not responsive to Norrin. This was directly attributable to its obligate dependence on the transmembrane protein TSPAN12 for canonical Wnt pathway activation. The Wnt reporter cell line, developed from the Y201 cell line, is a homogeneous population that was later confirmed to lack TSPAN12 expression by RNAseq data. This absence of a crucial co-factor, therefore, serves as the primary limiting factor and consequently explains the observed lack of reporter response to Norrin in these cells.

Since using Norrin was not a suitable, the addition of additives was explored to make Wnt3a less temperature sensitive. Glycerol was found to significantly increase Wnt3a's thermal stability at 45 °C consistent with other studies that have demonstrated glycerol's ability to protect proteins from denaturation at temperatures above physiological range [174]. This is due to the fact that glycerol acts as a kosmotrope, stabilizing the native conformation of proteins through a mechanism known as preferential exclusion. In this process, glycerol molecules are sterically excluded from the protein’s immediate hydration shell, which energetically favors the more compact, folded state over the expanded, denatured state. Furthermore, glycerol serves as a water analog its hydroxyl groups form hydrogen bonds that mimic the stabilizing environment of water, while its higher viscosity reduces the molecular flexibility that typically leads to unfolding at elevated temperatures [174, 190].

However, this high glycerol concentration also altered the temperature-responsive behaviour of the PNIPMAM coating. My findings showed that increasing glycerol concentrations led to a decrease in the LCST of the PNIPMAM-coated SPIONs. Specifically, dissolving the nanoparticles in 10% glycerol shifted the LCST from 45 °C to approximately 38 °C. Similar trends have been reported for thermoresponsive polymers, where higher glycerol concentrations reduce LCST [191-193]. This highlights that glycerol concentration modulated the transition temperature of the nanoparticles, a property that can be strategically exploited to fine-tune release behaviour. Consequently, a strategy was adopted in which encapsulation was carried out with 40% glycerol, followed by washing and release in the presence of a competitor protein with 10% glycerol, in order to maximise Wnt3a bioactivity.

6.4 Protein interactions with the PNIPMAM-coated SPIONs

Following confirmation of stability, both BMP2 and Wnt3a were independently encapsulated using PNIPMAM-coated SPIONs. Both proteins showed an encapsulation efficiency of ~95%, further supporting the suitability of PNIPMAM-coated SPIONs as a protein delivery system. These findings are consistent with previous work in our laboratory using GFP, a protein of comparable size (~27 kDa), which achieved an encapsulation efficiency of ~90% with PNIPMAM-coated SPIONs [18]. Although the loading performance was similarly high for both growth factors, their behaviour during release and bioactivity preservation diverged significantly.

For BMP2, temperature-dependent release behaviour did not fully align with expectations, only minimal differences were observed between release at 37 °C and 45 °C in the presence of competitor proteins that have previously been reported to promote the release of larger proteins such as apotransferrin with IgG as competitor protein and for IgG in the presence of ovalbumin as competitor protein. To understand this, the role of the protein corona must also be considered. When nanoparticles are introduced into protein-rich environments, they rapidly acquire a corona composed of adsorbed proteins, which in turn alters their surface properties [150, 194]. In the present study, competitor proteins likely acted as a simplified model of corona formation. The reduced release of BMP2 in the presence of larger proteins suggests that corona formation with ovalbumin, IgG, or apotransferrin may have impeded BMP2 release, while RNase B, due to its smaller size, allowed greater release but both below and above the LCST. Interestingly, in the previous study GFP release was also found to be relatively low. However, with GFP, most of the protein appeared to be lost during the wash steps when ovalbumin was used as a competitor, a phenomenon not observed with BMP2. In contrast, the comparatively higher release of BMP2 in the presence of RNase B (15 kDa) further supports the notion that molecular size could play a role during the release. BMP2 (28 kDa) appears less easily displaced by larger competitor proteins such as ovalbumin (45 kDa), IgG (150 kDa), or apotransferrin (80 kDa).

For Wnt3a (42 kDa), RNase B did not survive the stability test, leaving open the question of whether RNase B could have promoted Wnt3a release. However Wnt3a release was observed in the presence of apotransferrin, despite apotransferrin being larger than Wnt3a. This suggests that factors beyond molecular size, such as structural variations or differences in glycosylation sites, may influence release behaviour. The exact mechanism underlying protein-specific release therefore remains unclear.

FBS was not tested as a competitor protein for BMP2 release, so its potential effect in this context remains unknown. However, for Wnt3a, FBS was highly effective in preserving bioactivity, most likely due to its complex protein composition and the presence of natural carrier proteins that stabilised Wnt3a during encapsulation and release [178]. Despite this protective effect, FBS did not substantially promote release from PNIPMAM-coated SPIONs. In contrast, a previous study using PNIPAM-coated SPIONs in the presence of FBS as a competitor protein mixture demonstrated Wnt3a release, as evidenced by increased MSC proliferation and Wnt reporter cell line activity [17]. Release of approximately 40 ng of Wnt3a was reported, but details on the exact amount initially loaded onto the PNIPAM-coated SPIONs or how much was lost during washing steps were not included [17]. But, in the present study, I was able to confirm Wnt3a loading even after the wash steps, with a retention efficiency of 97%. This loading efficiency is particularly important, as it ensures that the majority of the protein is available for controlled release and biological activity, reducing variability and enhancing reproducibility in downstream applications.

Experiments using apotransferrin as a competitor in combination with glycerol showed that SPIONs could encapsulate Wnt3a and support temperature-dependent release, with significantly higher release observed at 38 °C compared with 37 °C. Although apotransferrin was less effective than FBS in preserving Wnt3a bioactivity, it nonetheless enabled discernible temperature-responsive release of active protein. The only competitor protein examined for both growth factors was apotransferrin, which did not promote the release of BMP2 but did facilitate measurable release of Wnt3a. Despite the release the PNIPMAM-coated SPIONs the overall proportion of Wnt3a released remained comparable to, but slightly lower than previous studies, highlighting the need for further optimisation of the release mechanism to achieve more efficient and sustained delivery of bioactive Wnt3a for therapeutic applications. Several strategies may be considered to enhance the robustness and translational potential of this system. One rational approach is protein engineering of Wnt3a to increase its intrinsic stability. For instance, the introduction of cysteine is an approach that was successfully applied to other growth factors and has been shown to improve thermostability without impairing biological activity [195].

The precise release mechanism remains complex, as the phase transition behaviour of PNIPMAM in the presence of bound proteins is not yet fully understood. In the stimulated biological environments, proteins rapidly adsorb onto nanoparticle surfaces, creating a dynamic protein corona that can mask functionalisation and influence protein release. This means that encapsulated proteins are simultaneously interacting with the SPION core, the PNIPMAM coating, and corona proteins. Depending on their position on the nanoparticle surface, growth factors may be sterically hindered or displaced blocking or facilitating the release. The interplay between all components SPIONs, PNIPMAM, and competitor proteins likely accounts for the observed, as seen for BMP2 compared with ovalbumin, IgG and RNase B, or for Wnt3a in the presence of FBS.

For BMP2, future studies should focus on systematically investigating the effects of different competitor protein, combinations like using larger competitor proteins and RNase B for the release, to understand their influence on release behaviour. In addition, because the current assays rely solely on bioactivity-based measurements, they cannot distinguish between reduced release and protein denaturation. Incorporating techniques such as Western blot analysis would provide a more direct assessment of BMP2's structural integrity after encapsulation and release, ensuring that potential loss of bioactivity can be attributed to either denaturation or impaired release.

In the case of Wnt3a, this study confirmed the feasibility of using polymer-coated SPIONs for controlled delivery, while also highlighting key challenges related to protein stability and release efficiency. The findings advance our understanding of how stabilizing-additives and competitor proteins can be used to balance stabilisation and release, while also pointing towards future engineering strategies that will be essential for achieving efficient and sustained delivery of bioactive Wnt3a *in vivo*. The use of glycerol here served primarily as a proof of concept, demonstrating that the delivery system can support release under conditions where Wnt3a is stabilised, but it is not a viable approach for regenerative medicine applications.

Taken together, these findings highlight both the promise and the challenges of PNIPMAM-coated SPIONs as a growth factor delivery vehicle. While the encapsulation and preservation of BMP2 bioactivity were successfully demonstrated, and Wnt3a could also be stabilised and released under certain conditions, optimising controlled release will be essential for therapeutic translation. By addressing protein corona effects, size-dependent competition, and polymer–protein interactions, PNIPMAM-coated SPIONs could ultimately provide a versatile platform with advantages over conventional delivery systems. Such improvements may be particularly valuable in regenerative medicine, for example in bone repair, where sustained and localised release of proteins. Importantly, the insights gained here also provide a foundation for extending this delivery strategy to other signalling molecules relevant to osteogenesis.

6.5 Future work

Building on these insights, the next step is to address the current limitations of PNIPMAM-coated SPIONs for the delivery of growth factors. While specific aspects of future directions have been highlighted in earlier sections, this section provides a more integrated outlook. Addressing these challenges will require not only the optimisation of stabilisation strategies but also more robust characterisation of the system. Together, these considerations form the basis for the proposed future work, which aims to strengthen mechanistic understanding and improve the reliability of this delivery platform.

In particular, a more rigorous validation of the chemistry underlying NDA–PNIPMAM functionalisation and subsequent SPION coating is required to streamline the workflow. The main challenge lies in the removal of excess free NDA after the functionalisation step. At present, the most reliable strategy involves a lengthy, multi-step process of post-synthesis purification by ultracentrifugation, followed by dissolving the coated nanoparticles and performing heat tests to verify success. This makes the procedure time-consuming and inefficient, as incomplete removal of free NDA is often not detected until after the entire coating process is finished. Incorporating an intermediate, robust step to confirm the effective elimination of free NDA before proceeding to the final coating would not only ensure reaction fidelity but also significantly shorten the workflow and reduce experimental time.

Beyond removal of excess free NDA, the precise mechanism underlying protein release from PNIPMAM-coated SPIONs remains to be fully elucidated. It is not yet clear whether protein displacement is primarily governed by molecular size, electrostatic charge, or a combination of both. Systematic analysis of the zeta potential before encapsulation of BMP2/Wnt3a, after competitor protein introduction, and following thermal stimulation could provide valuable insights into these interactions. Such measurements may reveal whether shifts in particle or protein charge contribute to the observed release profiles.

It is also noteworthy that previous studies have reported enhanced release under magnetic triggering compared with bulk heating, with side-by-side comparisons confirming a higher proportion of protein released when localised magnetic actuation was employed [17, 18]. Given that the present work utilised bulk thermal stimulation, it would be particularly interesting to evaluate whether magnetic triggering could similarly enhance Wnt3a release from PNIPMAM-coated SPIONs, while simultaneously preserving bioactivity through spatially controlled heating.

From a translational perspective, testing the release system in a more biologically relevant context will be essential. For example, seeding cells in vessel-like constructs developed in a previous study [17] and triggering release magnetically within a sterile environment would more closely mimic *in vivo* conditions. As long as there is a reliable system that is available to detect the response of bioactive proteins, this platform could potentially be extended to other growth factors and signalling molecules beyond BMP2 and Wnt3a and other biological functions beyond osteogenesis.

Another promising avenue would be to explore the synthesis of a copolymer combining PNIPAM and PNIPMAM, or alternatively coating SPIONs with a defined ratio of the two polymers. By blending these thermoresponsive polymers, it may be possible to fine-tune the transition temperature to fall just above physiological levels, rather than relying solely on the higher transition temperature (typically >44 °C) observed for PNIPMAM alone. Such an approach could enable more precise control over triggered release under mild hyperthermic conditions (38–40 °C), thereby reducing the risk of protein denaturation and improving compatibility with *in vivo* applications.

Taken together, these strategies highlight clear directions for further optimisation and translation of PNIPMAM-coated SPIONs. By refining functionalisation, elucidating release mechanisms, and tailoring thermal responsiveness, this platform could be advanced towards a versatile and clinically relevant system for the controlled delivery of bioactive proteins.

Ultimately, *in vivo* studies will be essential to fully assess biocompatibility, evaluate biodistribution, and optimise dosing strategies for therapeutic use. Small animal models in particular would allow the investigation of immune responses and functional outcomes in bone regeneration, thereby bridging the gap between *in vitro* findings and clinical applicability. This step is especially important given the additional complexity introduced by systemic exposure, biodistribution, and clearance pathways *in vivo*. Studies have shown that nanoparticles can accumulate in organs such as the liver and spleen when administered above certain dose thresholds, leading to inflammatory responses. Striking a balance between delivering an adequate therapeutic payload (e.g., BMP2 or Wnt3a) and minimising cytotoxicity will therefore be a critical challenge for further development.

7. References

1. Ulbrich, K., et al., *Targeted Drug Delivery with Polymers and Magnetic Nanoparticles: Covalent and Noncovalent Approaches, Release Control, and Clinical Studies.* Chem Rev, 2016. **116**(9): p. 5338-431.
2. Zulauf, G.D., et al., *Targeting of systemically-delivered magnetic nanoparticle hyperthermia using a noninvasive, static, external magnetic field.* Proc SPIE Int Soc Opt Eng, 2013. **8584**: p. 85840C.
3. Rasekh, M., M.S. Arshad, and Z. Ahmad, *Advances in Drug Delivery Integrated with Regenerative Medicine: Innovations, Challenges, and Future Frontiers.* Pharmaceutics, 2025. **17**(4).
4. Blanco, E., H. Shen, and M. Ferrari, *Principles of nanoparticle design for overcoming biological barriers to drug delivery.* Nat Biotechnol, 2015. **33**(9): p. 941-51.
5. Nakamura, Y., et al., *Nanodrug Delivery: Is the Enhanced Permeability and Retention Effect Sufficient for Curing Cancer?* Bioconjug Chem, 2016. **27**(10): p. 2225-2238.
6. Golombek, S.K., et al., *Tumor targeting via EPR: Strategies to enhance patient responses.* Adv Drug Deliv Rev, 2018. **130**: p. 17-38.
7. Malaviya, A.N. and N.K. Mehra, *A fascinating story of the discovery & development of biologicals for use in clinical medicine.* Indian J Med Res, 2018. **148**(3): p. 263-278.
8. Yu, M., et al., *Nanotechnology for protein delivery: Overview and perspectives.* J Control Release, 2016. **240**: p. 24-37.
9. Zhu, Y., W. Zhuang, and H. Cheng, *Strategies to Enhance Protein Delivery.* Langmuir, 2025. **41**(10): p. 6457-6470.
10. Du, B., et al., *Glomerular barrier behaves as an atomically precise bandpass filter in a sub-nanometre regime.* Nat Nanotechnol, 2017. **12**(11): p. 1096-1102.
11. Khalil, B., E.J. Miller, and S.L. Lappin, *Physiology, Cellular Receptors*, in *StatPearls*. 2025: Treasure Island (FL) ineligible companies. Disclosure: Eric Miller declares no relevant financial relationships with ineligible companies. Disclosure: Sarah Lappin declares no relevant financial relationships with ineligible companies.
12. Schuster, J., et al., *In Vivo Stability of Therapeutic Proteins.* Pharm Res, 2020. **37**(2): p. 23.
13. Elisseeff, J., et al., *Controlled-release of IGF-I and TGF-beta1 in a photopolymerizing hydrogel for cartilage tissue engineering.* J Orthop Res, 2001. **19**(6): p. 1098-104.
14. Gupta, A.K. and S. Wells, *Surface-modified superparamagnetic nanoparticles for drug delivery: preparation, characterization, and cytotoxicity studies.* IEEE Trans Nanobioscience, 2004. **3**(1): p. 66-73.
15. Wang, Y.X., et al., *Recent advances in superparamagnetic iron oxide nanoparticles for cellular imaging and targeted therapy research.* Curr Pharm Des, 2013. **19**(37): p. 6575-93.
16. Zhao, N., et al., *pH-responsive carbohydrate polymer-based nanoparticles in cancer therapy.* Int J Biol Macromol, 2025. **306**(Pt 1): p. 141236.
17. Walker, M., et al., *Magnetically Triggered Release of Entrapped Bioactive Proteins from Thermally Responsive Polymer-Coated Iron Oxide Nanoparticles for Stem-Cell Proliferation.* ACS Appl Nano Mater, 2020. **3**(6): p. 5008-5013.
18. Sharma, R., et al., *Functional magnetic nanoparticles for protein delivery applications: understanding protein-nanoparticle interactions.* Nanoscale, 2024. **16**(5): p. 2466-2477.

19. Liu, D., et al., *Conjugation of paclitaxel to iron oxide nanoparticles for tumor imaging and therapy.* Nanoscale, 2012. **4**(7): p. 2306-10.
20. Pouliquen, D., et al., *Superparamagnetic iron oxide nanoparticles as a liver MRI contrast agent: contribution of microencapsulation to improved biodistribution.* Magn Reson Imaging, 1989. **7**(6): p. 619-27.
21. Barrow, M., et al., *SPIONs for cell labelling and tracking using MRI: magnetite or maghemite?* Biomater Sci, 2017. **6**(1): p. 101-106.
22. Chee, C.F., B.F. Leo, and C.W. Lai, *Superparamagnetic iron oxide nanoparticles for drug delivery*, in *Applications of Nanocomposite Materials in Drug Delivery*. 2018. p. 861-903.
23. Dulinska-Litewka, J., et al., *Superparamagnetic Iron Oxide Nanoparticles-Current and Prospective Medical Applications.* Materials (Basel), 2019. **12**(4).
24. Mornet, S., et al., *Magnetic nanoparticle design for medical diagnosis and therapy.* Journal of Materials Chemistry, 2004. **14**(14): p. 2161-2175.
25. Janko, C., et al., *Functionalized Superparamagnetic Iron Oxide Nanoparticles (SPIONs) as Platform for the Targeted Multimodal Tumor Therapy.* Front Oncol, 2019. **9**: p. 59.
26. Jordan, A., et al., *Inductive heating of ferrimagnetic particles and magnetic fluids: physical evaluation of their potential for hyperthermia.* Int J Hyperthermia, 1993. **9**(1): p. 51-68.
27. Johannsen, M., et al., *Magnetic nanoparticle hyperthermia for prostate cancer.* Int J Hyperthermia, 2010. **26**(8): p. 790-5.
28. Shevtsov, M.A., et al., *Superparamagnetic iron oxide nanoparticles conjugated with epidermal growth factor (SPION-EGF) for targeting brain tumors.* Int J Nanomedicine, 2014. **9**: p. 273-87.
29. Lubbe, A.S., et al., *Clinical experiences with magnetic drug targeting: a phase I study with 4'-epidoxorubicin in 14 patients with advanced solid tumors.* Cancer Res, 1996. **56**(20): p. 4686-93.
30. Lyer, S., et al., *Visualisation of tumour regression after local chemotherapy with magnetic nanoparticles - a pilot study.* Anticancer Res, 2010. **30**(5): p. 1553-7.
31. Johannsen, M., et al., *Clinical hyperthermia of prostate cancer using magnetic nanoparticles: presentation of a new interstitial technique.* Int J Hyperthermia, 2005. **21**(7): p. 637-47.
32. Alexiou, C., et al., *Locoregional cancer treatment with magnetic drug targeting.* Cancer Res, 2000. **60**(23): p. 6641-8.
33. Chertok, B., et al., *Iron oxide nanoparticles as a drug delivery vehicle for MRI monitored magnetic targeting of brain tumors.* Biomaterials, 2008. **29**(4): p. 487-96.
34. Calle, D., et al., *Magnetoliposomes loaded with poly-unsaturated fatty acids as novel theranostic anti-inflammatory formulations.* Theranostics, 2015. **5**(5): p. 489-503.
35. Torres, T.E., et al., *The relevance of Brownian relaxation as power absorption mechanism in Magnetic Hyperthermia.* Sci Rep, 2019. **9**(1): p. 3992.
36. Fortin, J.P., F. Gazeau, and C. Wilhelm, *Intracellular heating of living cells through Neel relaxation of magnetic nanoparticles.* Eur Biophys J, 2008. **37**(2): p. 223-8.
37. Gilchrist, R.K., et al., *Selective inductive heating of lymph nodes.* Ann Surg, 1957. **146**(4): p. 596-606.
38. Chertok, B., et al., *Glioma selectivity of magnetically targeted nanoparticles: a role of abnormal tumor hydrodynamics.* J Control Release, 2007. **122**(3): p. 315-23.

39. Rivera, D., et al., *Magnetic hyperthermia therapy enhances the chemoradiosensitivity of glioblastoma.* Sci Rep, 2025. **15**(1): p. 10532.
40. Rivera Gil, P., et al., *Nanopharmacy: Inorganic nanoscale devices as vectors and active compounds.* Pharmacol Res, 2010. **62**(2): p. 115-25.
41. Quoika, P.K., et al., *Thermosensitive Hydration of Four Acrylamide-Based Polymers in Coil and Globule Conformations.* J Phys Chem B, 2020. **124**(43): p. 9745-9756.
42. Dybal, J., M. Trchová, and P. Schmidt, *The role of water in structural changes of poly(N-isopropylacrylamide) and poly(N-isopropylmethacrylamide) studied by FTIR, Raman spectroscopy and quantum chemical calculations.* Vibrational Spectroscopy, 2009. **51**(1): p. 44-51.
43. Berndt, I., et al., *Influence of shell thickness and cross-link density on the structure of temperature-sensitive poly-N-isopropylacrylamide-poly-N-isopropylmethacrylamide core-shell microgels investigated by small-angle neutron scattering.* Langmuir, 2006. **22**(1): p. 459-68.
44. Doberenz, F., et al., *Thermoresponsive polymers and their biomedical application in tissue engineering – a review.* Journal of Materials Chemistry B, 2020. **8**(4): p. 607-628.
45. Fundueanu, G., et al., *Poly(N-isopropylacrylamide-co-N-isopropylmethacrylamide) Thermo-Responsive Microgels as Self-Regulated Drug Delivery System.* Macromolecular Chemistry and Physics, 2016. **217**(22): p. 2525-2533.
46. Ansari, M.J., et al., *Poly(N-isopropylacrylamide)-Based Hydrogels for Biomedical Applications: A Review of the State-of-the-Art.* Gels, 2022. **8**(7).
47. Peters, J.T., et al., *Synthesis and characterization of poly(N-isopropyl methacrylamide) core/shell nanogels for controlled release of chemotherapeutics.* Chemical Engineering Journal, 2018. **340**: p. 58-65.
48. Tang, Y., Y. Ding, and G. Zhang, *Role of methyl in the phase transition of poly(N-isopropylmethacrylamide).* J Phys Chem B, 2008. **112**(29): p. 8447-51.
49. Deshpande, S., et al., *Core-Shell Nanoparticles as an Efficient, Sustained, and Triggered Drug-Delivery System.* ACS Omega, 2017. **2**(10): p. 6455-6463.
50. Urošević, M.Z., et al., *Synthesis and characterization of poly(N-isopropylmethacrylamide-co-N-isopropylacrylamide) copolymers.* HEMIJSKA INDUSTRIJA (Chemical Industry), 2020/05/01. **74**(2).
51. Osyczka, A.M. and P.S. Leboy, *Bone morphogenetic protein regulation of early osteoblast genes in human marrow stromal cells is mediated by extracellular signal-regulated kinase and phosphatidylinositol 3-kinase signaling.* Endocrinology, 2005. **146**(8): p. 3428-37.
52. Frolke, J.P. and P. Patka, *Definition and classification of fracture non-unions.* Injury, 2007. **38 Suppl 2**: p. S19-22.
53. Disseldorp, D.J., et al., *Is Bone Grafting Necessary in the Treatment of Malunited Distal Radius Fractures?* J Wrist Surg, 2015. **4**(3): p. 207-13.
54. Cauley, J.A., et al., *Risk of mortality following clinical fractures.* Osteoporos Int, 2000. **11**(7): p. 556-61.
55. Lin, W., et al., *Mesenchymal stem cells homing to improve bone healing.* J Orthop Translat, 2017. **9**: p. 19-27.
56. Pittenger, M.F., et al., *Multilineage potential of adult human mesenchymal stem cells.* Science, 1999. **284**(5411): p. 143-7.

57. Hass, R., et al., *Different populations and sources of human mesenchymal stem cells (MSC): A comparison of adult and neonatal tissue-derived MSC.* Cell Commun Signal, 2011. **9**: p. 12.
58. Ferretti, C. and M. Mattioli-Belmonte, *Periosteum derived stem cells for regenerative medicine proposals: Boosting current knowledge.* World J Stem Cells, 2014. **6**(3): p. 266-77.
59. Wozney, J.M., *The bone morphogenetic protein family and osteogenesis.* Mol Reprod Dev, 1992. **32**(2): p. 160-7.
60. Linkhart, T.A., S. Mohan, and D.J. Baylink, *Growth factors for bone growth and repair: IGF, TGF beta and BMP.* Bone, 1996. **19**(1 Suppl): p. 1S-12S.
61. Fujioka-Kobayashi, M., et al., *Cholesteryl group- and acryloyl group-bearing pullulan nanogel to deliver BMP2 and FGF18 for bone tissue engineering.* Biomaterials, 2012. **33**(30): p. 7613-20.
62. Kim, J.H., et al., *Wnt signaling in bone formation and its therapeutic potential for bone diseases.* Ther Adv Musculoskelet Dis, 2013. **5**(1): p. 13-31.
63. Chen, G., C. Deng, and Y.P. Li, *TGF-beta and BMP signaling in osteoblast differentiation and bone formation.* Int J Biol Sci, 2012. **8**(2): p. 272-88.
64. Lee, K.S., et al., *Runx2 is a common target of transforming growth factor beta1 and bone morphogenetic protein 2, and cooperation between Runx2 and Smad5 induces osteoblast-specific gene expression in the pluripotent mesenchymal precursor cell line C2C12.* Mol Cell Biol, 2000. **20**(23): p. 8783-92.
65. Nakashima, K., et al., *The novel zinc finger-containing transcription factor osterix is required for osteoblast differentiation and bone formation.* Cell, 2002. **108**(1): p. 17-29.
66. Martini, F., et al., *Bone Morphogenetic Protein-2 Signaling in the Osteogenic Differentiation of Human Bone Marrow Mesenchymal Stem Cells Induced by Pulsed Electromagnetic Fields.* Int J Mol Sci, 2020. **21**(6).
67. Leucht, P., et al., *Wnt3a reestablishes osteogenic capacity to bone grafts from aged animals.* J Bone Joint Surg Am, 2013. **95**(14): p. 1278-88.
68. Urist, M.R., *Bone: formation by autoinduction.* Science, 1965. **150**(3698): p. 893-9.
69. Wozney, J.M., et al., *Novel regulators of bone formation: molecular clones and activities.* Science, 1988. **242**(4885): p. 1528-34.
70. Scheufler, C., W. Sebald, and M. Hulsmeyer, *Crystal structure of human bone morphogenetic protein-2 at 2.7 A resolution.* J Mol Biol, 1999. **287**(1): p. 103-15.
71. Yeung, B., T.J. Porter, and J.E. Vath, *Direct isoform analysis of high-mannose-containing glycoproteins by on-line capillary electrophoresis electrospray mass spectrometry.* Anal Chem, 1997. **69**(13): p. 2510-6.
72. Celeste, A.J., et al., *Identification of transforming growth factor beta family members present in bone-inductive protein purified from bovine bone.* Proc Natl Acad Sci U S A, 1990. **87**(24): p. 9843-7.
73. McDonald, N.Q. and W.A. Hendrickson, *A structural superfamily of growth factors containing a cystine knot motif.* Cell, 1993. **73**(3): p. 421-4.
74. Hang, Q., et al., *Asparagine-linked glycosylation of bone morphogenetic protein-2 is required for secretion and osteoblast differentiation.* Glycobiology, 2014. **24**(3): p. 292-304.

75. Liu, H., et al., *Activation of c-Jun NH(2)-terminal kinase 1 increases cellular responsiveness to BMP-2 and decreases binding of inhibitory Smad6 to the type 1 BMP receptor.* J Bone Miner Res, 2011. **26**(5): p. 1122-32.
76. Burkus, J.K., et al., *Clinical and radiographic outcomes of anterior lumbar interbody fusion using recombinant human bone morphogenetic protein-2.* Spine (Phila Pa 1976), 2002. **27**(21): p. 2396-408.
77. Halloran, D., H.W. Durbano, and A. Nohe, *Bone Morphogenetic Protein-2 in Development and Bone Homeostasis.* J Dev Biol, 2020. **8**(3).
78. Haid, R.W., Jr., et al., *Posterior lumbar interbody fusion using recombinant human bone morphogenetic protein type 2 with cylindrical interbody cages.* Spine J, 2004. **4**(5): p. 527-38; discussion 538-9.
79. Burkus, J.K., et al., *Is INFUSE bone graft superior to autograft bone? An integrated analysis of clinical trials using the LT-CAGE lumbar tapered fusion device.* J Spinal Disord Tech, 2003. **16**(2): p. 113-22.
80. Lee, K.B., et al., *Inflammatory characteristics of rhBMP-2 in vitro and in an in vivo rodent model.* Spine (Phila Pa 1976), 2011. **36**(3): p. E149-54.
81. Zara, J.N., et al., *High doses of bone morphogenetic protein 2 induce structurally abnormal bone and inflammation in vivo.* Tissue Eng Part A, 2011. **17**(9-10): p. 1389-99.
82. James, A.W., et al., *A Review of the Clinical Side Effects of Bone Morphogenetic Protein-2.* Tissue Eng Part B Rev, 2016. **22**(4): p. 284-97.
83. Cahill, K.S., et al., *Prevalence, complications, and hospital charges associated with use of bone-morphogenetic proteins in spinal fusion procedures.* JAMA, 2009. **302**(1): p. 58-66.
84. Choudhry, O.J., et al., *Bone morphogenetic protein-induced inflammatory cyst formation after lumbar fusion causing nerve root compression.* J Neurosurg Spine, 2012. **16**(3): p. 296-301.
85. Rihn, J.A., et al., *Complications associated with single-level transforaminal lumbar interbody fusion.* Spine J, 2009. **9**(8): p. 623-9.
86. Zhang, M., et al., *Increased plasma BMP-2 levels are associated with atherosclerosis burden and coronary calcification in type 2 diabetic patients.* Cardiovasc Diabetol, 2015. **14**: p. 64.
87. Gan, Q., et al., *Fabrication and evaluation of a BMP-2/dexamethasone co-loaded gelatin sponge scaffold for rapid bone regeneration.* Regen Biomater, 2022. **9**: p. rbac008.
88. Wagner, W., et al., *Aging and replicative senescence have related effects on human stem and progenitor cells.* PLoS One, 2009. **4**(6): p. e5846.
89. Wagner, W., et al., *Replicative senescence of mesenchymal stem cells: a continuous and organized process.* PLoS One, 2008. **3**(5): p. e2213.
90. Dominici, M., et al., *Minimal criteria for defining multipotent mesenchymal stromal cells. The International Society for Cellular Therapy position statement.* Cytotherapy, 2006. **8**(4): p. 315-7.
91. James, S., et al., *Multiparameter Analysis of Human Bone Marrow Stromal Cells Identifies Distinct Immunomodulatory and Differentiation-Competent Subtypes.* Stem Cell Reports, 2015. **4**(6): p. 1004-15.
92. Diefenderfer, D.L., et al., *BMP responsiveness in human mesenchymal stem cells.* Connect Tissue Res, 2003. **44 Suppl 1**: p. 305-11.

93. Chen, D., M. Zhao, and G.R. Mundy, *Bone morphogenetic proteins.* Growth Factors, 2004. **22**(4): p. 233-41.
94. Katagiri, T., et al., *Bone morphogenetic protein-2 converts the differentiation pathway of C2C12 myoblasts into the osteoblast lineage.* J Cell Biol, 1994. **127**(6 Pt 1): p. 1755-66.
95. Akiyama, S., et al., *Constitutively active BMP type I receptors transduce BMP-2 signals without the ligand in C2C12 myoblasts.* Exp Cell Res, 1997. **235**(2): p. 362-9.
96. Kang, M., et al., *Cell-permeable bone morphogenetic protein 2 facilitates bone regeneration by promoting osteogenesis.* Mater Today Bio, 2024. **25**: p. 100983.
97. Park, K.H., et al., *Bone morphogenic protein-2 (BMP-2) loaded nanoparticles mixed with human mesenchymal stem cell in fibrin hydrogel for bone tissue engineering.* J Biosci Bioeng, 2009. **108**(6): p. 530-7.
98. Kempen, D.H., et al., *Retention of in vitro and in vivo BMP-2 bioactivities in sustained delivery vehicles for bone tissue engineering.* Biomaterials, 2008. **29**(22): p. 3245-52.
99. Vantucci, C.E., et al., *BMP-2 delivery strategy modulates local bone regeneration and systemic immune responses to complex extremity trauma.* Biomater Sci, 2021. **9**(5): p. 1668-1682.
100. Vallmajo-Martin, Q., et al., *Enhanced bone regeneration in rat calvarial defects through BMP2 release from engineered poly(ethylene glycol) hydrogels.* Sci Rep, 2024. **14**(1): p. 4916.
101. Chen, X., et al., *Enhanced bone regeneration via spatiotemporal and controlled delivery of a genetically engineered BMP-2 in a composite Hydrogel.* Biomaterials, 2021. **277**: p. 121117.
102. Miller, J.R., *The Wnts.* Genome Biol, 2002. **3**(1): p. REVIEWS3001.
103. Willert, K., et al., *Wnt proteins are lipid-modified and can act as stem cell growth factors.* Nature, 2003. **423**(6938): p. 448-52.
104. Kim, J.B., et al., *Bone regeneration is regulated by wnt signaling.* J Bone Miner Res, 2007. **22**(12): p. 1913-23.
105. Gordon, M.D. and R. Nusse, *Wnt signaling: multiple pathways, multiple receptors, and multiple transcription factors.* J Biol Chem, 2006. **281**(32): p. 22429-33.
106. Wang, P., et al., *YAP/TEAD1 and beta-catenin/LEF1 synergistically induce estrogen receptor alpha to promote osteogenic differentiation of bone marrow stromal cells.* MedComm (2020), 2023. **4**(3): p. e246.
107. Aida, Y., H. Kurihara, and K. Kato, *Wnt3a promotes differentiation of human bone marrow-derived mesenchymal stem cells into cementoblast-like cells.* In Vitro Cell Dev Biol Anim, 2018. **54**(6): p. 468-476.
108. Ross, S.E., et al., *Inhibition of adipogenesis by Wnt signaling.* Science, 2000. **289**(5481): p. 950-3.
109. Gao, Y., et al., *Progress of Wnt Signaling Pathway in Osteoporosis.* Biomolecules, 2023. **13**(3).
110. Jullien, N., et al., *Downregulation of ErbB3 by Wnt3a contributes to wnt-induced osteoblast differentiation in mesenchymal cells.* J Cell Biochem, 2012. **113**(6): p. 2047-56.
111. Wagner, J.M., et al., *Local Wnt3a treatment restores bone regeneration in large osseous defects after surgical debridement of osteomyelitis.* J Mol Med (Berl), 2020. **98**(6): p. 897-906.

112. Jackson, A., et al., *Gene array analysis of Wnt-regulated genes in C3H10T1/2 cells.* Bone, 2005. **36**(4): p. 585-98.
113. Li, X., et al., *Wnt3a involved in the mechanical loading on improvement of bone remodeling and angiogenesis in a postmenopausal osteoporosis mouse model.* FASEB J, 2019. **33**(8): p. 8913-8924.
114. Dhamdhere, G.R., et al., *Drugging a stem cell compartment using Wnt3a protein as a therapeutic.* PLoS One, 2014. **9**(1): p. e83650.
115. Reeves, J., et al., *Rejuvenating aged osteoprogenitors for bone repair.* Elife, 2024. **13**.
116. Moschouris, P., et al., *Effect of Wnt3a delivery on early healing events during guided bone regeneration.* Clin Oral Implants Res, 2017. **28**(3): p. 283-290.
117. Janeczek, A.A., et al., *PEGylated liposomes associate with Wnt3A protein and expand putative stem cells in human bone marrow populations.* Nanomedicine (Lond), 2017. **12**(8): p. 845-863.
118. Mitchell, M.J., et al., *Engineering precision nanoparticles for drug delivery.* Nat Rev Drug Discov, 2021. **20**(2): p. 101-124.
119. Zhang, C., J. Fan, and L. Wu, *Application of nanomaterials in precision treatment of lung cancer.* iScience, 2025. **28**(1): p. 111704.
120. Nel, A.E., et al., *Understanding biophysicochemical interactions at the nano-bio interface.* Nat Mater, 2009. **8**(7): p. 543-57.
121. Kyriakides, T.R., et al., *Biocompatibility of nanomaterials and their immunological properties.* Biomed Mater, 2021. **16**(4).
122. Tillotson, M., N. Logan, and P. Brett, *Osteogenic stem cell selection for repair and regeneration.* Bone Rep, 2016. **5**: p. 22-32.
123. Cheng, K., et al., *Magnetic antibody-linked nanomatchmakers for therapeutic cell targeting.* Nat Commun, 2014. **5**: p. 4880.
124. Kim, J., Y.M. Kim, and S.C. Song, *One-Step Preparation of an Injectable Hydrogel Scaffold System Capable of Sequential Dual-Growth Factor Release to Maximize Bone Regeneration.* Adv Healthc Mater, 2023. **12**(4): p. e2202401.
125. DeConde, A.S., et al., *Bone morphogenetic protein-2-impregnated biomimetic scaffolds successfully induce bone healing in a marginal mandibular defect.* Laryngoscope, 2013. **123**(5): p. 1149-55.
126. Wang, P., et al., *Controlled Growth Factor Release in 3D-Printed Hydrogels.* Adv Healthc Mater, 2020. **9**(15): p. e1900977.
127. Mohammadi-Samani, S., et al., *Preparation and assessment of chitosan-coated superparamagnetic Fe3O4 nanoparticles for controlled delivery of methotrexate.* Res Pharm Sci, 2013. **8**(1): p. 25-33.
128. Yu, M. and J. Zheng, *Clearance Pathways and Tumor Targeting of Imaging Nanoparticles.* ACS Nano, 2015. **9**(7): p. 6655-74.
129. Berry, C.C., et al., *Dextran and albumin derivatised iron oxide nanoparticles: influence on fibroblasts in vitro.* Biomaterials, 2003. **24**(25): p. 4551-7.
130. Gaur, U., et al., *Biodistribution of fluoresceinated dextran using novel nanoparticles evading reticuloendothelial system.* Int J Pharm, 2000. **202**(1-2): p. 1-10.
131. Wahajuddin and Arora, *Superparamagnetic iron oxide nanoparticles: magnetic nanoplatforms as drug carriers.* International Journal of Nanomedicine, 2012: p. 3445.
132. Kalambur, V.S., E.K. Longmire, and J.C. Bischof, *Cellular level loading and heating of superparamagnetic iron oxide nanoparticles.* Langmuir, 2007. **23**(24): p. 12329-36.

133. Mulens-Arias, V., et al., *Polyethylenimine-coated superparamagnetic iron oxide nanoparticles impair in vitro and in vivo angiogenesis.* Nanomedicine, 2019. **21**: p. 102063.

134. Hoang Thi, T.T., et al., *Functional Magnetic Core-Shell System-Based Iron Oxide Nanoparticle Coated with Biocompatible Copolymer for Anticancer Drug Delivery.* Pharmaceutics, 2019. **11**(3).

135. Purushotham, S., et al., *Thermoresponsive core-shell magnetic nanoparticles for combined modalities of cancer therapy.* Nanotechnology, 2009. **20**(30): p. 305101.

136. Lassenberger, A., et al., *Evaluation of High-Yield Purification Methods on Monodisperse PEG-Grafted Iron Oxide Nanoparticles.* Langmuir, 2016. **32**(17): p. 4259-69.

137. *Thermoresponsive Polypeptoid-Coated Superparamagnetic Iron Oxide Nanoparticles by Surface-Initiated Polymerization.* Macromolecular Chemistry and Physics, 2017. **218**(13).

138. Harrison, R.P., et al., *Intracellular processing of silica-coated superparamagnetic iron nanoparticles in human mesenchymal stem cells.* RSC Adv, 2019. **9**(6): p. 3176-3184.

139. Poniatowski, L.A., et al., *Transforming growth factor Beta family: insight into the role of growth factors in regulation of fracture healing biology and potential clinical applications.* Mediators Inflamm, 2015. **2015**: p. 137823.

140. Sanchez-Duffhues, G., et al., *Bone morphogenetic protein receptors: Structure, function and targeting by selective small molecule kinase inhibitors.* Bone, 2020. **138**: p. 115472.

141. Stottmann, R.W. and J. Klingensmith, *Bone morphogenetic protein signaling is required in the dorsal neural folds before neurulation for the induction of spinal neural crest cells and dorsal neurons.* Dev Dyn, 2011. **240**(4): p. 755-65.

142. Li, R.H. and J.M. Wozney, *Delivering on the promise of bone morphogenetic proteins.* Trends Biotechnol, 2001. **19**(7): p. 255-65.

143. Howard, M.T., et al., *Sustained release of BMP-2 using self-assembled layer-by-layer film-coated implants enhances bone regeneration over burst release.* Biomaterials, 2022. **288**: p. 121721.

144. Antebi, Y.E., et al., *Combinatorial Signal Perception in the BMP Pathway.* Cell, 2017. **170**(6): p. 1184-1196 e24.

145. Reddi, A.H., *Bone and cartilage differentiation.* Curr Opin Genet Dev, 1994. **4**(5): p. 737-44.

146. Nohe, A., et al., *The mode of bone morphogenetic protein (BMP) receptor oligomerization determines different BMP-2 signaling pathways.* J Biol Chem, 2002. **277**(7): p. 5330-8.

147. Rui, Y.F., et al., *Higher BMP receptor expression and BMP-2-induced osteogenic differentiation in tendon-derived stem cells compared with bone-marrow-derived mesenchymal stem cells.* Int Orthop, 2012. **36**(5): p. 1099-107.

148. Moreno-Miralles, I., J.C. Schisler, and C. Patterson, *New insights into bone morphogenetic protein signaling: focus on angiogenesis.* Curr Opin Hematol, 2009. **16**(3): p. 195-201.

149. Ma, L., et al., *Bmp2 is essential for cardiac cushion epithelial-mesenchymal transition and myocardial patterning.* Development, 2005. **132**(24): p. 5601-11.

150. Cedervall, T., et al., *Understanding the nanoparticle-protein corona using methods to quantify exchange rates and affinities of proteins for nanoparticles.* Proc Natl Acad Sci U S A, 2007. **104**(7): p. 2050-5.
151. He, M., X. Zhou, and X. Wang, *Glycosylation: mechanisms, biological functions and clinical implications.* Signal Transduct Target Ther, 2024. **9**(1): p. 194.
152. Diefenderfer, D.L., et al., *Regulation of BMP-induced transcription in cultured human bone marrow stromal cells.* J Bone Joint Surg Am, 2003. **85-A Suppl 3**: p. 19-28.
153. Osyczka, A.M., et al., *Different effects of BMP-2 on marrow stromal cells from human and rat bone.* Cells Tissues Organs, 2004. **176**(1-3): p. 109-19.
154. Kopf, J., et al., *BMP2 and mechanical loading cooperatively regulate immediate early signalling events in the BMP pathway.* BMC Biol, 2012. **10**: p. 37.
155. Nakamura, A., et al., *Osteoclast inhibitory lectin (OCIL) inhibits osteoblast differentiation and function in vitro.* Bone, 2007. **40**(2): p. 305-15.
156. Tare, R.S., et al., *Pleiotrophin/Osteoblast-stimulating factor 1: dissecting its diverse functions in bone formation.* J Bone Miner Res, 2002. **17**(11): p. 2009-20.
157. Hwang, P.W. and J.A. Horton, *Variable osteogenic performance of MC3T3-E1 subclones impacts their utility as models of osteoblast biology.* Sci Rep, 2019. **9**(1): p. 8299.
158. Huang, P., et al., *BMP-2 induces EMT and breast cancer stemness through Rb and CD44.* Cell Death Discov, 2017. **3**: p. 17039.
159. Sangadala, S., et al., *FK506 Induces Ligand-Independent Activation of the Bone Morphogenetic Protein Pathway and Osteogenesis.* Int J Mol Sci, 2019. **20**(8).
160. Sakurai, T., et al., *Radiation-induced reduction of osteoblast differentiation in C2C12 cells.* J Radiat Res, 2007. **48**(6): p. 515-21.
161. Quaas, B., et al., *Stability and Biological Activity of E. coli Derived Soluble and Precipitated Bone Morphogenetic Protein-2.* Pharmaceutical Research 2019 36:12, 2019-11-20. **36**(12).
162. *Protein Binding on the Surface of Magnetic Nanoparticles.* Particle & Particle Systems Characterization, 2019. **36**(8).
163. Fradkin, L.G., J.N. Noordermeer, and R. Nusse, *The Drosophila Wnt protein DWnt-3 is a secreted glycoprotein localized on the axon tracts of the embryonic CNS.* Dev Biol, 1995. **168**(1): p. 202-13.
164. Steinhart, Z. and S. Angers, *Wnt signaling in development and tissue homeostasis.* Development, 2018. **145**(11).
165. Miao, Y., et al., *Next-Generation Surrogate Wnts Support Organoid Growth and Deconvolute Frizzled Pleiotropy In Vivo.* Cell Stem Cell, 2020. **27**(5): p. 840-851 e6.
166. Nazemidashtarjandi, S., et al., *Near-infrared light-responsive hydrogels for on-demand dual delivery of proangiogenic growth factors.* Acta Biomater, 2024. **183**: p. 61-73.
167. Carenza, E., et al., *Encapsulation of VEGF(165) into magnetic PLGA nanocapsules for potential local delivery and bioactivity in human brain endothelial cells.* J Mater Chem B, 2015. **3**(12): p. 2538-2544.
168. Mok, H. and M. Zhang, *Superparamagnetic iron oxide nanoparticle-based delivery systems for biotherapeutics.* Expert Opin Drug Deliv, 2013. **10**(1): p. 73-87.
169. Saleh, F., et al., *Real-Time Analysis of Endogenous Wnt Signalling in 3D Mesenchymal Stromal Cells.* Stem Cells Int, 2016. **2016**: p. 7132529.

170. Nagano, K., *R-spondin signaling as a pivotal regulator of tissue development and homeostasis.* Jpn Dent Sci Rev, 2019. **55**(1): p. 80-87.
171. Xu, Q., et al., *Vascular development in the retina and inner ear: control by Norrin and Frizzled-4, a high-affinity ligand-receptor pair.* Cell, 2004. **116**(6): p. 883-95.
172. Ke, J., et al., *Structure and function of Norrin in assembly and activation of a Frizzled 4-Lrp5/6 complex.* Genes Dev, 2013. **27**(21): p. 2305-19.
173. Iyer, S. and K.R. Acharya, *Tying the knot: the cystine signature and molecular-recognition processes of the vascular endothelial growth factor family of angiogenic cytokines.* FEBS J, 2011. **278**(22): p. 4304-22.
174. Chen, X., B. Bhandari, and P. Zhou, *Insight into the effect of glycerol on stability of globular proteins in high protein model system.* Food Chem, 2019. **278**: p. 780-785.
175. Bhat, J.K.K.a.R., *Thermal Stability of Proteins in Aqueous Polyol Solutions: Role of the Surface Tension of Water in the Stabilizing Effect of Polyols.* The Journal of Physical Chemistry B, 1998. **Vol 102**(Issue 36).
176. Du, H., R. Wickramasinghe, and X. Qian, *Effects of salt on the lower critical solution temperature of poly (N-isopropylacrylamide).* J Phys Chem B, 2010. **114**(49): p. 16594-604.
177. Hopkins, S.D. and E. Blaisten-Barojas, *Molecular dynamics simulations evidence the thermoresponsive behavior of PNIPAM and PDEA in glycerol solutions.* Frontiers in Nanotechnology, 2023. **5**: p. 1292259.
178. Kolli, A.R., *Deriving protein binding-corrected chemical concentrations for in vitro testing.* Clin Transl Sci, 2023. **16**(11): p. 2123-2129.
179. Alfano, C., et al., *Molecular Crowding: The History and Development of a Scientific Paradigm.* Chem Rev, 2024. **124**(6): p. 3186-3219.
180. Aguilar-Rabiela, A.E., et al., *Reduction of the in vitro toxicity of elevated concentrations of SPIONLA by its administration through PHBV/curcumin composite microspheres.* Frontiers in Biomaterials Science, 2022. **1**.
181. Soenen, S.J., et al., *Investigating the toxic effects of iron oxide nanoparticles.* Methods Enzymol, 2012. **509**: p. 195-224.
182. Wei, H., et al., *Superparamagnetic Iron Oxide Nanoparticles: Cytotoxicity, Metabolism, and Cellular Behavior in Biomedicine Applications.* Int J Nanomedicine, 2021. **16**: p. 6097-6113.
183. Dousti, M., et al., *Enhancing bone regeneration: Unleashing the potential of magnetic nanoparticles in a microtissue model.* J Cell Mol Med, 2024. **28**(17): p. e70040.
184. Liao, W., et al., *Osteogenesis of Iron Oxide Nanoparticles-Labeled Human Precartilaginous Stem Cells in Interpenetrating Network Printable Hydrogel.* Front Bioeng Biotechnol, 2022. **10**: p. 872149.
185. Zhao, Y.Z., et al., *Magnetic PLGA microspheres loaded with SPIONs promoted the reconstruction of bone defects through regulating the bone mesenchymal stem cells under an external magnetic field.* Mater Sci Eng C Mater Biol Appl, 2021. **122**: p. 111877.
186. Wu, S., et al., *Synergistic effect of a LPEMF and SPIONs on BMMSC proliferation, directional migration, and osteoblastogenesis.* Am J Transl Res, 2018. **10**(5): p. 1431-1443.
187. Osyczka, A.M., et al., *Age and skeletal sites affect BMP-2 responsiveness of human bone marrow stromal cells.* Connect Tissue Res, 2009. **50**(4): p. 270-7.

188. Ohta, H., et al., *The effects of heat on the biological activity of recombinant human bone morphogenetic protein-2.* J Bone Miner Metab, 2005. **23**(6): p. 420-5.
189. Tuysuz, N., et al., *Lipid-mediated Wnt protein stabilization enables serum-free culture of human organ stem cells.* Nat Commun, 2017. **8**: p. 14578.
190. Cheron, N., et al., *Protein Preferential Solvation in Water:Glycerol Mixtures.* J Phys Chem B, 2020. **124**(8): p. 1424-1437.
191. Narang, P., et al., *Unravelling the role of polyols with increasing carbon chain length and OH groups on the phase transition behavior of PNIPAM.* New Journal of Chemistry, 2018/08/06. **42**(16).
192. Kim, S.M., S.M. Lee, and Y.C. Bae, *Influence of hydroxyl group for thermoresponsive poly(N-isopropylacrylamide) gel particles in water/co-solvent (1,3-propanediol, glycerol) systems.* European polymer journal., 2014. **54**: p. 151-159.
193. *Preparation and characterization of thermoresponsive poly(N-isopropylacrylamide-co-N-isopropylmethacrylamide) hydrogel materials for smart windows.* Journal of Applied Polymer Science, 2021. **138**(6).
194. Jedlovszky-Hajdu, A., et al., *Surface coatings shape the protein corona of SPIONs with relevance to their application in vivo.* Langmuir, 2012. **28**(42): p. 14983-91.
195. Dombkowski, A.A., K.Z. Sultana, and D.B. Craig, *Protein disulfide engineering.* FEBS Lett, 2014. **588**(2): p. 206-12.